Contributions to the analysis of vibrations and acoustic emissions for the condition monitoring of epicyclic gearboxes

From the Faculty of Georesources and Materials Engineering of the

RWTH Aachen University

Submitted by

Cristián Molina Vicuña

from Concepción (Chile)

in respect of the academic degree of

Doctor of Engineering

approved thesis

Advisors:

Univ.-Prof. Dr.-Ing. Andreas Seeliger

apl. Prof. Dr.-Ing. Paul Burgwinkel

Date of the oral examination: 15.12.2009

ASRE - **A**ACHENER **S**CHRIFTEN ZUR **R**OHSTOFF- UND **E**NTSORGUNGSTECHNIK

DES INSTITUTS FÜR MASCHINENTECHNIK DER ROHSTOFFINDUSTRIE

Herausgeber:

Prof. Dr.-Ing. Andreas Seeliger

Prof. Dr.-Ing. Paul Burgwinkel

IMR - Institut für Maschinentechnik der Rohstoffindustrie der RWTH Aachen
Wüllnerstraße 2 • D-52056 Aachen
Tel.: +49 241 809 3845 • Fax: +49 241 809 2227
Internet: http://www.ibh.rwth-aachen.de • E-Mail: mail@ibh.rwth-aachen.de

1. Auflage Aachen:

Verlag R. Zillekens, 2010
Aachener Schriften zur Rohstoff- und Entsorgungstechnik, Band 72
ISBN: XXX-X-XXXXXX-XX-X

Verlag R. Zillekens
Am Bachpütz 4; 52224 Stolberg
Telefon 02408. 958216; Telefax 02408. 958217
E-Mail: verlag@druckservice-zillekens.de

Gesamterstellung

Druckservice Zillekens
Am Bachpütz 4; 52224 Stolberg
Telefon 02408. 958216; Telefax 02408. 958217
www.druckservice-zillekens.de; E-Mail: verlag@druckservice-zillekens.de

Bibliografische Information der deutschen Bibliothek

Die deutsche Bibliothek verzeichnet diese Publikation in der deutschen Nationalbibliografie. Detaillierte Bibliografische Daten sind im Internet unter http://dnb.ddb.de abrufbar.

D82 (Diss. RWTH Aachen)

Abstract

Condition monitoring of machines through vibration analysis has been successfully applied on different types of machines for several decades. However, there are still some mechanical systems where its use has not given the same good results. Epicyclic gearboxes (EG) belong to this group of systems. Due to its special characteristics, EG are used in a wide range of applications within the drive technology, mostly when high power transmission is required. Machines dealing with high power transmission are typically critical, which means that a large part of the process in which they are involved depends on their appropriate operation. Hence, there is a high interest on a solution that can effectively detect failures in EG at an early stage, before they evolve and produce major breakdowns.

Probably the most important reason for the deficient results of failure detection on EG through vibrations is the poor knowledge about the characteristics of the vibrations generated in EG. In an EG, each planet gear meshes with the sun gear and ring gear simultaneously. Hence, the number of meshing processes is equal to twice the number of planet gears, being one half of them internal and the other half external. Depending on the geometry of the gearbox, phase differences between all meshing processes can exist. These phase differences are also present in the vibrations generated in each of the meshing processes. This key point is one of the fundamentals for understanding the vibrations generated in EG. The second fundamental point relates to the influence of the measurement arrangement on the measured vibrations. For example, in the most typical case, vibrations are measured with a sensor mounted on the outer part of the ring gear of a planetary gearbox (one of the possible configurations of EG). During operation, the carrier plate rotates concentric with the sun gear. Since the planet gears are mounted on the carrier plate, they rotate around their own axis and revolve around the sun gear. Consequently, the points of contact between the meshing gears, that is the location of the sources of vibrations, also revolve around the sun gear. On the other hand, the sensor remains steady, so that the distance between the sensor and the points of generation of vibrations changes continuously. This phenomenon acts an amplitude modulation of the vibrations generated in the meshing of each planet with the sun and ring gear and repeats once per revolution of the carrier. The amplitude modulation functions acting on the vibrations generated on different planets are time-shifted according to the relative angular position between the planets. These two fundamental points determine the spectral structure of the vibrations measured on an EG. Thus, the vibrations measured on different types of non-faulty EG can present different shapes in their spectra.

The use of acoustic emissions (AE) as a tool for the condition monitoring is not new, however it is only in the last years it has expanded. Most auspicious results have been found in bearing diagnosis. Its use for gear diagnosis has focused only on conventional fixed-axis gearboxes. The AE signals generated during the meshing of two spur gears consist typically of a train of bursts over a continuous background noise. It has been postulated that the bursts are produced at the pure rolling portion of the meshing period, whereas the continuous AE is produced in the portion where a combination of rolling and sliding occur. In the case of EG, the relative phase between the different meshing processes and the influence of the measurement arrangement

must be considered, as was explained for the vibrations. Furthermore, there is a third point that must be considered: due to its high frequency nature the AE signals generated in the meshing of gears are essentially random. Still, they convey valuable information in form of "hidden periodicities".

Two theoretical models are developed, one for the vibrations and one for the AE generated on a planetary gearbox when measured with a sensor installed on the outer part of the ring gear. Care is taken in presenting the development and analysis of the models in a step-by-step manner, so that it can be used as a basis for the development of similar models for the other configurations of EG (i.e. solar and star) and/or other sensor positions.

The vibration model considers all vibrations as deterministic. Accordingly, the stationary approach (i.e. the analysis of the frequency spectrum) is sufficient. It is shown that, although different planetary gearboxes can produce different spectral structures of the vibrations, they can be classified in four groups depending on the phase differences existing between the meshing processes and the relative angular position between the gear planets.

Differently, the AE model considers the amplitude and the time of arrival of the AE bursts as random processes. The model is analysed separately for its deterministic and stochastic part. It is shown that the stationary approach applied to both parts is unable to reveal the information contained on the signal and, therefore, is less apt for failure diagnosis purposes. Conversely, the cyclostationary approach is able to reveal the hidden periodicities present on the signal. Therefore, it is best suited for diagnosis purposes. Since the cyclostationary theory still remains to some extent unknown, its most important concepts, results and signal processing tools are presented and illustrated through an example.

Finally, the stationary and cyclostationary approach are used for the analysis of vibrations and AE measured on a planetary gearbox test bench. Measurements under two types of seeded defects are investigated: localized planet bearing defect and single-tooth flank defect of one planet gear. Encouraging results were observed from the AE measurements. However, it is concluded that more work is needed to validate the proposed methodology. Results from industrial measurements are also presented. Here, no fault was observed; however, the measurements provided valuable information for the development of the models. Furthermore, a relation between the amplitude of the AE and the rotational speed of the gearbox, and the load acting on the gearbox was observed. This was further studied in the planetary gearbox test bench by taking measurements under different conditions of load and rotational speed.

Zusammenfassung

Schwingungsbasierte Zustandsüberwachung von Maschinen wird seit mehreren Jahrzehnten bei verschiedenen Maschinenarten erfolgreich angewendet. Es gibt jedoch mechanische Systeme, wo ihre Anwendung keine guten Ergebnisse geliefert hat. Umlaufgetriebe (UG) gehören zu dieser Gruppe von Systemen. Wegen ihrer speziellen Eigenschaften werden UG in verschiedenen Bereichen der Antriebstechnik genutzt, besonders wenn hohe Leistungsübertragungen erforderlich sind. Maschinen, die hohe Leistungen übertragen, sind typischerweise kritisch. Ihr störungsfreier Betrieb ist daher von immenser Wichtigkeit für reibungslose Prozessabläufe. Deswegen gibt es ein großes Interesse an einer Lösung für die Früherkennung von Fehlern in UG, bevor sie lange unvorhersehbare Stillstände nach sich ziehen.

Der wahrscheinlich wichtigste Grund für die schlechten Ergebnisse bei der Fehlerfrüherkennung in UG ist eine mangelnde Kenntnis der Merkmale der Schwingungen, die in UG erzeugt werden. Jedes Planetenrad eines UG greift gleichzeitig in das Sonnenrad und das Hohlrad ein. Dadurch ist die Anzahl von Zahneingriffsprozessen doppelt so groß wie die Anzahl von Planetenrädern im UG, wobei die eine Hälfte als Innen- und die andere Hälfte als Außenverzahnungen ausgeführt sind. Abhängig von der Geometrie des Getriebes können Phasenunterschiede zwischen den verschiedenen Zahneingriffsprozessen existieren. Diese Phasenunterschiede werden an die Schwingungen aller Zahneingriffe übertragen. Sie tragen fundamental zum Verständnis von Schwingungen in UG bei. Ein weiterer grundsätzlicher Punkt die Schwingungen in UG zu verstehen und zu analysieren bezieht sich auf den Einfluss, den die Messanordnung auf die gemessenen Schwingungen hat. Typischerweise werden Schwingungen an einem Planetengetriebe (eine Bauform eines UG) mit nur einem Sensor gemessen, der fest an der äußeren Oberfläche des Hohlrades montiert wird. Während des Betriebs dreht sich der Planetenträger konzentrisch zu dem Sonnenrad. Da die Planetenräder auf dem Planetenträger montiert werden, drehen sie sich um ihre eigene Achse und kreisen um das Sonnenrad. Folglich kreisen die Berührungspunkte zwischen allen eingreifenden Zahnrädern (d.h. die Position der Schwingungsquellen) auch um das Sonnenrad. Andererseits bleibt der Sensor ortsfest, sodass sich der Abstand zwischen dem Sensor und den Schwingungsquellen kontinuierlich ändert. Das verursacht eine variierende Übertragungsfunktion, die eine Amplitudenmodulation der Schwingungen, die durch den Zahneingriff jedes Planetenrades mit dem Sonnen- und Hohlrad erzeugt werden, zur Folge hat. Dieser Vorgang wiederholt sich einmal pro Umdrehung des Planetenträgers. Die Amplitudenmodulationsfunktionen, die in jedem Planetenrad wirken, sind in Abhängigkeit ihrer relativen Winkelanordnung zeitverschoben. Diese beiden Schlüsselpunkte bestimmen die Struktur des Spektrums der Schwingungen, gemessen auf einem UG.

Die Nutzung von acoustic emissions (AE) als ein Werkzeug für die Zustandsüberwachung von Maschinen ist nicht neu. Zu einem verbreiteten Einsatz kommt es aber erst seit einigen Jahren. Dabei haben sich die besten Ergebnisse im Bereich der Lagerdiagnose gezeigt. Die Anwendung in der Zahnraddiagnose hat sich nur auf herkömmliche Zahnradpaare mit festen Drehachsen konzentriert. Die AE, die im Zahneingriff von Stirnrädern erzeugt werden, bestehen typischerweise aus einer Folge von Stößen über einem kontinuierlichen Hintergrundrauschen. Es wird vermutet, dass die Stöße am rein rollenden Anteil der Zahneingriffsstrecke erzeugt werden. Das

kontinuierliche Rauschen ensteht in dem Anteil der Zahneingriffsstrecke, in dem eine Kombination aus Rollen und Schlupf vorliegt. Bei der Analyse von AE (in Anwendung auf UG) müssen die relative Phase zwischen den verschiedenen Zahneingriffen und der Einfluss der Messanordnung, wie im Falle der Schwingungen bereits beschrieben, betrachtet werden. Darüber hinaus gibt es einen weiteren wichtigen Punkt, der beachtet werden muss: wegen ihrer Hochfrequenzeigenschaft sind die im Zahneingriff erzeugten AE im Wesentlichen stochastische Signale. Dennoch befördern sie wertvolle Informationen in der Form von „verborgenen Periodizitäten".

Im Rahmen der vorliegenden Arbeit wurden theoretische Modelle entwickelt, mit deren Hilfe Schwingungen und AE in Abhängigkeit der Sensorposition auf dem Außenteil des Hohlrades eines Planetengetriebes, berechnet werden können. Die Entwicklung der Modelle und ihre Analyse werden sorgfältig und schrittweise präsentiert. Sie können somit als Basis für die Entwicklung, ähnlicher Modelle für andere Konfigurationen von UG (d.h. bei anderen feststehenden Bauelementen) und/oder verschiedenen Sensorpositionen dienen. Im Falle des Schwingungsmodells werden die Schwingungen als deterministisch betrachtet. Dementsprechend genügt die stationäre Betrachtung der Signale (d. h. die Analyse des Amplitudenspektrums). Es wird gezeigt, dass verschiedene Planetengetriebe verschiedene Strukturen des Schwingungsspektrums zeigen können. Diese können in vier Gruppen klassiert werden. Die Klassierung hängt von den Phasenunterschieden zwischen den Zahneingriffsprozessen und der relativen Winkellage zwischen den Planetenrädern ab.

Im Gegensatz dazu werden beim AE-Modell die Amplitude und die Ankunftszeit der AE-Stöße als Zufallsvariablen betrachtet. Das Modell wird für seinen deterministischen und stochastischen Anteil getrennt analysiert. Es wird gezeigt, dass die stationäre Betrachtung beider Anteile nicht geeignet ist, die Informationen, die im Signal enthalten sind, zu analysieren. Deshalb ist die stationäre Betrachtung von AE für Fehlerdiagnosezwecke weniger geeignet. Im Vergleich dazu ist die zyklostationäre Betrachtung in der Lage, die verborgenen Periodizitäten der AE zu offenbaren. Deshalb ist sie für Fehlerdiagnosezwecke besser geeignet. Da die zyklostationäre Theorie verhältnismäßig unbekannt ist, werden ihre wichtigsten Begriffe, Ergebnisse und Signalverarbeitungstools vorgestellt und durch ein Beispiel erklärt.

Schließlich wird die Anwendung der stationären und der zyklostationären Betrachtung für die Analyse von Schwingungen und AE, welche auf einem Planetengetriebeprüfstand gemessen wurden, beispielhaft vorgestellt. Messungen unter zwei Defektarten wurden untersucht: lokale Einzelschäden an einem Planetenlager und Schäden an der Flanke eines Zahnes eines Planetenrades. Die AE-Messungen führten zu ersten, guten Ergebnissen. Allerdings sollte das Projekt weiter geführt werden, da bisher nur wenig Vergleichsdaten zur Verfügung stehen und die bislang vorliegende Datenbasis lediglich aus Prüfstandsuntersuchungen stammen. Außerdem sollte die vorgeschlagene Methodik anhand weiterer Untersuchungen validiiert werden. Darüber hinaus präsentiert die vorliegende Arbeit Ergebnisse von industriellen Messungen auf Planetengetrieben. Die Analyse der Messergebnisse zeigten keinen Indizien von Schaden, sie lieferten jedoch zielführende Auskünfte für die Entwicklung der Schwingungs- und AE-Modelle. Es konnten Beziehungen zwischen der Amplitude der AE und der Drehzahl und zwischen der Ampitude der AE und der Last beobachtet werden. Diese Beziehungen konnten im Planetengetriebeprüfstand nur für die Drehzahl deutlich reproduziert werden.

Danksagung

Die vorliegende Arbeit entstand in der Zeit von Oktober 2006 bis September 2009 während meiner Tätigkeit als wissenschaftlicher Mitarbeiter am Institut für Bergwerks- und Hüttenmaschinenkunde (IBH) der Rheinisch-Westfälischen Technischen Hochschule Aachen. Dem Institutsleiter Herrn Univ. Prof. Dr.-Ing. Andreas Seeliger bin ich besonders dankbar für die Möglichkeit zu promovieren, das Vertrauen in meine Person, die Unterstützung und die Betreuung der vorliegenden Arbeit. Ein großer Dank gilt ebenso Prof. Dr.-Ing. Paul Burgwinkel für das Vertrauen, die Unterstützung und die konstruktiven Ratschläge.

An die Herren Dr.-Ing. Bernd Geropp, Dr.-Ing. Hans-Willi Keßler und Dipl.-Ing. Götz Langer der Fa. FAG Industrial Services geht mein herzlicher Dank für die Einführung in das Thema meiner Dissertation, die finanzielle Unterstützung des Projektes, das Interesse, die fachlichen Ratschläge, die Geduld bei meinen Sprachschwierigkeiten und vor allem das Vertrauen in meine Person.

Des Weiteren möchte ich mich bei den Herren Dr.-Ing. Jörn Lachmann, Dr.-Ing. Oliver Webber, Dr.-Ing. Jens Wellhausen und insbesondere beim Herrn Dipl.-Ing. Klaus Vaehsen für die schöne Zusammenarbeit und kontinuierliche Hilfe im Laufe des Projektes bedanken. Auch an sie und die Herren Dipl.-Ing. Frank Höhne und Dipl.-Ing. Ralph Baltes gilt mein Dank für die Hilfe bei der Vorbereitung des Messsystems und bei der Durchführung der Betriebsmessungen. Die Herren Dr.-Ing. Bruno van den Heuvel und Dr.-Ing. Eicko Hinrichs ermöglichten die Messungen an den Schaufelradbaggern bzw. Windenergieanlagen. Dafür bedanke ich mich herzlich bei Ihnen. Mein Dank gilt auch den Herren Matthias Gitzen, Christoph Höweler und Marius Hirsch für die Zusammenarbeit bei der Vorbereitung des Prüfstandes.

Allen Mitarbeitern des IBH danke ich für die Zusammenarbeit und das tolle Arbeitsklima. Auch möchte ich mich beim Dr.-Ing. Christian Schaaf, ehemals Oberingenieur des IBH, für den herzlichen Empfang am Institut bedanken. Herrn Dr.-Ing. David Buttgereit bin ich für den LaTeX-Frame als Vorlage für diese Dissertation sehr dankbar. Mein Dank gilt auch an Herrn Axel Poqué für die 3D-Zeichnung des Planetengetriebes. Herrn Michael Heyers und seinem Team sei für die Besorgung eines neuen Rechners für meine Arbeit und die Verwaltung der Software gedankt. Ich danke auch Herr Hans Püttmann für den hilfreiche Deutschunterricht. An dieser Stelle möchte ich auch Frau Dipl.-Ing. Esther Neye und Herrn Dipl.-Ing. Daniel Vreydal für die zahlreichen Sprachkorrekturen in Berichten, Protokolle, usw. herzlich danken. Mein großer Dank gilt auch der ausländischen Truppe des IBH: Dipl.-Ing. Sandor Berde, Gamil Eltaliawi, M.Sc., Dipl.-Ing. Raul Vintila, Herr Andreas Jarzombek (Ehrenmitglied) und insbesondere an Herrn Nandhakumar Vijayakumar, M.Sc. deren Hilfsbereitschaft und Freundschaft kein Ende haben. Meinen chilenischen Freunden (mit deutschen Namen) Tatjana von Frey und Sebastian Fingerhuth bin ich, insbesondere für die große Hilfe bei der Wohnungssuche am Anfang –wenn alles etwas schwierig war– und ihre wertvolle Freundschaft immens dankbar.

I am indebted to Prof. Jerome Antoni, who not only answered my E-Mails with questions about cyclostationarity, but also received me in Compiegne and used his time to discuss and

answer all my questions regarding the bearing model. Herrn Dr.-Ing. Matthias Wien bin ich sehr dankbar für die Diskussion und die Vorschläge bezüglich der Frequenzanalyse meines Schwingungsmodells.

I would like to thank Mr. Sebastian Fingerhuth and Mr. Nandhakumar Vijayakumar, M.Sc. for the English revision. However, I take all responsibility for all still remaining errors.

Schließlich gilt mein aller größter Dank meiner Frau Tania, die immer bei mir während dieses Abenteuers war. Bei ihr bedanke ich mich für ihre Motivation, Unterstützung, Geduld und unendlichen Liebe. In bescheidener Weise widme ich ihr meine Dissertation.

The project was supported by the Programme Alßan, the European Union Programme of High Level Scholarships for Latin America, scholarship No. E06D100713CL.

List of symbols

$a_i^r(t)$	Amplitude modulation function of the vibrations $v_i^r(t)$
$a_i^s(t)$	Amplitude modulation function of the vibrations $v_i^s(t)$
a_q^r	Fourier coefficients of $a_1^r(t)$
a_k^s	Fourier coefficients of $a_1^s(t)$
$\{A_k^i\}_{k\in\mathbb{Z}}$	Periodically delta-correlated random point process
f	Frequency [Hz]
f_{Bn}	Magnitude of the relative rotational frequency between the inner and outer ring of the bearing n
f_C	Rotational frequency of the carrier plate [Hz]
f_g^p	Magnitude of the gear mesh frequency for a planetary gearbox
f_g^{so}	Magnitude of the gear mesh frequency for a solar gearbox
f_g^{st}	Magnitude of the gear mesh frequency for a star gearbox
f_P	Rotational frequency of the planet gear [Hz]
f_R	Rotational frequency of the ring gear [Hz]
f_S	Rotational frequency of the sun gear [Hz]
i	Index for the planet gear ($i = 1, 2, \ldots N$)
j	$\sqrt{-1}$
K	Number of stages of a multi-stage epicyclic gearbox
$K_{xx}(t, \tau)$	Autocovariance function of $x(t)$
$m_{y_i}^r(t)$	Deterministic part of $y_i^r(t)$
$M_{y_i}^r(f)$	Fourier transform of $m_{y_i}^r(t)$
$\{n(t)\}_{t\in\mathbb{R}}$	Zero-mean stationary additive background noise
N	Number of planet gears
$P_x(t)$	Power spectral density of $x(t)$
$P_x(t, f; \Delta f)$	Instantaneous power spectrum of $x(t)$
$P_x^\alpha(t; \Delta f)$	Cyclic modulation spectrum of $x(t)$
r_P	Radius of the pitch circle of the planet gear
r_R	Radius of the pitch circle of the ring gear
r_S	Radius of the pitch circle of the sun gear

$R_{xx}(t, \tau)$	Autocorrelation function of $x(t)$
$s(t)$	AE time waveform
$S(f)$	Fourier transform of $s(t)$
$S_{xx}^{\alpha}(f)$	Spectral correlation density of $x(t)$
$\gamma_{xx}^{\alpha}(f)$	Spectral coherence of $x(t)$
t_1	Time shift due to the unknown position of the planet gears at the beginning of a measurement [s]
T_C	Rotational period of the carrier plate ($T_C = 1/f_C$)
TP_R^r	Direct transmission path of the vibrations generated in the planet-ring gear meshes through the ring gear
TP_R^s	Direct transmission path of the vibrations generated in the sun-planet gear meshes through the ring gear
TP_{SC}^r	Transmission path of the vibrations generated in the planet-ring gear meshes through the sun gear and carrier plate
TP_{SC}^s	Transmission path of the vibrations generated in the sun-planet gear meshes through the sun gear and carrier plate
$v_i^r(t)$	Vibration generated in the meshing between the i-th planet gear and the ring gear, as experienced by an observer standing in the carrier plate
$v_i^s(t)$	Vibration generated in the meshing between the i-th planet gear and the sun gear, as experienced by an observer standing in the carrier plate
v_k^r	Fourier coefficients of $v_1^r(t)$
v_k^s	Fourier coefficients of $v_1^s(t)$
$v^r(t)\|_{TP_R^r}$	Vibrations generated in the planet-ring gear meshes that are transmitted to the sensor directly to the ring gear
$v^s(t)\|_{TP_R^s}$	Vibrations generated in the sun-planet gear meshes that are transmitted to the sensor directly to the ring gear
$v^r(t)\|_{TP_{SC}^r}$	Vibrations generated in the planet-ring gear meshes that are transmitted through the sun gear and carrier plate
$v^s(t)\|_{TP_{SC}^s}$	Vibrations generated in the sun-planet gear meshes that are transmitted through the sun gear and carrier plate

$x_i^r(t)$	Amplitude-modulated vibration generated in the meshing between the i-th planet gear and the ring gear, as experienced by the sensor
$x_i^s(t)$	Amplitude-modulated vibration generated in the meshing between the i-th planet gear and the sun gear, as experienced by the sensor
$X_i^r(f)$	Fourier transform of $x_i^r(t)$
$X_i^s(f)$	Fourier transform of $x_i^s(t)$
$x^r(t)$	Total vibrations experienced by the sensor, considering only the meshing with the ring gear and the transmission through the ring gear
$x^s(t)$	Total vibrations experienced by the sensor, considering only the meshing with the sun gear and the transmission through the ring gear
$x^{r,s}(t)$	Total vibrations experienced by the sensor, considering the meshing with the ring gear and sun gear and the transmission through the ring gear
$X^r(f)$	Fourier transform of $x^r(t)$
$X^s(f)$	Fourier transform of $x^s(t)$
$X^{r,s}(f)$	Fourier transform of $x^{r,s}(t)$
$y_i^r(t)$	AE generated in the meshing of the i-th planet gear with the ring gear and transmitted transmitted trhough the ring gear, as experienced from the sensor
$y^r(t)$	Total AE experienced by the sensor, considering only the meshing with the sun gear and the transmission through the ring gear
Z_P	Number of teeth of the planet gear
Z_R	Number of teeth of the ring gear
Z_S	Number of teeth of the sun gear
α	Cyclic frequency [Hz]
γ_{ri}	Phase difference between $v_i^r(t)$ and $v_1^r(t)$
γ_{si}	Phase difference between $v_i^s(t)$ and $v_1^s(t)$
γ_{sr}	Phase difference between $v_i^r(t)$ and $v_i^s(t)$
ψ_i	Relative angle between the position of the i-th planet gear and the first planet gear ($\varphi_1 = 0°$)
$\{\tau_k^i\}_{k\in\mathbb{Z}}$	Zero-mean delta correlated random point process with PDF $\varphi_\tau(\tau_k^i)$

$\Phi_\tau^i(f)$	Characteristic function of the process $\{\tau_k^i\}_{k\in\mathbb{Z}}$
$\angle_R$	Angular pitch of the ring gear
$\angle_S$	Angular pitch of the sun gear

Acronyms

AE	Acoustic emissions
ACR	Autocorrelation function
ACVF	Autocovariance function
CS	Cyclostationarity
CS1	First-order cyclostationarity
CS2	Second-order cyclostationarity
CSn	n-th-order cyclostationarity
DC	Direct current
dTE	Dynamic transmission error
EG	Epicyclic gearbox
FT	Fourier transform
FFT	Fast Fourier transform
ICP	Integrated circuit piezoelectric
IEPE	Integral electronics piezoelectric
LsTE	Loaded static transmission error
PC	Personal computer
PDF	Probability density function
PG	Planetary gearbox
PSD	Power spectral density
SCD	Spectral correlation density
SCoh	Spectral coherence
SP	Signal processing
SW	Software
TE	Transmission error
UsTE	Unloaded static transmission error

General Introduction

Problem description and motivation

Condition monitoring of machines (CM) –refered also as machine diagnosis– deals with the assessment of machine functioning condition, the detection and the identification of failures by means of external indications. There are different indications depending on the types of failures being present. For example, it has been found that the vibrations emmited by the machine contain rich information regarding its condition. The reason for this is that vibrations result from the forces acting on the components of the machine. The presence of failures produces a change in the normal behavior of these forces, which is observed on the resulting vibrations.

Condition monitoring through vibration analysis is well known and has been documented for different types of machines or machine parts such as bearings and fixed-shaft gearboxes. Research in this field has been consistently carried out, which has lead to the development of several techniques, nowadays established for the detection and identification of different types of failures. All this has lead to successful application of condition monitoring on a wide range of machines.

However, there are some systems where the application of CM has not given the same good results. The reasons for this are many: low rotational speed, high speed and/or load variability, adverse conditions for the transmission of vibrations from the source to the sensor, high complexity of the physical phenomena involved, etc. Epicyclic gearboxes belong to this group of systems. They are used normally for high torque applications. Hence, the speed is usually very low. Moreover, its construction characteristics result in an adverse enviroment for the vibration tranmission. In addition, the kinematics of its components play an important role in the resulting vibrations.

Research has been carried out in the area of vibration analysis of planetary gearboxes –the most common configuration of epicyclic gearboxes. Different techniques have been proposed for the diagnosis of faults of gears and carrier plate. Some of them, however, lack in generality or are difficult to put into practice. Some attempts for bearing failure diagnosis have been undertaken without much favorable results. Hence, there is a large room for improvement related to the

problem of condition monitoring of epicyclic gearboxes through vibration analysis.

Since epicyclic gearboxes are used in many industrial applications –usually in large scale– a reliable solution for its condition monitoring is highly desirable. All this motivated the excecution of a cooperation project between the Institute of Mining and Metallurgical Machine Design (Institut für Bergwerks- und Hüttenmaschinenkunde, IBH) of the RWTH Aachen University and the company FAG Industrial Services, with the aim of developing a solution to the condition monitoring of epicyclic gearboxes. This thesis presents the main results and findings of this project.

Objective

This thesis is developed in view of giving a solution to the condition monitoring of epicyclic gearboxes. In this regard, the original main objective of this thesis was defined as the **analysis of the vibrations generated in an epicyclic gearbox in general, with emphasis on planetary gearboxes**. During the development of the work, the use of acoustic emissions (AE) was seen as a potential aid for the solution to the problem. Consequently, the **analysis of the acoustic emissions generated in an epicyclic gearbox** was also included in the main objective of the thesis.

The secondary objectives are the following:

- the kinematic analysis of an epicyclic gearbox in general,
- the analysis of the physical phenomena behind the generation of vibrations and AE in a non-faulty and faulty epicyclic gearbox,
- the proposal of a model for the vibrations and AE generated on a non-faulty and faulty epicyclic gearbox,
- the study of the potential suitable signal processing tools to be used on the signals measured on an epicyclic gearbox,
- the application of the selected tools on real signals measured on a planetary gearbox and the analysis of the results.

Outline of the work

The thesis is structured as follows:

Chapter 1 presents a description of an epicyclic gearbox, its working principle and its possible configurations: planetary, solar and star. Its main characteristics and applications are presented. Following, the kinematic analysis is developed first for a single-stage epicyclic gearbox and then is expanded for a multi-stage epicyclic gearbox. A review of the literature found regarding condition monitoring of epicyclic gearboxes is presented. Finally, the fundamentals of vibration and acoustic emissions phenomena in epicyclic gearboxes are reviewed.

Chapter 2 presents the development of a novel model for the vibrations generated in a planetary gearbox when measured with a sensor located on the outer part of the ring gear. This model considers the difference in phase between all meshing processes present in the planetary gearbox. It is first developed by considering only the vibrations generated in the meshing between the planet gear wheels and the ring gear, and the transmission path through the ring gear. Based on the Fourier analysis of the model, it is shown that the vibrations generated in a planetary gearbox can be different depending on its geometrical characteristics. However, they can be classified in four groups. Each group is carefully analysed and examples are provided to facilitate the understanding. Afterwards, the influence of the vibrations generated in the meshing between the planet gear wheels and the sun gear, and of the transmission of the vibrations through the sun gear and carrier plate are studied. Part II also presents a proposition of a model developed in time domain for the AE generated in a planetary gearbox. The model accounts for randomness found in the time of arrival of the AE bursts. Accordingly, the Fourier analysis of the model is developed separately for the deterministic and stochastic part. It is shown that –opposed to the conventional stationary approach–, the cyclostationary approach is able to reveal the information contained in the AE signal, thus making it a good candidate for the use in diagnosis of epicyclic gearboxes. The cyclostationary approach is reviewed and its main signal processing tools are presented. An example illustrates its benefits.

Chapter 3 presents the results of measurements of vibrations and AE carried out in a planetary gearbox test bench. The measurements were carried out under different conditions of speed and load, and under three different fault conditions: non faulty, localized bearing fault and localized gear fault. The stationary and cyclostationary approach is used for the treatment of the signals and are illustrated through selected results. Finally, selected results from the

industrial measurements carried out in bucket wheel excavators and wind turbines are also presented.

Chapter 4 gives a general conclusion of the work.

The author hopes the presented work to be of some contribution for people dealing with the fascinating problem of condition monitoring of epicyclic gearboxes, as well as for the future development of the vibrations- and/or AE-based condition monitoring systems for epicyclic gearboxes.

Contents

1. Failure diagnosis in epicyclic gearboxes

1.1. Epicyclic gearboxes

1.1.1. Description and working principle

An epicyclic gearbox (EG) is an arrangement of gears consisting of one central gear that meshes with one or more intermediate gears placed at different positions around the central gear. The intermediate gears are held in their position by a structure called carrier plate. In addition, they mesh with an outer gear. Figure 1.1 shows a crosssection of a single-stage epicyclic gearbox.

Typically, an EG is used as a transmission with one of its components (i.e. the central gear, the carrier plate or the annulus gear) kept fixed. Consequently, there are three possible configurations , each providing different speed ratios (see Table 1.1). In the planetary configuration the terms sun, planet and ring are used to designate the center, intermediate and annulus gear respectively. Since the planetary type is the most expanded form of epicyclic gearboxes, these designations are used for all types of epicyclic gearboxes. However, the terms epicyclic and planetary should not be confused, as it is commonly done.

As an example, let us take a planetary gearbox with the sun used as an input to illustrate the working principle of an epicyclic gearbox. As the sun gear rotates, the planets are forced to rotate around their own axis of rotation. However, since they additionally mesh with the stationary ring gear, they are also forced to revolve around the axis of rotation of the sun gear. The revolving motion of the planets is finally transferred to the carrier plate, which constitutes the output of the gearbox.

Now, let us consider a solar gearbox and follow the path traced by a fixed point on the pitch circle of one planet gear during the operation of the gearbox. Since the planet rotates around

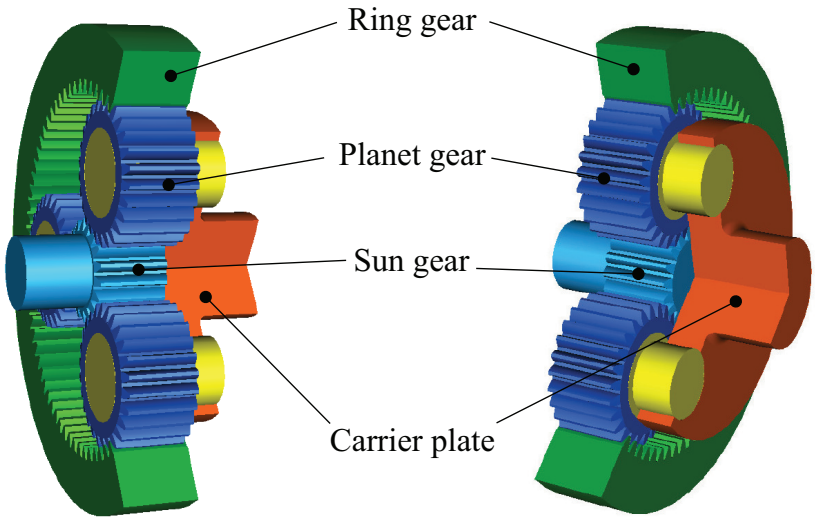

Figure 1.1: Illustration of a single-stage epicyclic gearbox.

Table 1.1: Different types of epicyclic gearboxes.

Denomination	Fixed component	Input/Output in reduction mode
Planetary	Outer gear	Central gear/Carrier plate
Solar	Central gear	Outer gear/Carrier plate
Star	Carrier plate	Central gear/Outer gear

its own axis and also revolves around the sun axis, the point follows a combination of a rotary and translatory motion, as illustrated in figure 1.2b. The path traced by the point is called epicycloid and explains the name given to this group of gearboxes. Note, however, that an epicycloidal path will be followed by this point only when the instantaneous center of rotation of the planet gear is located on the point of contact between the pitch circles of the sun and planet gear, as is the case for a solar gearbox. In a planetary gearbox, the instantaneous center of rotation of the planet is located on the point of contact between the pitch circles of the planet gear and the ring gear (see figure 1.2a). In this case, the path followed by the point is not an epicycloid, but an hypocycloid. Differently, in the case of a star gearbox the carrier plate is fixed, so that the axis of rotation of all gears is also fixed and the path followed by the point is a circle, as shown in fig. 1.2c. Notwithstanding the different traces followed by the fixed point on each configuration, due to the similarity between them, they are grouped under the epicyclic designation.

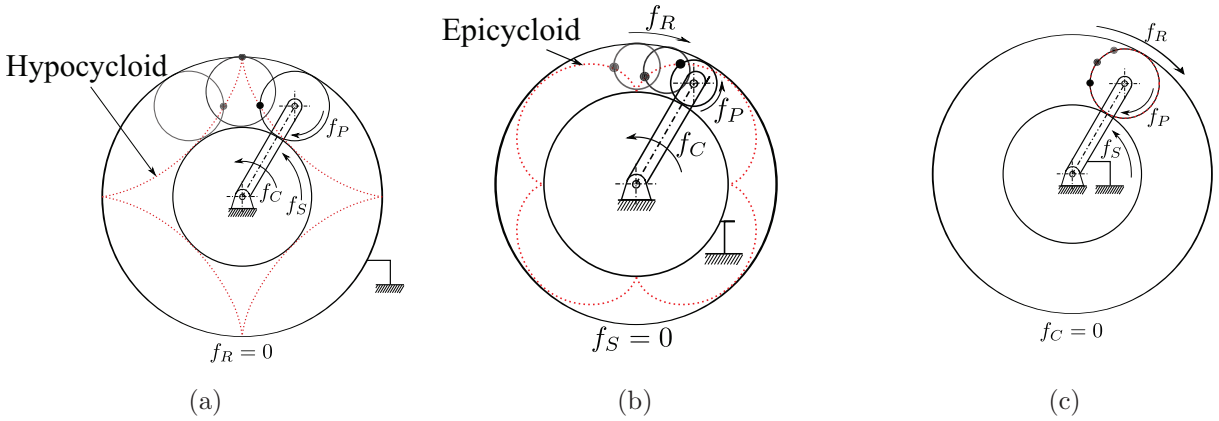

Figure 1.2: Path traced by a fixed point on the planet for different EG configurations. (a) Planetary (b) Solar (c) Star.

1.1.2. Characteristics, advantages, disadvantages and applications

The main feature of an EG is that the load is shared between several meshes. This permits the design to be compact and therefore light units compared to conventional fixed-shaft gearboxes can be constructed. Some planetary units can be up to one tenth of the size and weight of a conventional gearbox, while providing the same ratio [Smi03]. High speed ratio is other characteristic of epicyclic gearboxes, where values of 10 are normal for a single-stage planetary gearbox. The combination of both features makes EG specially apt for high power transmission and is in this field where they find most applications.

EG have a concentric input and output, which can be viewed as an advantage or as a disadvantage depending on the application requirements. The main disadvantages of EG are mainly due to its high compactness and construction complexity, which restricts the access to its components, principally to the planet gears and its bearings. For the same reason, cooling can be problematic.

EG are used in a wide range of applications within the drive technology. For example they are found in the main transmission of helicopters [HZ06], in turbo propellers for speed reduction between the power turbine and the propeller shaft [ZLSV07], in the drive chain of longwall conveyors [SMW85][SM87], in automatic transmission of vehicles [Loo96], in the loading system of bucket wheel excavators [BZ09], in the propeller system of heavy vehicles [Dou50], in wind turbines [VBVW09], etc.

1.2. Kinematic analysis of epicyclic gearboxes

In this section, the expressions for the rotational speeds of all components of a single-stage EG are derived. Subsequently, the particular expressions for the three configuration types of EG are obtained. Finally, the expressions are extended for a multi-stage EG.

1.2.1. Single stage epicyclic gearbox

1.2.1.1. Rotational frequency of gear wheels

Figure 1.3 represents a single-stage epicyclic gearbox with all elements allowed to rotate and its associated diagram of velocities, from which

$$\frac{v_B}{2r_P - x} = \frac{v_C}{r_P - x} = \frac{-v_D}{x} \tag{1.1}$$

where the negative sign indicates an opposite sense of rotation. From the first equality of eq. (1.1) we obtain $x = (v_B - 2v_C)\, r_P / (v_B - v_C)$. Substituting this result into the second equality of eq. (1.1) we have

$$v_D = 2v_C - v_B \tag{1.2}$$

From fig. 1.3b we also have $v_B = 2\pi f_S r_S$, $v_C = 2\pi f_C (r_S + r_P)$ and $v_D = 2\pi f_R r_R$, where f_C, f_R and f_S are the rotational frequencies of the carrier plate, ring gear and sun gear respectively. Substituting these expressions into eq. (1.2) we obtain:

$$f_R r_R = 2f_C (r_S + r_P) - f_S r_S \tag{1.3}$$

Also from fig. 1.3b, $v_D = v_C + 2\pi f_P r_P$, from which:

$$f_P r_P = f_C (r_S + r_P) - f_S r_S \tag{1.4}$$

Equations (1.3) and (1.4) relate the rotational speed of all elements of the single-stage EG of fig. 1.3a. Note that at least two rotational speeds are needed to determine the rest. Thus, for

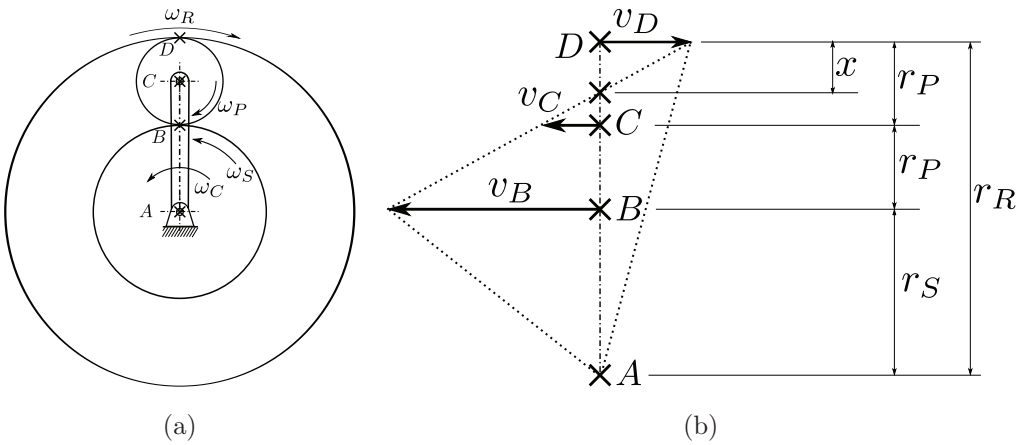

Figure 1.3: (a) Single-stage epicyclic gearbox (b) Associated diagram of velocities.

Table 1.2: Rotational speeds for a single-stage epicyclic gearbox.

Denomination	Condition	f_{input}	f_{output}	$f_{\text{intermediate}}$
Planetary	$f_R = 0$	f_S	$f_C = \frac{Z_S}{Z_S+Z_R} f_S$	$f_P = \frac{-Z_S(Z_R-Z_P)}{Z_P(Z_S+Z_R)} f_S$
Solar	$f_S = 0$	f_R	$f_C = \frac{Z_R}{Z_S+Z_R} f_R$	$f_P = \frac{Z_R(Z_S+Z_P)}{Z_P(Z_S+Z_R)} f_R$
Star	$f_C = 0$	f_S	$f_R = \frac{-Z_S}{Z_R} f_S$	$f_P = \frac{-Z_S}{Z_P} f_S$

the configuration types of table 1.1, since one element does not rotate (i.e. $f_R,\ f_S,$ or $f_C = 0$), it is possible to calculate the rotational speeds as a function of the input speed. The results of this procedure are given in table 1.2, where use of the following relations has been made: $2\,(r_S + r_P) = r_R + r_S$ and $2r_i = mZ_i$, where r_i is the pitch radius, m is the module of the gear wheels and Z_i is the number of teeth of the gear $i = S, P, R$[1].

1.2.1.2. Rotational frequencies of bearings

The relative rotational frequency between the linked components of the EG is equal to the relative rotational frequency between the inner and outer ring of the bearings. Its magnitude determine the fault frequencies of the bearings [How94] and therefore its calculation is of major importance for the analysis of vibrations and AE. Figure 1.4 shows schematically a bearing arrangement for a single-stage EG. Based on this figure and taking the results from section 1.2.1.1 into account, the magnitude of the relative rotational frequency between the inner and

[1] S: sun gear, P: planet gear and R ring gear

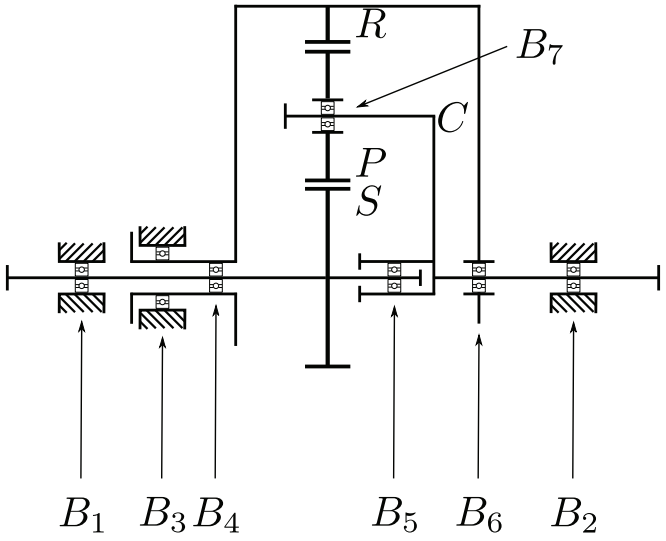

Figure 1.4: Typical arrangement of bearings in an EG [Loo96].

outer ring of the bearings can be expressed as follows:

$$f_{B_1} = |f_S| \tag{1.5a}$$

$$f_{B_2} = |f_C| \tag{1.5b}$$

$$f_{B_3} = |f_R| \tag{1.5c}$$

$$f_{B_4} = |f_S - f_R| \tag{1.5d}$$

$$f_{B_5} = |f_S - f_C| \tag{1.5e}$$

$$f_{B_6} = |f_C - f_R| \tag{1.5f}$$

$$f_{B_7} = |f_P - f_C| \tag{1.5g}$$

Equations (1.5) are the general expressions for calculating the rotational frequency of the bearings for a single-stage EG for an arrangement according to fig. 1.4. From them, the expressions for each configuration type of EG can be calculated as a function of any rotational frequency by using the results of section 1.2.1.1. Table 1.3 shows the results of this procedure.

1.2.1.3. Gear mesh frequency

It is well known that the determination of the gear mesh frequency is also of great importance for the condition monitoring of gearboxes [BCR97] [Smi03]. In an EG, the number of meshing

Table 1.3: Magnitude of the bearing rotational frequencies for a single-stage epicyclic gearbox.

Denomination	f_{B_1}	f_{B_2}	f_{B_3}	f_{B_4}	f_{B_5}	f_{B_6}	f_{B_7}
Planetary	$\lvert f_S \rvert$	$\frac{f_S}{Z_S+Z_R}\lvert f_S \rvert$	0	$\lvert f_S \rvert$	$\frac{Z_R}{Z_S+Z_R 3}\lvert f_S \rvert$	$\frac{Z_S}{Z_S+Z_R}\lvert f_S \rvert$	$\frac{Z_S Z_R}{Z_P(Z_S+Z_R)}\lvert f_S \rvert$
Solar	0	$\frac{Z_R}{Z_S+Z_R}\lvert f_R \rvert$	$\lvert f_R \rvert$	$\lvert f_R \rvert$	$\frac{Z_R}{Z_S+Z_R}\lvert f_R \rvert$	$\frac{Z_S}{Z_S+Z_R}\lvert f_R \rvert$	$\frac{Z_S Z_R}{Z_P(Z_S+Z_R)}\lvert f_R \rvert$
Star	$\lvert f_S \rvert$	0	$\frac{Z_S}{Z_R}\lvert f_S \rvert$	$\frac{Z_S+Z_R}{Z_R}\lvert f_S \rvert$	$\lvert f_S \rvert$	$\frac{Z_S}{Z_R}\lvert f_S \rvert$	$\frac{Z_S}{Z_P}\lvert f_S \rvert$

processes is equal to twice the number of planet gears. However, all mesh processes have the same frequency, whose magnitude is given by

$$f_g = \lvert f_R - f_C \rvert Z_R \tag{1.6}$$

where f_g is the general expression for the gear mesh frequency, f_R is the rotational frequency of the ring gear and f_C is the rotational frequency of the carrier plate. By substituting the results obtained from section 1.2.1.1 into eq. (1.6) the following expressions are obtained, which permit the calculation of the gear mesh frequency for the three configuration types of a single-stage EG, provided one rotational frequency and the number of teeth of the gears are known:

$$f_g^p = \frac{Z_S Z_R}{Z_S + Z_R}\lvert f_S \rvert = Z_R \lvert f_C \rvert \quad = \frac{Z_P Z_R}{Z_R - Z_P}\lvert f_P \rvert \tag{1.7a}$$

$$f_g^{so} = Z_S \lvert f_C \rvert \quad = \frac{Z_S Z_P}{Z_S + Z_P}\lvert f_P \rvert = \frac{Z_S Z_R}{Z_S Z_R}\lvert f_R \rvert \tag{1.7b}$$

$$f_g^{st} = Z_S \lvert f_S \rvert \quad = Z_P \lvert f_P \rvert \quad = Z_R \lvert f_R \rvert \tag{1.7c}$$

where the superscripts p, so and st refer to the planetary, solar and star configuration respectively.

1.2.2. Multi-stage epicyclic gearbox

In a multi-stage EG, two or more single-stage EG are connected in series. This implies that the output of a given stage is coupled to the input of the following. Although there is no restriction, usually all stages of the EG are of the same configuration type. This is, for example, the case of the drive train of the bucket wheel excavator presented in fig. 1.5, where a two-stage planetary

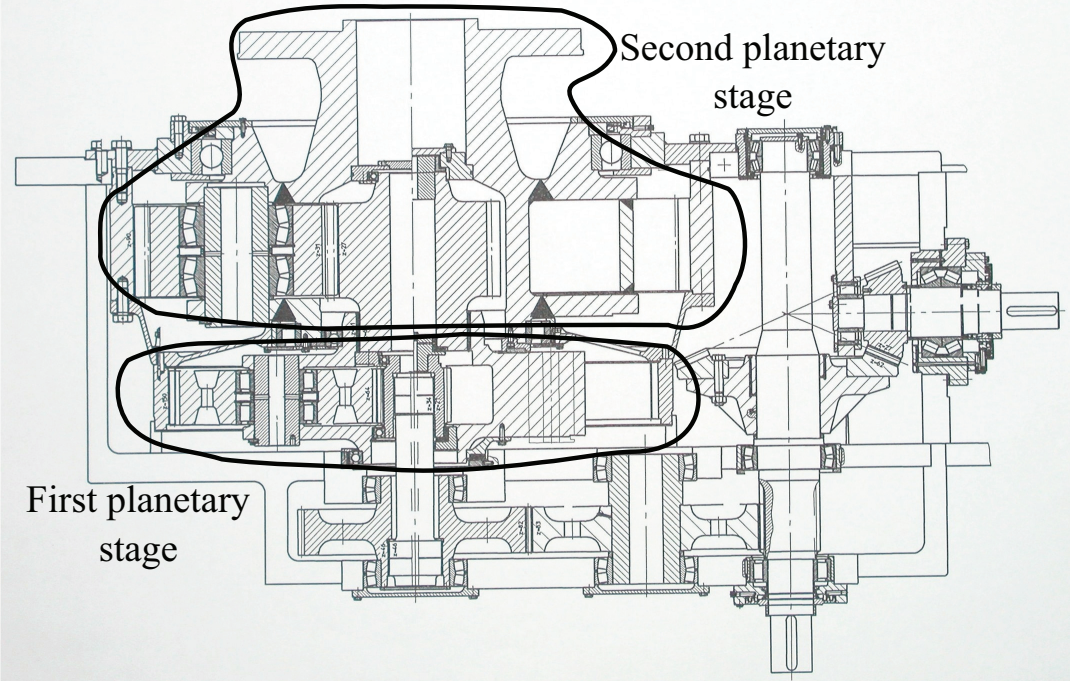

Figure 1.5: Drive gearbox of a bucket wheel excavator including two planetary stages in series.

gearbox is used to drive the bucket wheel. Based on the results of section 1.2.1.1, the generalised expressions are presented in table 1.4 for a multi-stage EG with all stages having the same configuration. Other arrangements of multi-stage EG can be derived from these expressions by combining the appropriate inputs and outputs.

Table 1.4: General expressions for a K-stage epicyclic gearbox.

	Solar	Planetary	Star
Input	Ring gear	Sun gear	Sun gear
Output	Carrier plate	Carrier plate	Ring gear
$f_{input,K}$	$f^{so}_{R,K} = \left[\prod_{k=1}^{K-1} \frac{Z_{R,k}}{Z_{S,k}+Z_{R,k}}\right] f^{so}_{R,1}$	$f^{p}_{S,K} = \left[\prod_{k=1}^{K-1} \frac{Z_{S,k}}{Z_{S,k}+Z_{R,k}}\right] f^{p}_{S,1}$	$f^{st}_{S,K} = \left[\prod_{k=1}^{K-1} \frac{Z_{S,k}}{Z_{R,k}}\right] f^{st}_{S,1}$
$f_{ouput,K}$	$f^{so}_{C,K} = \left[\prod_{k=1}^{K} \frac{Z_{R,k}}{Z_{S,k}+Z_{R,k}}\right] f^{so}_{R,1}$	$f^{p}_{C,K} = \left[\prod_{k=1}^{K} \frac{Z_{S,k}}{Z_{S,k}+Z_{R,k}}\right] f^{p}_{S,1}$	$f^{st}_{R,K} = \left[\prod_{k=1}^{K} \frac{Z_{S,k}}{Z_{R,k}}\right] f^{st}_{S,1}$
$f_{P,K}$	$f^{so}_{P,K} = \left[\prod_{k=1}^{K} \frac{Z_{R,k}}{Z_{S,k}+Z_{R,k}}\right] \frac{Z_{S,K}+Z_{P,K}}{Z_{P,K}} f^{so}_{R,1}$	$f^{p}_{P,K} = \left[\prod_{k=1}^{K} \frac{Z_{S,k}}{Z_{S,k}+Z_{R,k}}\right] \frac{Z_{R,K}-Z_{P,K}}{Z_{P,K}} f^{p}_{S,1}$	$f^{st}_{P,K} = \left[\prod_{k=1}^{K-1} \frac{Z_{S,k}}{Z_{R,k}}\right] \frac{Z_{S,K}}{Z_{P,K}} f^{st}_{S,1}$
$f_{g,K}$	$f^{so}_{g,K} = \left[\prod_{k=1}^{K} \frac{Z_{R,k}}{Z_{S,k}+Z_{R,k}}\right] Z_{S,K} \left\lvert f^{so}_{R,1}\right\rvert$	$f^{p}_{g,K} = \left[\prod_{k=1}^{K} \frac{Z_{S,k}}{Z_{S,k}+Z_{R,k}}\right] Z_{R,K} \left\lvert f^{p}_{S,1}\right\rvert$	$f^{st}_{g,K} = \left[\prod_{k=1}^{K-1} \frac{Z_{S,k}}{Z_{R,k}}\right] Z_{S,K} \left\lvert f^{st}_{S,1}\right\rvert$
$f_{B_1,K}$	$f^{so}_{B_1,K} = 0$	$f^{p}_{B_1,K} = \left[\prod_{k=1}^{K-1} \frac{Z_{S,k}}{Z_{S,k}+Z_{R,k}}\right] \left\lvert f^{p}_{S,1}\right\rvert$	$f^{st}_{B_1,K} = \left[\prod_{k=1}^{K-1} \frac{Z_{S,k}}{Z_{R,k}}\right] \left\lvert f^{st}_{S,1}\right\rvert$
$f_{B_2,K}$	$f^{so}_{B_2,K} = \left[\prod_{k=1}^{K} \frac{Z_{R,k}}{Z_{S,k}+Z_{R,k}}\right] \left\lvert f^{so}_{R,1}\right\rvert$	$f^{p}_{B_2,K} = \left[\prod_{k=1}^{K} \frac{Z_{S,k}}{Z_{S,k}+Z_{R,k}}\right] \left\lvert f^{p}_{S,1}\right\rvert$	$f^{s}_{B_2,K} = 0$
$f_{B_3,K}$	$f^{so}_{B_3,K} = \left[\prod_{k=1}^{K-1} \frac{Z_{R,k}}{Z_{S,k}+Z_{R,k}}\right] \left\lvert f^{so}_{R,1}\right\rvert$	$f^{p}_{B_3,K} = 0$	$f^{st}_{B_3,K} = \left[\prod_{k=1}^{K} \frac{Z_{S,k}}{Z_{R,k}}\right] \left\lvert f^{st}_{S,1}\right\rvert$
$f_{B_4,K}$	$f^{so}_{B_4,K} = \left[\prod_{k=1}^{K-1} \frac{Z_{R,k}}{Z_{S,k}+Z_{R,k}}\right] \left\lvert f^{so}_{R,1}\right\rvert$	$f^{p}_{B_4,K} = \left[\prod_{k=1}^{K-1} \frac{Z_{S,k}}{Z_{S,k}+Z_{R,k}}\right] \left\lvert f^{p}_{S,1}\right\rvert$	$f^{st}_{B_4,K} = \left[\prod_{k=1}^{K-1} \frac{Z_{S,k}}{Z_{R,k}}\right] \frac{Z_{S,K}+Z_{R,K}}{Z_{R,K}} \left\lvert f^{st}_{S,1}\right\rvert$
$f_{B_5,K}$	$f^{so}_{B_5,K} = \left[\prod_{k=1}^{K} \frac{Z_{R,k}}{Z_{S,k}+Z_{R,k}}\right] \left\lvert f^{so}_{R,1}\right\rvert$	$s^{p}_{B_5,K} = \left[\prod_{k=1}^{K-1} \frac{Z_{S,k}}{Z_{S,k}+Z_{R,k}}\right] \frac{Z_{R,K}}{Z_{S,K}+Z_{R,K}} \left\lvert f^{p}_{S,1}\right\rvert$	$f^{st}_{B_5,K} = \left[\prod_{k=1}^{K-1} \frac{Z_{S,k}}{Z_{R,k}}\right] \left\lvert f^{st}_{S,1}\right\rvert$
$f_{B_6,K}$	$f^{so}_{B_6,K} = \left[\prod_{k=1}^{K-1} \frac{Z_{R,k}}{Z_{S,k}+Z_{R,k}}\right] \frac{Z_{S,K}}{Z_{S,K}+Z_{R,K}} \left\lvert f^{so}_{R,1}\right\rvert$	$f^{p}_{B_6,K} = \left[\prod_{k=1}^{K} \frac{Z_{S,k}}{Z_{S,k}+Z_{R,k}}\right] \left\lvert f^{p}_{S,1}\right\rvert$	$f^{st}_{B_6,K} = \left[\prod_{k=1}^{K} \frac{Z_{S,k}}{Z_{R,k}}\right] \left\lvert f^{st}_{S,1}\right\rvert$
$f_{B_7,K}$	$f^{so}_{B_7,K} = \left[\prod_{k=1}^{K} \frac{Z_{R,k}}{Z_{S,k}+Z_{R,k}}\right] \frac{Z_{S,K}}{Z_{P,K}} \left\lvert f^{so}_{R,1}\right\rvert$	$f^{p}_{B_7,K} = \left[\prod_{k=1}^{K} \frac{Z_{S,k}}{Z_{S,k}+Z_{R,k}}\right] \frac{Z_{R,K}}{Z_{P,K}} \left\lvert f^{p}_{S,1}\right\rvert$	$f^{st}_{B_7,K} = \left[\prod_{k=1}^{K-1} \frac{Z_{S,k}}{Z_{R,k}}\right] \frac{Z_{S,K}}{Z_{P,K}} \left\lvert f^{st}_{S,1}\right\rvert$

1.3. Failure diagnosis on epicyclic gearboxes: literature review

Diagnosis of epicyclic gearboxes through vibration analysis has been limited to the planetary configuration. Research has been carried out for the last three decades, aiming principally to provide a solution for the condition monitoring of the planetary gearbox used in the main rotor of helicopters. In this regard mainly gear failures and crack on the carrier plate have been considered; only isolated works address the diagnosis of bearing failures. In this section an overview of the results from the previous works is presented by making the division between gear failures, carrier plate crack and bearing failures.

1.3.1. Gear failures

McFadden and Smith first proposed a phenomenological model to describe the vibrations generated on a non-faulty planetary gearbox when measured with a fixed sensor mounted on the outer part of the ring gear [MS85]. They noticed that the vibrations measured by the sensor were mostly originated from the meshing processes taking place on the gearbox. They also noticed that the vibrations generated by the meshing process of each planet are amplitude modulated, increasing its amplitude when the planet approaches the sensor position and then decreasing as it moves farther. Interestingly, the vibration measured by the sensor, which is the sum of the vibrations generated by all planets, can have different spectral components depending on the geometric characteristics of the gearbox. They showed that this can even lead to the complete absence of the component at the gear mesh frequency, a phenomenon refered as suppression. In a later publication [McF91] it was postulated that although the sensor measures the sum of the vibrations generated by the meshing of each planet, when a certain planet is at the sensor position they are dominated by the vibrations coming from the meshing of this planet with the teeth of the ring gear nearest to the sensor. Based on this, an algorithm was proposed to separate the vibrations generated from the meshing of each planet with this teeth. Since at the sensor position all planets mesh with the same teeth of the ring, this method would provide a way of performing a differential diagnosis for each planet gear. It was also proposed that the method could be used for the separation of the vibrations generated by the meshing of each

planet with the sun gear.

Forrester [For01] proposed a modification to the method of McFadden and Smith for calculating the synchronous average of the separated signals in a faster form. Similarly, Blunt [Blu05] used the basic method for separating the vibration signals produced during the gearing between the sun and the planet gears and proposed a modified average vibration signal to perform diagnosis of the sun gear. Although the results presented are favorable, the use of these techniques is only possible in planetary gearboxes whose components fulfill certain geometric restrictions, thus lacking in generality. To overcome this limitation, Samuel et al. [SP03][SCP04] extended the technique to the use of multiple sensors mounted on the ring gear, under the assumption that "*the vibration signals measured by the transducers are nominally similar*". However it was concluded in the same work, that this assumption does not hold and the use of multiple sensors was not recommended. Mosher proposed an alternative method for signal separation using an inverted vibration model, however the results were irregular and it was concluded that more work is needed in this direction [Mos05].

In a different approach Shan [SBS99][Sha01] used the envelope spectrum of the vibration signal measured on the outer part of the ring gear to diagnose gear failures in a planetary gearbox. Different failures were seeded in the tooth flank of all gears of a planetary gearbox. Excluding the case of the failure in the ring gear, all failures were identified through analysis of the envelope spectrum. Moreover, the results were in accordance with a model previously developed by Shan. As a conclusion, symptoms for identifying the studied failures on a planetary gearbox were given. However, it is important to notice that Shan's model and measurements were made on a planetary gearbox which does not suffer from the suppression of the component at the gear mesh frequency and therefore encompass only one group of planetary gearboxes.

Recently Barszcz and Randall [BR09] used the kurtogram [AR06] to detect a crack in a ring gear tooth by analysing the vibration signals recorded with a commercial condition monitoring system. This was done after the system was unable to detect the failure, thus leading to a catastrophic failure of the planetary stage.

1.3.2. Carrier plate crack

Diagnosis of carrier plate crack in planetary gearboxes has also been carefully studied. The interest comes from the fact that it is a failure that has been observed several times in the planetary gearbox of helicopters. As a result, numerous scalar quantities (i.e. features) calculated differently from the vibration signal have been proposed for its detection. The principle behind them is basically the assumption that a crack in the carrier plate affects the torsional stiffness causing a local deformation near the crack. This, in turn, influences the angular position of the planet near the crack. A change in the angular position of a planet would produce a change in the phase of the vibration at the mesh frequency generated by the planet. Recalling that the spectral structure of the vibration measured is determined by the sum of the vibrations generated at each planet in which the phase of the gear mesh-related components play a critical role [MS85], the features are designed to detect changes in the spectrum which can be related to the carrier crack. Among the features, the modified sideband index and the modified sideband level factor are found. Although the results of these two features were favorable under laboratory conditions, they failed when used with real data [KG03]. Additionally Patrick-Aldaco pointed out that these features are system-dependent and therefore provide no capability of comparison. Further, the use of a series of condition indicators and the average of them was proposed. Contrary to the former, the indicators proposed by Patrick-Aldaco are based on relative amplitudes between spectral components, thus allowing system-to-system result comparison [PA07]. Similarly Wu et al. presented the harmonic index and the intra-revolution energy variance, the former calculated on the frequency domain and the latter on the wavelet domain, which he claimed were able to differentiate between the faulty and non-faulty case [WSK$^+$04][WSPV05].

On a recent publication, Bartelmus and Zimroz [BZ09] analysed the influence of the load variation in the vibration signal measured on the planetary gearbox of a bucket wheel excavator. They showed the influence of load to be larger when the planetary gearbox is damaged. However, the failure was not accurately described and was only refered to as “perturbation of the arm rotation”.

1.3.3. Bearing failures

Shan [Sha01] used the envelope spectrum of the vibration signal to detect seeded defects in the inner ring, outer ring and rolling element of the bearing of one planet gear without favorable results. It was indicated that the bearings used were needle bearings and that probably different results would be obtained, should other type of bearings have been used. Contrary, Randall [Ran04] was able to detect a rolling element failure in the planet bearing by using the envelope spectrum. Note that this is the same approach taken by Shan, but in this case a barrel roller bearing instead of a needle bearing was used. Further, the use of a self adaptive filter for the removal of the deterministic part of the signal was proposed. Thus, the masking effects of the gear mesh components are eliminated and the components due to the bearing failure are more clearly observed in the envelope spectrum. This proved to be effective when the rotational speed is relative stable. Sawalhi [SR06][Saw07] used a set of signal processing tools to identify a faulty planet bearing. This included angular resampling, removal of the gear mesh contribution, pre-whitening, spectral kurtosis, filtering, and envelope spectrum. Angular resampling made possible the removal of the gear mesh contribution under variable rotational speed conditions.

1.3.4. Summary

As presented in the preceding sections, different approaches have been taken for the diagnosis of distinct types of failures in a planetary gearbox with different results. In the case of the gear failures, though a careful analysis of the generated vibrations has been made, the proposed diagnosis techniques are only applicable under the fulfillment of certain (geometric) conditions. Differently, the features proposed for the diagnosis of carrier crack have a more general basis. Finally, although promising results have been recently reported for planet bearing failure diagnostics, they have been presented as application examples of novel algorithms for bearing failure detection in general. In this context, the algorithms have been applied to the case of planetary gearbox, but no thorough analysis of the vibration signals has been made.

To the knowledge of the author, there is no published work concerning the use of AE for failure diagnosis of EG. Moreover, no literature regarding the analysis of AE in EG for the non-faulty case has been found.

1.4. Vibrations and acoustic emissions generated on epicyclic gearboxes

1.4.1. Vibration phenomena in epicyclic gearboxes

1.4.1.1. Fundamentals of gear vibrations

The transmission error (TE) has been recognized as the main source of vibrations in geared transmissions [Har58][BH87][LTO89][Smi03]. The TE is defined as the difference between the actual position of the driven gear wheel and the position it would occupy if the gears were geometrically perfect and non-deformable. Three types of TE are distinguished:

- **Unloaded static transmission error (UsTE):** the UsTE comprehends the geometric imperfections or deviations from the perfect involute geometry of the gears. This includes manufacturing and mounting errors of the gear wheels and other components of the gearbox. It also includes tooth profile modifications such as addendum/dedendum modification, semitopping, etc.. The UsTE is measured under quasi-static conditions (low rotational speed) and with a very low torque, only to ensure the contact between the tooth flanks, so that no deformations of the gear teeth are produced.

- **Loaded static transmission error (LsTE):** besides the manufacturing errors, the LsTE includes the deviations from the perfect geometry of the gears due to the elastic and local deformations of the gears produced by the transferred load.

- **Dynamic transmission error (dTE):** the dTE takes into account the dynamic response of the system due to the excitation resultant from the LsTE. The dTE is of particular importance for gearboxes working at high rotational speeds. This type of TE is not considered in this thesis.

As illustrated in fig. 1.6, the principal sources of UsTE can be divided into tooth profile deviations from the true involute and gear wheel errors such as tooth spacing and gear wheel eccentricity. The tooth profile deviation can be further divided into a mean and a random contribution (fig. 1.7). The mean contribution is the amount of profile deviation that is present in

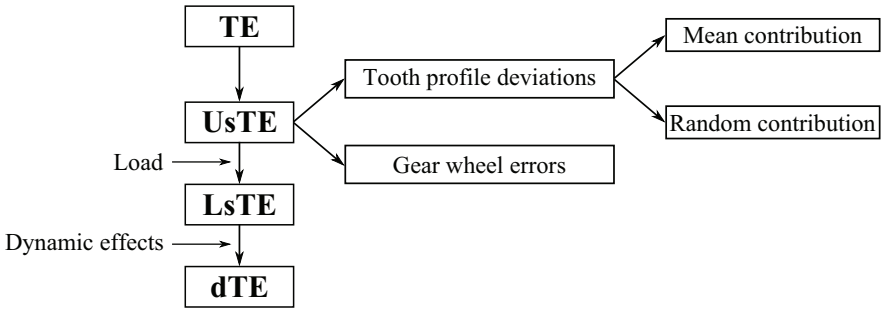

Figure 1.6: Representation of the transmission error.

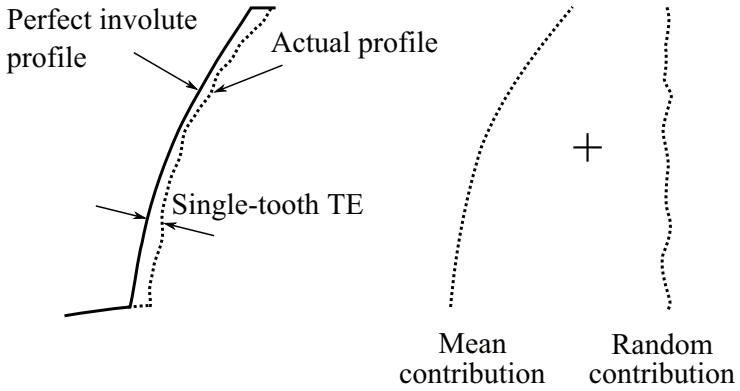

Figure 1.7: Decomposition of the tooth profile deviation.

all teeth of the gear wheel. It can be due to systematic errors during the manufacturing of the teeth, or to tooth profile modifications. The random contribution is the amount of profile deviation that varies from tooth to tooth. As the gears rotate, the mean contribution will produce a pattern in the UsTE that repeats as the different tooth pairs come into mesh. Eccentricity of one gear wheel will produce a pattern in the UsTE that repeats for every rotation of the gear wheel. Since tooth spacing error differs for different adjacent teeth, its effect on the UsTE will be the same as the eccentricity. The random deviation from the true involute of the teeth has a similar effect, although to a less extent. Figure 1.8 shows an example of how the UsTE of a gear with tip and root relief would typically look. Note the influence of the mean tooth profile deviation on the UsTE which produces the periodic pattern marked with θ_g; the component with period equal to one gear wheel revolution is possibly due to gear wheel eccentricity or teeth spacing error.

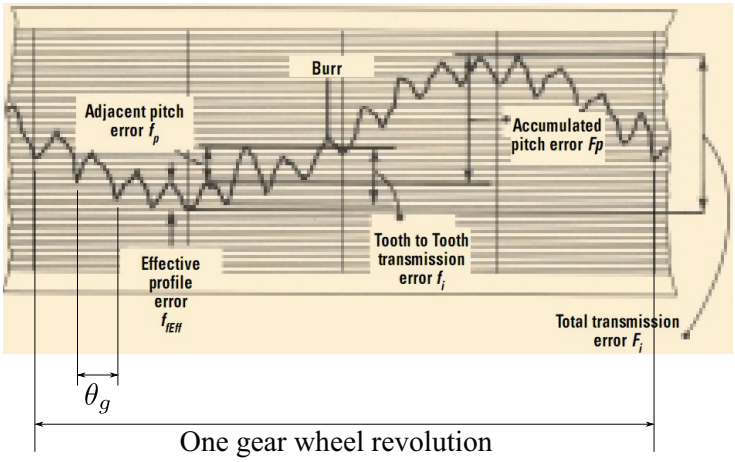

Figure 1.8: Example of single-flank measurement of the UsTE [Smi04].

As mentioned, the LsTE is a consequence of the gear deformation under load. The torque is transmitted from the driving to the driven gear wheel through forces acting on the tooth flanks in mesh. As the gears rotate, the points of contact between the flanks of the meshing teeth move along the line of action. Hence, the force acts at different locations on the tooth flanks: it moves from base to tip for the driving tooth and from tip to base for the driven tooth, as illustrated in fig. 1.9. For the same reason, the stiffness of a single tooth pair is dependent on the location of the point of contact (fig. 1.10a). Moreover, as the gear wheels rotate, the number of tooth pairs in contact varies according to the contact ratio. Thus, the stiffness during the meshing process can be determined by superimposing and adding the stiffnesses of each tooth pair (fig. 1.10b). Similarly, during the meshing process the load is transmitted by a varying number of tooth pairs, which means that the magnitude of the force acting on a single tooth pair is also variable (fig. 1.10c) [LHLC87]. Since it depends on the stiffness and the load, the LsTE will be variable during the rotation of the gear wheels. Its approximated shape is illustrated in fig. 1.10d. Note that the LsTE is periodic with a period equal to the gear mesh period. Note also the influence of the change in the number of tooth pair in contact which produces the sharp transitions in the stiffness, tooth load and LsTE.

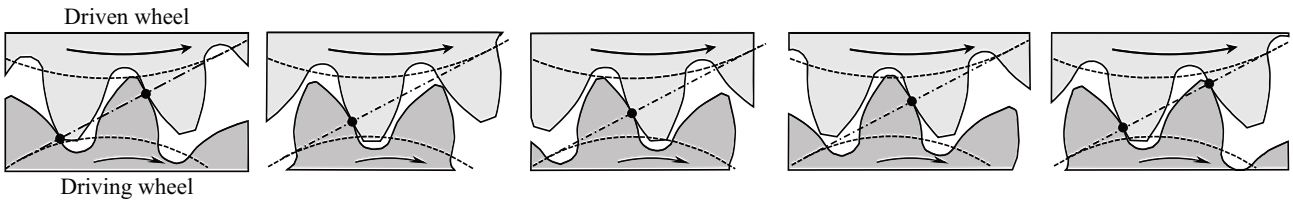

Figure 1.9: Progression of the gear mesh process. Dots represent the points of contact.

The TE can be interpreted as a displacement excitation with fundamental periods equal to the gear mesh period and the rotation of the gear wheels, as presented in fig. 1.11. This excitation produces reaction forces and vibrations on all components of the gearbox, in particular in the supporting bearings and in the case of the gearbox. Vibration and sound with the same fundamental periods are, therefore, normal to the operation of gearboxes.

Other possible sources of vibrations in a gearbox are tooth impact, fluid pumping and friction between the tooth flanks while meshing. It has been postulated that impacts occur when meshing teeth come into contact and start to take load. However, measurements taken on gears at operation conditions have shown no presence of shocks [Smi03]. Fluid pumping refers to the fluid that is trapped in the space between the tip and root of meshing teeth and is expelled axially producing impacts on other elements of the gearbox at the gear mesh frequency. The friction forces acting on the tooth flanks are perpendicular to the line of action. During the mesh period, they vary in magnitude and in sense (i.e. sign) after passing the pitch point, thus producing vibrations in the mentioned direction. They also produce moments that affect the rotation of the gear wheels and the tooth bending and, therefore, the LsTE [LP09][KLD07].

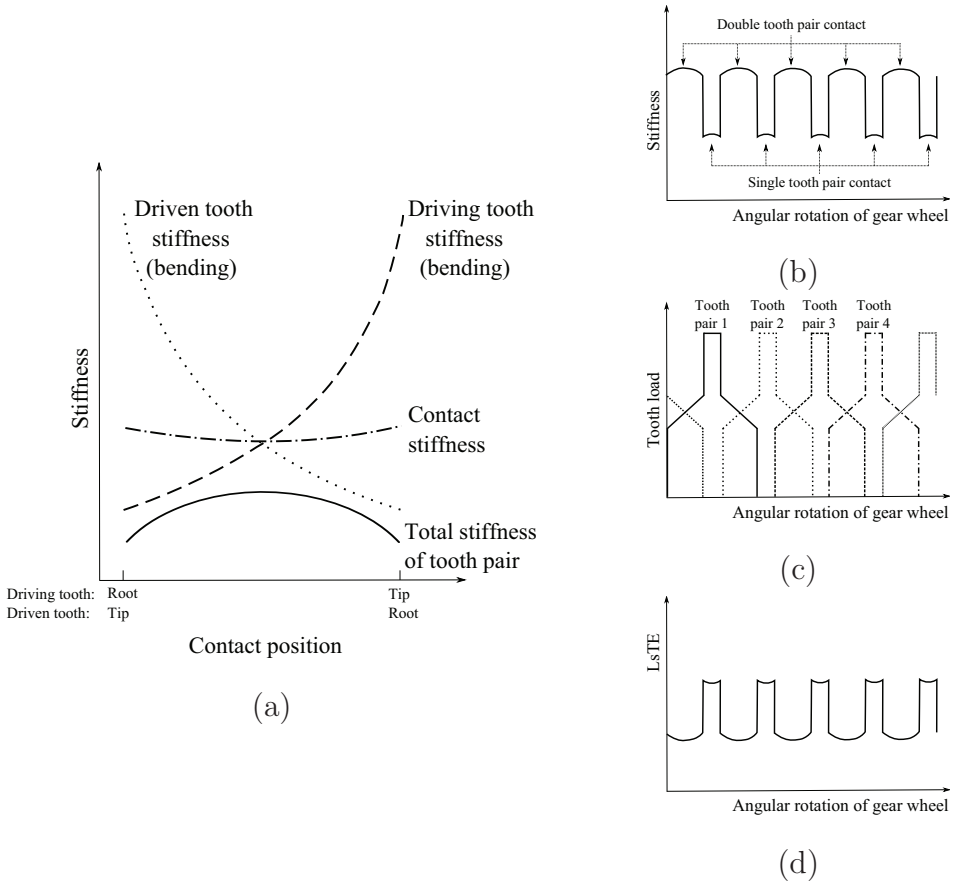

Figure 1.10: (a) Stiffness of a single tooth pair. (b) Stiffness during the meshing process. (c) Load during the meshing process. (d) LsTE during the meshing process.

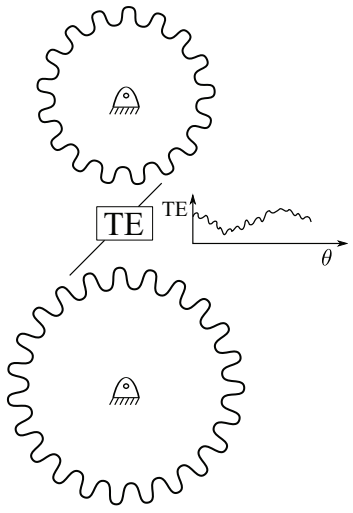

Figure 1.11: Interpretation of the TE as an displacement excitation acting between the gear wheels.

1.4.1.2. Sources of vibration in a non-faulty epicyclic gearbox

In an EG the number of meshing processes is equal to twice the number of planets N. They occur simultaneously, each generating vibrations. The source of the vibrations in each process is intrinsically the same as in fixed-axis gearboxes, namely the TE.

Additionally, in EG one half of the meshing processes are internal (i.e. meshing between the planet gears and the ring gear) while the other half are external. The vibrations generated in internal meshing differ from the vibrations generated in external meshing, principally because of:

- **Higher contact ratio:** due to the concave/convex geometry of the meshing, the contact line between meshing teeth is longer for internal than for external gears. Therefore, there is an increase in the time in which multiple tooth pair contact occur. The effects of the increase of the contact ratio are: *i*) the transfered load is distributed in more teeth and therefore the load acting on a single tooth pair is lower, *ii*) the total mesh stiffness is higher, and *iii*) in cases where the contact ratio is increased from a value of less than 2 to a value greater than 2, the sharp transitions in the stiffness, tooth load and LsTE (see fig. 1.10b-d) are eliminated. All this translates into a lower TE and therefore lower vibrations.

- **Lower friction:** there is less relative displacement between the surfaces of the meshing teeth in internal than in external gearing. This and the lower tooth load makes the influence of the friction force in the generation of vibrations to be less than in external gears.

- **Higher stiffness:** as shown in fig. 1.12, the tooth stiffness of an internal gear is higher than the tooth stiffness of the equivalent external gear. This is mainly because the base of the internal tooth is wider than its external counterpart. This means that for the same load, the amount of the LsTE is lower.

Although the vibrations generated in internal gears are lower than the vibrations generated in external gears, they still exist and share the same fundamental periods.

Hence, in an epicyclic gearbox N internal and N external mesh processes take place, each generating vibrations with slight differences in shape between the vibrations generated in the

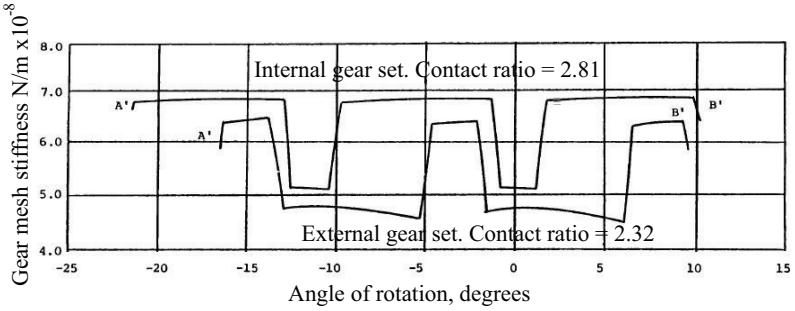

Figure 1.12: Example of gear mesh stiffnes for internal and external gears [PKFA83].

internal and external gearing. Except for the star configuration, as the planet gears revolve around the sun gear, the location of the point of contact between the meshing teeth also revolve around the sun gear. Since the vibrations are precisely generated at these points, this means that the location of the source of gear vibrations in an epicyclic gearbox (planetary and solar configurations) revolves around the sun gear. This is in contrast to fixed-axis gearboxes where the location of the source of vibrations remains fixed. This particular phenomenon and its influences on the analysis of vibrations of epicyclic gearboxes is thoroughly explained in chapter 2.

1.4.2. Acoustic emissions phenomena in epicyclic gearboxes

1.4.2.1. Fundamentals of acoustic emissions in gears

Acoustic emissions (AE) are high frequency transient elastic waves generated by the sudden release of energy due to strain or damage within or on the surface of a solid material, or by the interaction of two media in relative motion [MR06]. There are different opinions on the frequency range of AE, however it is usually accepted that they range between 100 kHz and 1 MHz. Typical sources of AE include impacts, friction, turbulence, leakage, material loss, cavitation, etc. The main advantages and disadvantages of the use of AE in condition monitoring are:

- **Advantages:**
  - AE are non-directional, therefore usually only one sensor suffices,

  - AE are very sensitive to micro physical phenomena, thus offering good possibilities for early-stage failure detection,
  - the frequency of the AE transient wave is dependent on the material characteristics rather than on the rotational speed of the machine. Based on this, it has been reported that AE offers good chances for monitoring low-speed rotating machinery [EM09],
  - mechanical noise has low amplitude in the range of AE, which means the signal has a high signal-to-noise ratio.

- **Disadvantages:**
  - The AE waves travel from the source in all directions reducing its amplitude as the distance from the source increases, a phenomenon termed **attenuation**,
  - AE are sensitive to interfaces. When the waves meet changes in the propagation medium (e.g. interfaces or changes of material), only one part of the AE wave is further transmitted and other part is **reflected**.

These two disadvantages can in some cases be diminished by placing the sensor near the AE source.

Besides the frequency range, what differentiates AE and vibrations is the mechanism of generation. As explained in section 1.4.1.1 the mechanism of generation of the vibrations is the TE. In the case of AE, the principal mechanism of generation is asperity contact between the surfaces of the meshing teeth. The mechanism of generation of the AE activity during the meshing process and the influence of the working condition is at present a very active field of research. Several researchers currently agree that the rolling portion of the gear mesh period is responsible for the burst-type AE activity, whereas the sliding portion is responsible for the continuous-type AE activity [TM05][HM09]. Figure 1.13 shows a portion of the time history of a typical AE signal measured on a gearbox where the presence of burst at the gear mesh period T_g with a continuous background is evidenced.

AE are influenced by the following parameters:

- **Surface roughness:** higher roughness of the tooth surfaces produces more asperity contact and, therefore, higher levels of AE.

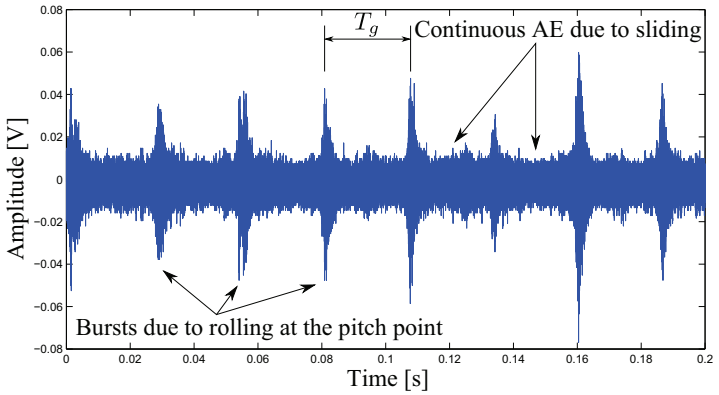

Figure 1.13: Typical time history of AE signal measured on a spur gearbox.

- **Temperature:** the lubricant film thickness is influenced by temperature [DH77]. A higher temperature results in a thinner film and, thus, in a higher rate of asperity contact, which produces higher levels of AE.

- **Speed:** the speed has two contrary effects on the AE. First, as the speed increases the lubricant film thickness increases, which results in less asperity contact and lower AE levels. On the other hand, an increase in the speed results in an increase in the rate of asperity contact, which results in higher AE levels. Different results can be found on different gearboxes depending on the degree of influence of both effects on the AE.

- **Load:** an increase in the load results in a decrease in the film thickness, and thereby an increase in the asperity contact, thus producing higher AE levels.

The influence of these parameters on the AE can be considerable and therefore should be taken into account in the analysis of AE signals from gearboxes.

Other possible sources of AE during the meshing process are *i*) viscous shearing of lubricant, *ii*) elastic deformation of gear tooth, and *iii*) pressure peak of lubricant [TM04][DH77]. However, these have not yet been proved.

1.4.2.2. Sources of acoustic emissions in a non-faulty epicyclic gearbox

Similarly to the case of vibrations, AE are produced on each of the $2N$ mesh processes ocurring in an epicyclic gearbox. Since the sliding/rolling behaviour between internal and external

gearing differ, differences in the shape and amplitude of the AE generated in the internal and external gear processes can be expected. As the gears rotate, the location of the sources of generation of AE –i.e. the points of contact between teeth– will revolve around the sun gear (except for the star configuration). As in the case of vibrations, this will influence the AE measured by the sensor.

2. Novel model for the vibrations and AE generated on an epyciclic gearbox

2.1. Introduction

Models of mechanical systems or mechanical components are widely used in the field of machine diagnosis. The objective of the models is to describe the behaviour of the system of interest for the required conditions as close to reality as possible. Essentially, the models consist of a collection of mathematical equations which describe the physical laws governing the system.

It is advantageous to have a reliable and accurate model of a system, because it provides a cost-efficient way of evaluating the response of the system under different conditions. Furthermore, constructive modifications and its influences on the behaviour of the system can be analysed [SW76]. In the case of machine diagnosis, the models provide a very convenient way to develop and test new signal processing tools for failure diagnosis. As an additional advantage, the process of developing a model involves a detailed study of the system, so that a deep knowledge of the system is inevitably accomplished.

Sometimes, the physical processes involved in the system can be so complex, that no mathematical equations are available for describing them. In the modelling of mechanical systems, even the most simple cases can involve high complex interactions like friction, lubrication, parametric excitations, non-linearities, etc. If the physical processes can not be realistically modelled, the results obtained from the model are not as useful as desired.

Phenomenological models have emerged as a possible solution to this difficulty. Phenomenological models are not based on the theory or physical laws behind the phenomena; they aim to mathematically describe the processes under study based on empirical observations. In the

case of machine diagnosis, the process under study can be, for example, the vibrations or AE measured on the case of a gearbox, the torque measured on the output shaft, lubricant temperature or pressure, etc. In order to do this, phenomenological models make use of statistical functions –rather than differential equations– to describe the **output** of a system.

In the following sections, phenomenological models are developed for the vibrations and acoustic emissions measured on a planetary gearbox with a sensor mounted on the outer part of the ring gear. This situation the most typical situation found in the industry. However, models for other configurations of epicyclic gearboxes, or other measurement points can be easily developed by taking the development of the presented models as a basis and making the appropriate considerations.

2.2. Vibration model for planetary gearboxes

It was shown on chapter 1.4, that the vibrations in gears are caused by the TE. It was also shown, that the TE is a periodic function with a fundamental period equal to the gear mesh period, with possible modulations at the rotational speed of the gear wheels. Therefore, in a fixed-axis gearbox, the frequency spectrum of the vibrations measured with a sensor mounted on the gearbox case consists typically of several components at the gear mesh frequency f_g and harmonics, each with possible sidebands at the rotational frequency of the gear wheels f_1 and f_2 –see fig. 2.1. Although the number of components present in the spectrum and its amplitudes can vary depending on the particular shape of the TE, the *spectral structure* of the vibrations shown in fig. 2.1 is *roughly* the same for all fixed-shaft gear transmissions. Naturally, the frequency of the components vary according to the rotational speed of the gear wheels and their number of teeth.

It will be shown in the following sections that this feature of having a *unique spectral structure* is not shared by epicyclic gearboxes where, depending on geometrical characteristics, different spectral structures can be found.

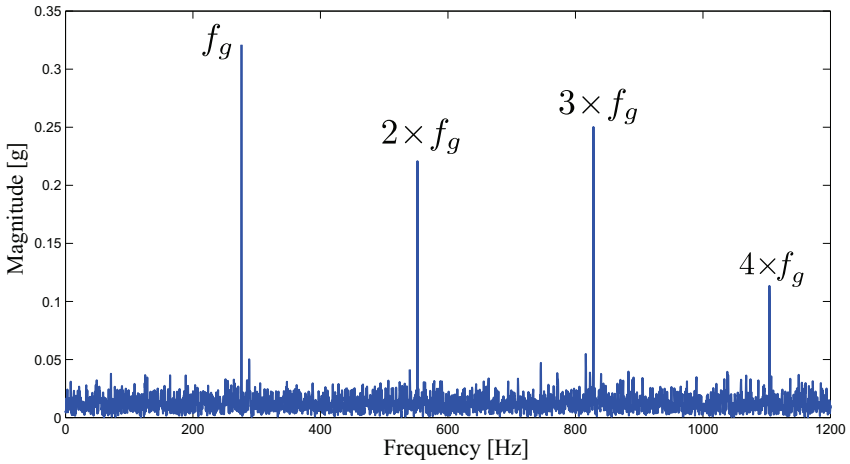

Figure 2.1: Example of frequency spectrum of a fixed-axis gearbox.

2.2.1. Model development

The model is developed for the vibrations generated in a planetary gearbox (PG), which are measured by a sensor mounted on the outer part of the fixed ring gear, as indicated in fig. 2.2.

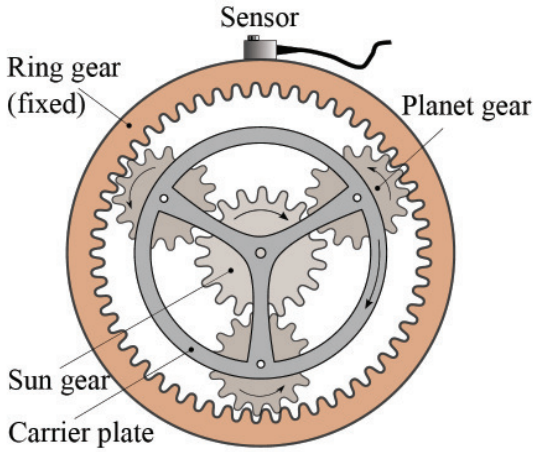

Figure 2.2: Measurement arrangement on a single-stage planetary gearbox.

The planetary configuration is the most widely used of the configurations of epicyclic gearboxes, and the measurement arrangement of fig. 2.2 represents the most typical case. For the afore mentioned reason, the model is developed only for this case.

As a first approximation, following assumptions are made:

(i) vibrations are only generated in the planet-ring meshing processes,

(ii) the vibrations generated in each planet-ring meshing are periodic, have the same amplitude and have no amplitude modulation, and

(iii) the vibrations are transmitted to the sensor through the ring gear only.

These assumptions are relaxed later, during the development of the model.

First, the vibrations as seen by an observer rotating with the carrier plate are considered. The observer experiences the vibrations $v_i^r(t)|_{i=1,\dots,N}$ coming from the meshing of each of the N planet gear wheels with the ring gear. All these vibrations are a consequence of the TE between the i-th planet and the ring gear. Hence, they are considered periodic with fundamental frequency f_g^p. The relative phase between the vibrations $v_i^r(t)|_{i=1,\dots,N}$, however, can differ according to the assembly characteristics of the gearbox. Taking the pitch point as a reference, this means that the contact at the pitch point of each planet-ring meshing process can take place at different times. The phase difference γ_{ri} between the vibration generated in the meshing of i-th planet gear with the ring gear $v_i^r(t)$ and the vibration generated on the meshing of the first

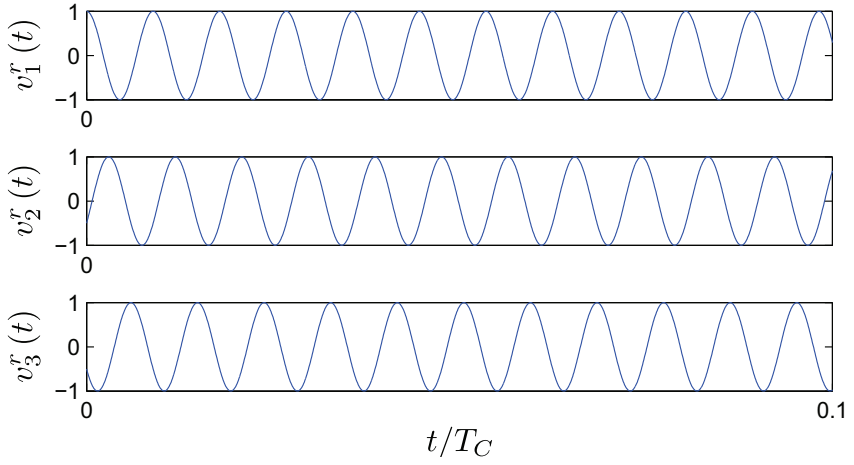

Figure 2.3: Illustration of $v_i^r(t)$ for a planetary gearbox with $Z_R = 112$ and $\psi_i = 0$; $2\pi/3$ and $4\pi/3$.

planet gear with the ring gear $v_1^r(t)$, depends on the relative angular position of both planets around the sun gear. Since the planet gears can only be assembled at angular positions ψ_i that are integer multiples of $\Delta\psi = 2\pi/(Z_S + Z_R)$ [PL04], γ_{ri} is specific for each planetary gearbox. The angular pitch[1] of the ring gear is given by $\angle_R = 2\pi/Z_R$. Thus, the phase difference γ_{ri} between $v_i^r(t)$ and $v_1^r(t)$ can be calculated as follows:

$$\gamma_{ri} = \frac{\psi_i}{\angle_R} = \frac{\psi_i Z_R}{2\pi} \tag{2.1}$$

where ψ_i is the relative angle between the position of the i-th planet gear and the first planet gear ($\psi_1 = 0°$). Thus, the vibration generated on the i-th meshing process as seen by the observer in the carrier plate $v_i^r(t)$ can be written as a time-shifted version of the vibration generated on the first planet $v_1^r(t)$, by taking their phase difference into account:

$$v_i^r(t) = v_1^r\left(t - \gamma_{ri} T_g^p\right) \tag{2.2}$$

where $T_g^p = 1/f_g^p$ is the gear mesh period. Fig. 2.3 schematically shows the vibrations $v_i^r(t)$ as seen by the observer standing at and rotating with the carrier of a planetary gearbox.

As the carrier plate rotates, the point of generation of the vibration $v_i^r(t)$ moves with respect to the sensor, which remains fixed. The variable distance between the point of generation of

[1]The angular pitch of a gear wheel is the angle determined by the length along the pitch circle between corresponding flank points of adjacent teeth

the vibrations $v_i^r(t)|_{i=1,\dots,N}$ and the sensor produces a variable transmission path that acts as an amplitude modulation function of the vibrations $v_i^r(t)|_{i=1,\dots,N}$. Consequently, the sensor experiences an increase in the amplitude of $v_i^r(t)$ as the i-th planet approaches the sensor position. Likewise, it experiences a decrease in the amplitude of $v_i^r(t)$, as the planet moves away from the sensor. Thus, the amplitude modulation function $a_i^r(t)$ is periodic with fundamental frequency f_C.

Since all vibrations $v_i^r(t)|_{i=1,\dots,N}$ are transmitted through the ring gear, the amplitude modulation function $a_i^r(t)$ of the vibration generated on the i-th planet gear can be expressed as a time-shifted version of the amplitude modulation function of the first planet by taking the relative angular position of the planets ψ_i into account:

$$a_i^r(t) = a_1^r\left(t - \frac{\psi_i T_C}{2\pi}\right) \tag{2.3}$$

The shape of $a_i^r(t)$ can be difficult to determine. However, for the frequency analysis of the vibrations measured by the sensor, it is its periodicity what is decisive. In this work, a bell-shaped amplitude modulation function $a_i^r(t)$ such as the illustrated in fig. 2.4a is used. The individual amplitude-modulated vibrations as seen by the sensor $x_i^r(t) = a_i^r(t)\, v_i^r(t)$ are illustrated in fig. 2.4b.

The vibrations generated in the meshing process of all planet gears with the ring gear occur simultaneously, therefore the sensor measures the sum of all amplitude modulated vibrations:

$$x^r(t) = \sum_{i=1}^{N} x_i^r(t) = \sum_{i=1}^{N} a_i^r(t)\, v_i^r(t) = \sum_{i=1}^{N} a_1^r\left(t - \frac{\psi_i T_C}{2\pi}\right) v_1^r\left(t - \gamma_{ri} T_g^p\right) \tag{2.4}$$

Note that eq. (2.4), which is illustrated in fig. 2.5, considers that the first planet is at the sensor position at $t = 0$. This is also clear from the plot of $a_1^r(t)$ in fig. 2.4a. However, in a more realistic scenario, the position of the first planet is unknown when starting a measurement. To account for this, a time shift t_1 is introduced to the amplitude modulating functions of equation (2.4). Fig. 2.6 illustrates the situation at the moment where the measurement is started. The time shift t_1 depends on the angular position of the first planet with respect to the sensor at the beginning of the measurement θ_1 and on the rotational frequency of the carrier plate, and is given by $t_1 = \frac{\theta_1}{2\pi f_C}$. However, since θ_1 is –in most of the cases– not known, the notation t_1 is

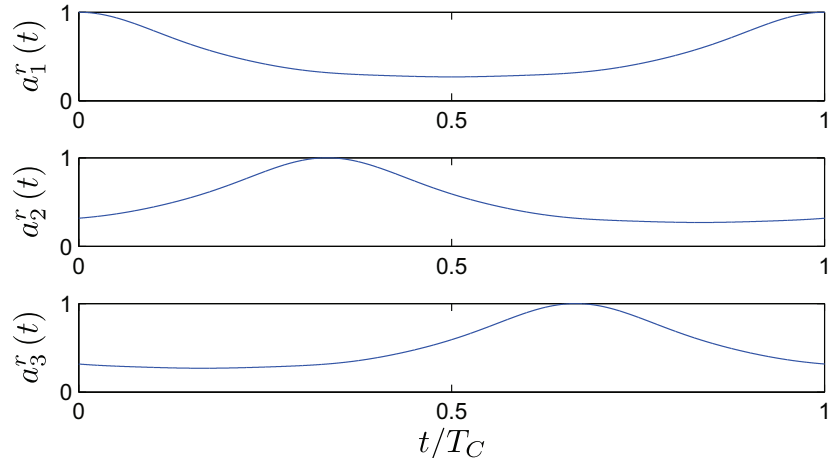

(a)

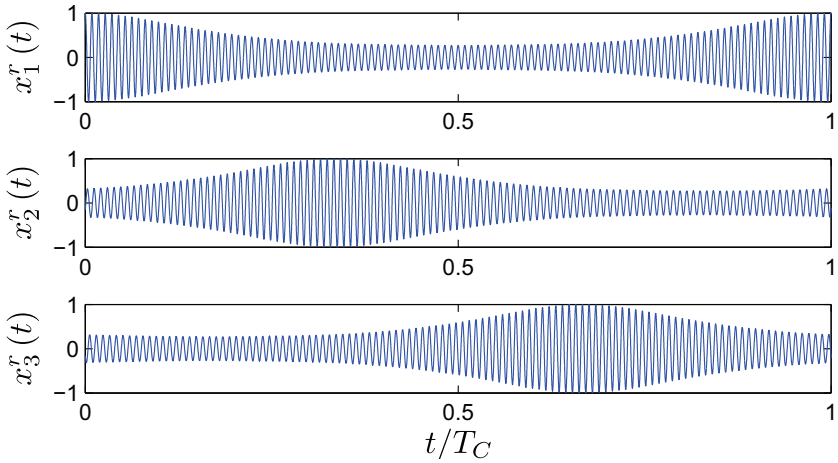

(b)

Figure 2.4: Illustration of (a) $a_i^r(t)$ and (b) $x_i^r(t) = a_i^r(t)\, v_i^r(t)$ for a planetary gearbox with $Z_R = 112$ and $\psi_i = 0;\ 2\pi/3$ and $4\pi/3$.

kept and eq. (2.4) becomes:

$$x^r(t) = \sum_{i=1}^{N} a_1^r\left(t - t_1 - \frac{\psi_i T_C}{2\pi}\right) v_1^r\left(t - \gamma_{ri} T_g^p\right) \tag{2.5}$$

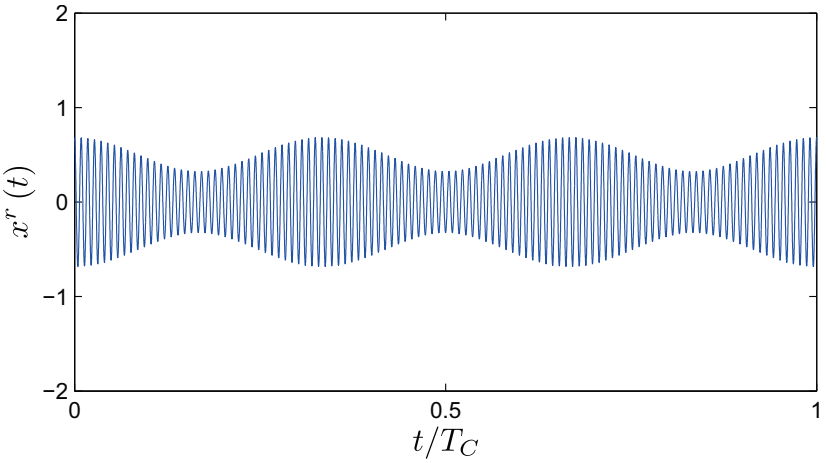

Figure 2.5: Illustration of $x^r(t)$ for a planetary gearbox with $Z_R = 112$ and $\psi_i = 0$; $2\pi/3$ and $4\pi/3$.

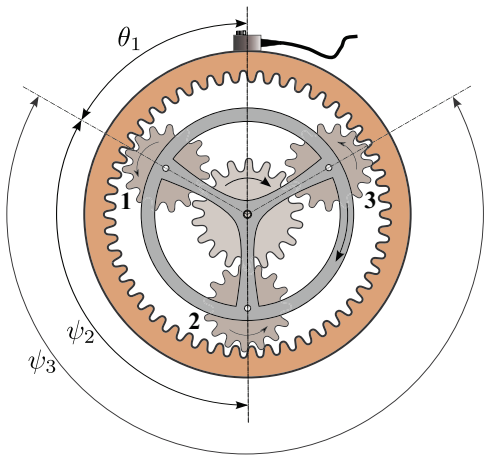

Figure 2.6: Position of the planet gears at the beginning of the measurement.

2.2.2. Frequency analysis

The frequency analysis of the vibrations measured by the sensor –eq. (2.5)– is performed through the calculation of the Fourier transform (FT). Considering the planetary gearbox as a linear system, the FT of eq. (2.5) is given by:

$$\begin{aligned} x^r(t) \overset{\mathcal{F}}{\longleftrightarrow} X^r(f) &= \sum_{i=1}^{N} X_i^r(f) \\ &= \sum_{i=1}^{N} \underbrace{\mathcal{F}\left\{a_1^r\left(t - t_1 - \frac{\psi_i T_C}{2\pi}\right)\right\}}_{\text{(I)}} * \underbrace{\mathcal{F}\left\{v_1^r\left(t - \gamma_{ri} T_g^p\right)\right\}}_{\text{(II)}} \end{aligned} \tag{2.6}$$

where $\mathcal{F}\{\cdot\}$ represents the FT, and $*$ represents the convolution product. As observed in eq. (2.6), $X^r(f)$ is composed of the sum of N convolution products between the terms marked as (I) and (II) in eq. (2.6).

Term (I):

As mentioned in section 2.2.1, $a_i^r(t)$ is periodic with a fundamental frequency equal to the rotational frequency of the carrier plate f_C. Therefore, it can be expressed as a Fourier series as follows:

$$a_i^r(t) = a_1^r\left(t - t_1 - \frac{\psi_i T_C}{2\pi}\right) = \sum_{q\in\mathbb{Z}} a_q^r e^{j2\pi q f_C\left(t - t_1 - \frac{\psi_i T_C}{2\pi}\right)} \tag{2.7}$$

where a_q^r, $q \in \mathbb{Z}$ are the Fourier coefficients of $a_1^r(t)$

Taking the FT of eq. (2.7) and using the time-shifting property of the FT, the following result is obtained for the term (I):

$$\mathcal{F}\left\{a_1^r\left(t - t_1 - \frac{\psi_i T_C}{2\pi}\right)\right\} = \sum_{q\in\mathbb{Z}} a_q^r e^{-j2\pi q f_C\left(t_1 + \frac{\psi_i T_C}{2\pi}\right)} \delta(f - q f_C) \tag{2.8}$$

where $\delta(z) = 1$, if $z = 0$; and $\delta(z) = 0$, if $z \neq 0$.

Term (II):

Likewise, $v_i^r(t)$ is considered periodic with a fundamental frequency equal to the gear mesh frequency f_g^p and can be expressed as a Fourier series:

$$v_i^r(t) = v_1^r\left(t - \gamma_{ri}T_g^p\right) = \sum_{k\in\mathbb{Z}} v_k^r e^{j2\pi k f_g^p\left(t-\gamma_{ri}T_g^p\right)} \tag{2.9}$$

where v_k^r, $k \in \mathbb{Z}$ are the Fourier coefficients of $v_1^r(t)$.

Taking the FT of eq. (2.9), the following expression for the term (II) is obtained:

$$\mathcal{F}\left\{v_1^r\left(t - \gamma_{ri}T_g^p\right)\right\} = \sum_{k\in\mathbb{Z}} v_k^r e^{-j2\pi k f_g^p \gamma_{ri}T_g^p}\delta\left(f - kf_g^p\right) \tag{2.10}$$

Substituting the eqs. (2.8) and (2.10) into eq. (2.6) and solving yields eq (2.11).

$$X^r(f) = \sum_{k\in\mathbb{Z}}\sum_{q\in\mathbb{Z}}\sum_{i=1}^{N} a_q^r v_k^r e^{-j2\pi q f_C t_1} e^{-j(kZ_R+q)\psi_i}\delta\left(f - kf_g^p - qf_C\right) \tag{2.11}$$

The term $\delta\left(f - kf_g^p - qf_C\right)$ in eq. (2.11) implies that $X^r(f)$ can take non-zero values only for the frequency set $f = kf_g^p + qf_C$ with k, $q \in \mathbb{Z}$. Furthermore, for planetary gearboxes with equally spaced planet gears, the term $e^{-j(kZ_R+q)\psi_i}$ in eq. (2.11), which determines the phase departing from $2\pi q f_C t_1$ of the i-th spectral component at $f = kf_g^p + qf_C$, becomes:

$$e^{-j(kZ_R+q)\psi_i} = e^{-j2\pi(i-1)\left[\frac{kZ_R+q}{N}\right]} \tag{2.12}$$

It is clear from eq. (2.12) that the exponential term acts as a sampling function, as it yields non-zero values only for values of $(kZ_R + q)$ that are integer multiples of N. Thus, the spectral components at the gear mesh frequency f_g^p and multiples ($k = 1, 2, ...$ and $q = 0$) will exist only if the quotient Z_R/N is an integer. This is in accordance to the results from [MS85], although the interpretation presented in this thesis is somewhat different.

Note also from eq. (2.12) that if $(kZ_R + q)/N \in \mathbb{Z}$, the N spectral components will be in-phase (i.e. they will add constructively) and, thus, eq. (2.11) can be written as:

$$X^r(f) = \begin{cases} N a_q^r v_k^r e^{-j2\pi q f_C t_1}\delta\left(f - kf_g^p - qf_C\right) & \text{, if } \frac{kZ_R+q}{N} \in \mathbb{Z} \\ 0 & \text{, elsewhere} \end{cases} \tag{2.13}$$

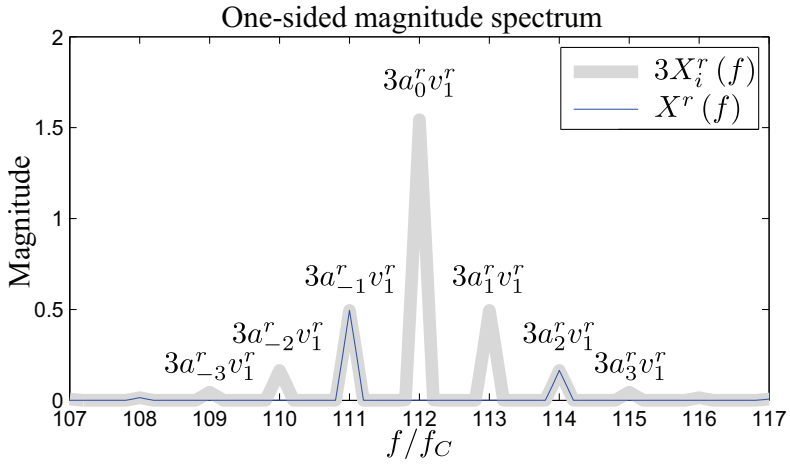

Figure 2.7: Portion around the first gear mesh component (i.e. $k = 1$) of the spectrum of the total vibrations measured by the sensor $X^r(f)$ (thin line) and the N-scaled spectrum of the single-planet vibrations $X_i^r(f)$ (thick line) for a planetary gearbox with $Z_R = 112$ and $\psi_i = 0;\ 2\pi/3$ and $4\pi/3$.

The portion around the first gear mesh component (i.e. $k = 1$) of the spectrum of the vibrations measured by the sensor –eq. (2.13)– for a planetary gearbox with $Z_R = 112$ and $\psi_i = 0;\ 2\pi/3$ and $4\pi/3$ is illustrated in fig. 2.7 (thin line). In the same figure, the N-scaled version of the spectrum of the single-planet vibrations $X_i^r(f)$ is illustrated (thick gray line). It is noted that the spectrum of the vibrations measured by the sensor has amplitude zero at the normalised gear mesh frequency ($f/f_C = 112$). The figure also illustrates that the spectrum of the vibrations of a planetary gearbox with N equally spaced planet gears can be interpreted as the sampled version at frequencies $f/f_C = pN$ (where $p \in \mathbb{N}_0$) of the N-scaled version of the spectrum of the vibrations coming from a single planet $X_i^r(f)$. This observation is in accordance with the one provided in [McN02], and explains the amplitude assymetry sometimes observed in the spectrum of the total vibrations $X^r(f)$.

2.2.3. Analysis of the spectral structure

From the frequency analysis of section 2.2.2, it is easy to see that the spectral structure $X^r(f)$ of the vibrations measured by the sensor is dependent on the geometrical characteristics of the PG. Incidentally, a very recent publication [IK09] has also described this issue. Moreover the authors have classified the PG in five groups, according to their *sideband behaviour*. Further, a vibration model and the results of the FFT[2] algorithm applied to this model were used to

[2]FFT: Fast Fourier Transform

describe the specific spectral characteristics of each group. However, the analysis of the **root cause** of the different spectral structures observed was not performed. The aim of this section is to provide such analysis and, through this, to expand the coverage of [IK09].

According to [IK09], the PG can be classified in the following groups corresponding to the spectral structure of its measured vibrations:

(i) PG with equally spaced planet gears and in-phase gear meshes;

(ii) PG with equally spaced planet gears and sequentially phased meshes;

(iii) PG with unequally spaced planet gears and in-phase gear meshes;

(iv) PG with unequally spaced planet gears and sequentially phased meshes;

(v) PG with unequally spaced planet gears and arbitrarily phased meshes.

The *sequentially phased* condition is defined in [IK09] as the case when "*the sum of the phase angles is an integer multiple of* π". The author believes that this definition is inexact and instead the following should be used: "*the phase angle of the gear meshes is equally distributed in the range* $[0, 2\pi)$". Moreover, since it can be demonstrated that this new definition of sequentially spaced gear meshes is the only possible condition for PG of group (ii), the author believes that a more general and appropriate classification is the following:

(A) PG with equally spaced planet gears and in-phase gear meshes;

(B) PG with equally spaced planet gears and out-of-phase gear meshes;

(C) PG with unequally spaced planet gears and in-phase gear meshes;

(D) PG with unequally spaced planet gears and out-of-phase gear meshes.

In the following lines, the frequency analysis of each of these new defined groups is presented.

Group (A): *PG with equally spaced planet gears and in-phase gear meshes*

The planet gears are equally spaced, so that $\psi_i = 2\pi\,(i-1)\,/N$ and eq. (2.1) becomes:

$$\gamma_{ri} = \frac{\psi_i Z_R}{2\pi} = \frac{Z_R}{N}\,(i-1) \tag{2.14}$$

Since all meshes are in phase, γ_{ri} must be either zero or an integer (i.e. $\gamma_{ri} \in \mathbb{N}_0$). It is clear from eq. (2.14) that this requires Z_R/N to be an integer (i.e. $Z_R/N \in \mathbb{N}$).

Let us now analyse the spectral structure of the vibrations through the evaluation of the second exponential term of eq. (2.11), which can be rearranged as follows:

$$e^{-j(kZ_R+q)\psi_i} = e^{-j2\pi(i-1)\left[\frac{kZ_R}{N}+\frac{q}{N}\right]} \tag{2.15}$$

Since $Z_R/N \in \mathbb{N}$ and $q \in \mathbb{Z}$; if q is an integer multiple of the number of planet gears N, the phase of the N spectral components will be an integer multiple of 2π, which means that the N components are in-phase. In this case the spectral components add constructively, so that the component will be present in the spectrum $X^r\,(f)$ with an amplitude given by $Na_q^r v_k^r$. The same occurs for the spectral components at the gear mesh frequency f_g^p (i.e. for $q = 0$). Contrary, if q is not an integer multiple of N, the phases of the spectral components are equally distributed in the range $[0, 2\pi)$, so that they add destructively and the amplitude of the component in the spectrum is zero. As a result, the spectral structure consists of components at the gear mesh frequency and multiples, each with symmetrical sidebands spaced by Nf_C; mathematically:

$$X^r\,(f) = \begin{cases} Na_q^r v_k^r e^{-j2\pi q f_C t_1}\delta\left(f - kf_g^p - qf_C\right) & \text{, if } \frac{q}{N} \in \mathbb{N} \\ 0 & \text{, elsewhere} \end{cases} \tag{2.16}$$

The spectrum of eq. (2.16) is illustrated in fig. 2.8 for a PG with $Z_R = 72$ and three equally spaced planets. In this figure, the presence of the components at the gear mesh frequency f_g^p and harmonics are clearly observed, each with sidebands at $3 \times f_C$. The magnitude of each component in the spectrum can be calculated by using eq. (2.16), provided the Fourier coefficients a_q^r and v_k^r are known. For example, for $f/f_C = 72$, the Fourier coefficients used are $a_0^r = 0.2554$ and $v_1^r = 1$. From eq. (2.16), since $N = 3$, the magnitude in the spectrum of the component at $f = f/f_C$ is equal to $0.2554 \times 1 \times 3 = 0.7663$, as shown in fig. 2.8.

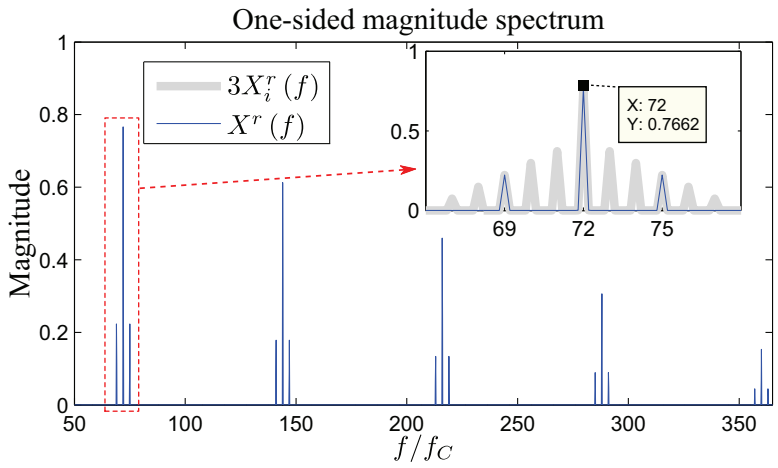

Figure 2.8: Illustration of the spectral structure of a PG of group (A) ($Z_R = 72$ and $N = 3$).

Group (B): *PG with equally spaced planet gears and out-of-phase gear meshes*

Here the planets are also equally spaced, so that $\psi_i = 2\pi\,(i-1)\,/N$ and $\gamma_{ri} = Z_R\,(i-1)\,/N$. However, in this group the meshes are not in-phase, which requires Z_R/N to be a non-integer. Hence, the second exponential term of eq. (2.11) can be conveniently written as:

$$e^{-j(kZ_R+q)\psi_i} = e^{-j2\pi(i-1)\left[\frac{kZ_R+q}{N}\right]} \tag{2.17}$$

From eq. (2.17) is clear that if $\left[\frac{kZ_R+q}{N}\right]$ is an integer, the N components will be in-phase, so that they will add constructively and the component will be present in the spectrum $X^r(f)$ with an amplitude of $Na_q^r v_k^r$. On the other hand, if $\left[\frac{kZ_R+q}{N}\right]$ is a non-integer, then the phase of the N components will be equally distributed in $[0, 2\pi)$, so that they will add destructively. Planetary gearboxes from this group present a spectrum without component at the gear mesh frequency f_g^p, but with an assymetrical distribution of components both in frequency and amplitude around the axis defined by f_g^p and spaced by Nf_C. Moreover, the frequency distribution of the components around the axis defined by the harmonics of f_g^p differs from the distribution around f_g^p, but their relative distance remains the same. Evidently, the N-th harmonics of f_g^p -if present in the vibrations- will be present in the spectrum. As a special case, if rem $\{Z_R; N\} = 1/2$, all $N/2$-th harmonics of f_g^p will be present in the spectrum[3].

At first sight, all this might appear very complex. This can be clarified by means of an example. Let us consider a planetary gearbox with five equally spaced planet gears and $Z_R = 126$, which

[3]where rem $\{a; b\}$ gives the remainder of a/b

corresponds to the example given in the case (ii)-(c) of [IK09]. Let us now accomodate the exponential term from eq. (2.17) as follows:

$$e^{-j2\pi(i-1)\left[\frac{kZ_R+q}{N}\right]} = \underbrace{e^{-j2\pi(i-1)k\frac{Z_R}{N}}}_{(i)}\underbrace{e^{-j2\pi(i-1)\frac{q}{N}}}_{(ii)} \tag{2.18}$$

It is observed in eq. (2.18) that the phase of term (i) depends on the values of i and k, while the phase of term (ii) depends on i and q. Table 2.1 shows the phase in the range $[0, 2\pi)$ of the term (i) for the N components and for $k > 0$. Similarly, the table 2.2 shows the phase in the range $[0, 2\pi)$ of the term (ii) for the N components.

Table 2.1: Phase of the term (i) of eq. (2.18) for the N components.

k	Phase expression	Phase in the range $[0, 2\pi)$				
		$i = 1$	$i = 2$	$i = 3$	$i = 4$	$i = 5$
1	$2\pi\,(i-1)\,126/5$	0	$\frac{1}{5}2\pi$	$\frac{2}{5}2\pi$	$\frac{3}{5}2\pi$	$\frac{4}{5}2\pi$
2	$4\pi\,(i-1)\,126/5$	0	$\frac{2}{5}2\pi$	$\frac{4}{5}2\pi$	$\frac{1}{5}2\pi$	$\frac{3}{5}2\pi$
3	$6\pi\,(i-1)\,126/5$	0	$\frac{3}{5}2\pi$	$\frac{1}{5}2\pi$	$\frac{4}{5}2\pi$	$\frac{2}{5}2\pi$
4	$8\pi\,(i-1)\,126/5$	0	$\frac{4}{5}2\pi$	$\frac{3}{5}2\pi$	$\frac{2}{5}2\pi$	$\frac{1}{5}2\pi$
5	$10\pi\,(i-1)\,126/5$	0	0	0	0	0

Recalling that $f = kf_g^p + qf_C$, the presence of the component at the frequency f in the spectrum $X^r(f)$ is evaluated by adding the phase of the corresponding terms (i) and (ii). For example, for the component at the gear mesh frequency $f = f_g^p$ (i.e. $k = 1;\ q = 0$), the phase of the N components in the range $[0, 2\pi)$ are $\left\{0 + 0;\ \frac{1}{5}2\pi + 0;\ \frac{2}{5}2\pi + 0;\ \frac{3}{5}2\pi + 0;\ \frac{4}{5}2\pi + 0\right\} = \left\{0;\ \frac{1}{5}2\pi;\ \frac{2}{5}2\pi;\ \frac{3}{5}2\pi;\ \frac{4}{5}2\pi\right\}$, which indicates that the N components are equally distributed in $[0, 2\pi)$. This means that they add destructively, so that the component at $f = f_g^p$ has amplitude zero in the spectrum $X^r(f)$.

Let us now evaluate the component at the frequency $f = f_g^p - f_C$ (i.e. $k = 1;\ q = -1$). In this case the phase of the N components in the range $[0, 2\pi)$ are
$\left\{0 + 0;\ \frac{1}{5}2\pi + \frac{4}{5}2\pi;\ \frac{2}{5}2\pi + \frac{3}{5}2\pi;\ \frac{3}{5}2\pi + \frac{2}{5}2\pi;\ \frac{4}{5}2\pi + \frac{1}{5}2\pi\right\} = \{0;\ 0;\ 0;\ 0;\ 0\}$. Since all components are in-phase they add constructively, so that the component at $f = f_g^p - f_C$ is present in the spectrum with a magnitude of $Na_q^r v_k^r$. From the values given in tables 2.1 and 2.2, the following combinations of $(k; q)$ give a constructive sum as a result: $(1; -1)$, $(1; 4)$, $(2; -2)$,

Table 2.2: Phase of the term (ii) of eq. (2.18) for the N components.

q	Phase expression	Phase in the range $[0, 2\pi)$				
		$i=1$	$i=2$	$i=3$	$i=4$	$i=5$
-5	$-2\pi\,(i-1)$	0	0	0	0	0
-4	$-8\pi\,(i-1)\,/5$	0	$\frac{1}{5}2\pi$	$\frac{2}{5}2\pi$	$\frac{3}{5}2\pi$	$\frac{4}{5}2\pi$
-3	$-6\pi\,(i-1)\,/5$	0	$\frac{2}{5}2\pi$	$\frac{4}{5}2\pi$	$\frac{1}{5}2\pi$	$\frac{3}{5}2\pi$
-2	$-4\pi\,(i-1)\,/5$	0	$\frac{3}{5}2\pi$	$\frac{1}{5}2\pi$	$\frac{4}{5}2\pi$	$\frac{2}{5}2\pi$
-1	$-2\pi\,(i-1)\,/5$	0	$\frac{4}{5}2\pi$	$\frac{3}{5}2\pi$	$\frac{2}{5}2\pi$	$\frac{1}{5}2\pi$
0	0	0	0	0	0	0
1	$2\pi\,(i-1)\,/5$	0	$\frac{1}{5}2\pi$	$\frac{2}{5}2\pi$	$\frac{3}{5}2\pi$	$\frac{4}{5}2\pi$
2	$4\pi\,(i-1)\,/5$	0	$\frac{2}{5}2\pi$	$\frac{4}{5}2\pi$	$\frac{1}{5}2\pi$	$\frac{3}{5}2\pi$
3	$6\pi\,(i-1)\,/5$	0	$\frac{3}{5}2\pi$	$\frac{1}{5}2\pi$	$\frac{4}{5}2\pi$	$\frac{2}{5}2\pi$
4	$8\pi\,(i-1)\,/5$	0	$\frac{4}{5}2\pi$	$\frac{3}{5}2\pi$	$\frac{2}{5}2\pi$	$\frac{1}{5}2\pi$
5	$2\pi\,(i-1)$	0	0	0	0	0

$(2;3)$, $(3;-3)$, $(3;2)$, $(4;-4)$, $(4;1)$, $(5;-5)$, $(5;0)$ and $(5;5)$. The spectrum of the vibrations measured by the sensor $X^r(f)$ for this example is illustrated in figure 2.9. The magnitude of each of these components in the spectrum can be calculated provided the Fourier coefficients a_q^r and v_k^r are known. For example, for the component at $f/f_C = 125$ (i.e. $k=1$ and $q=-1$) the Fourier coefficients are $a^r_{-1} = 0.1241$ and $v_1^r = 1$. Since $N=5$, the magnitude of this component is given by $0.1241 \times 1 \times 5 = 0.6205$, as shown in fig. 2.9. In this figure, it can also be noted that the structure is not the same around all harmonics of f_g^p. It is also observed that for $k=1$ to 4 there is no component at $f = kf_g^p$, but this is present at $f = 5 \times f_g^p$. Moreover, the sideband structure around this frequency is symmetric in amplitude and frequency, as observed in the zoom box at the top right of the figure.

Group (C): *PG with unequally spaced planet gears and in-phase gear meshes*

PG of this group have planet gears that are not equally distributed around the sun gear, which means that $\psi_i \neq \frac{2\pi(i-1)}{N}$. However, the planet gears are assembled at angular positions satisfying the in-phase restriction $\gamma_{ri} = \frac{Z_R\psi_i}{2\pi} \in \mathbb{N}_0$.

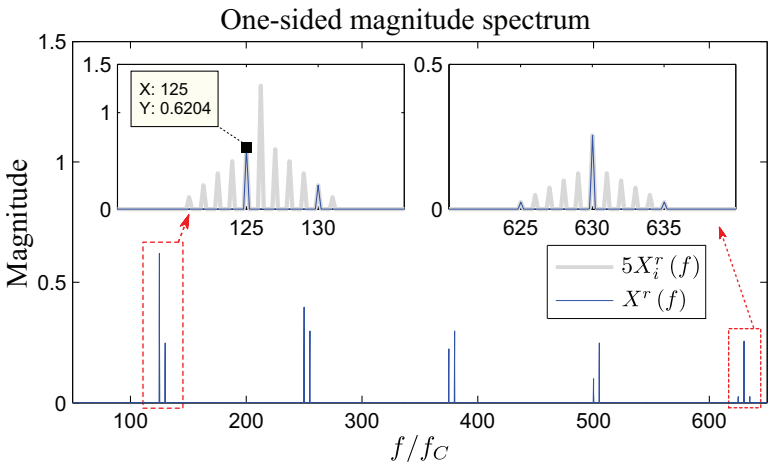

Figure 2.9: Illustration of the spectral structure of a PG of group (B) ($Z_R = 126$ and $N = 5$).

Let us evaluate the second exponential term of eq. (2.11), which can be expressed as:

$$e^{-j(kZ_R+q)\psi_i} = \underbrace{e^{-jk2\pi\gamma_{ri}}}_{(i)}\underbrace{e^{-jq\psi_i}}_{(ii)} \tag{2.19}$$

In this equation, it is clear that the phase of term (i) is either 0 or an integer multiple of 2π. Hence, the phase difference of the N spectral components is determined only by the term (ii). If for a given $f = kf_g^p + qf_C$, the phases $q\psi_i|_{i=1\ldots N}$ are all zero in the range $[0, 2\pi)$ –as it is the case for the components at the gear mesh frequency and harmonics, for which $q = 0$–, the component will be present in the spectrum $X^r(f)$ with an amplitude given by $Na_q^r v_k^r$. Otherwise, its presence in the spectrum is dependent on the phase distribution of the phases $q\psi_i|_{i=1\ldots N}$ in the range $[0, 2\pi)$, and its amplitude is given by $a_q^r v_k^r$ weighted by the magnitude of the resultant of the vectorial sum of the N components. Based on this, the following observations can be listed for the spectral structure of PG of this group:

1. The component at f_g^p and harmonics (i.e. $q = 0$) is always present in the spectrum. Compared with their respective sidebands, they have the largest amplitude;

2. Since for spectral components with equal magnitude of q only the sign of the phase of term (ii) differs, these components have the same amplitude, so that the structure of sidebands around kf_g^p is symmetric;

3. The structure of the sidebands and the relative amplitude between the central component and the amplitude of its sidebands is the same for all harmonics of f_g^p.

All this can be illustrated through an example. Consider a PG with $Z_R = 126$ and three planet gears positioned at 0°, 120° and 220°, which corresponds to the example (*iii*)-*a* of [IK09]. Table 2.3 shows the phase in the range $[0, 2\pi)$ of the term (*ii*) for the N spectral components and the resultant of the vectorial sum.

Table 2.3: Phase of the term (*ii*) for the N components.

q	Phase expression	Phase in the range $[0, 2\pi)$			Resultant	
		$i = 1$	$i = 2$	$i = 3$	Magnitude	Phase
-5	$5\psi_i$	0	$\frac{2}{3}2\pi$	$\frac{1}{18}2\pi$	1.532	340.00°
-4	$4\psi_i$	0	$\frac{1}{3}2\pi$	$\frac{4}{9}2\pi$	1.286	110.00°
-3	$3\psi_i$	0	0	$\frac{5}{6}2\pi$	2.646	340.89°
-2	$2\psi_i$	0	$\frac{2}{3}2\pi$	$\frac{2}{9}2\pi$	0.684	10.00°
-1	ψ_i	0	$\frac{1}{3}2\pi$	$\frac{11}{18}2\pi$	0.347	140.00°
0	0	0	0	0	3.000	0.00°
1	$-\psi_i$	0	$\frac{2}{3}2\pi$	$\frac{7}{18}2\pi$	0.347	220.00°
2	$-2\psi_i$	0	$\frac{1}{3}2\pi$	$\frac{7}{9}2\pi$	0.684	350.00°
3	$-3\psi_i$	0	0	$\frac{1}{6}2\pi$	2.646	19.11°
4	$-4\psi_i$	0	$\frac{2}{3}2\pi$	$\frac{5}{9}2\pi$	1.286	250.00°
5	$-5\psi_i$	0	$\frac{1}{3}2\pi$	$\frac{17}{18}2\pi$	1.532	20.00°

The magnitude of the spectral component at $f = kf_g^p + qf_C$ can be calculated by multiplying $a_q^r v_k^r$ by the corresponding magnitude of the resultant. Note that only for $f = kf_g^p$ all N components are in phase, so that they add constructively to give the highest weighting function of 3. Figure 2.10 illustrates the spectrum $X^r(f)$ (thin line) and the N-scaled version of the vibrations coming from a single planet $X_i^r(f)$ (thick gray line) for this example, where the agreement with the observations 1, 2 and 3 is clearly observed.

For clarity purposes, the spectral magnitude of two components of the spectrum of fig. 2.10 are exemplarly calculated. First the component at the gear mesh frequency $f/f_C = 126$ is considered. For this frequency the Fourier coefficients are $a_0^r = 0.2554$ and $v_1^r = 1$; and the magnitude of the resultant is equal to 3 (from table 2.3). Thus, the magnitude of the component in the spectrum is given by $0.2554 \times 1 \times 3 = 0.7662$, as shown in fig. 2.10. Next, the magnitude of the component at $f/f_C = 128$ is calculated. For this frequency, the Fourier coefficients are

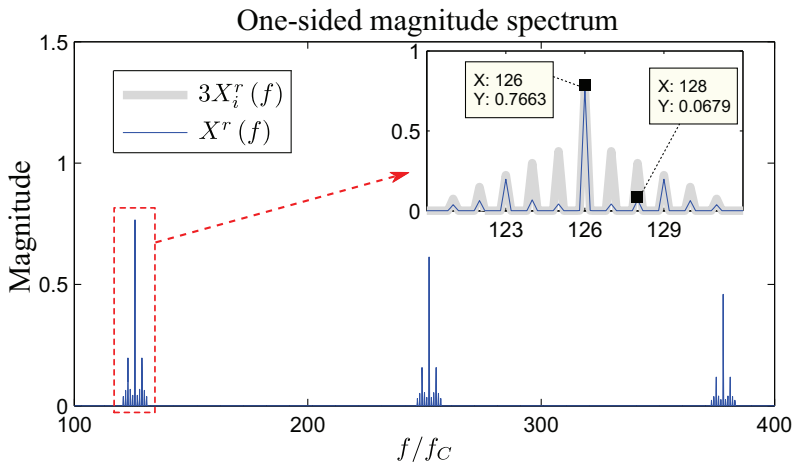

Figure 2.10: Illustration of the spectral structure of a PG of group (C) ($Z_R = 126$; $\psi_1 = 0°$, $\psi_2 = 120°$ and $\psi_3 = 220°$).

$a_0^r = 0.0993$ and $v_1^r = 1$; and the magnitude of the resultant is equal to 0.684 (from table 2.3). Hence, the magnitude of the component in the spectrum is given by $0.0993 \times 1 \times 0.684 = 0.0679$.

Group (D): *PG with unequally spaced planet gears and out-of–phase gear meshes*

For PG of this group $\psi_i \neq \frac{2\pi(i-1)}{N}$ and $\gamma_{ri} \notin \mathbb{N}_0$. Since there are several combinations that satisfy these restrictions, there is no specific spectral structure for PG of this group. However, it can be said that the most typical case corresponds to a structure with components present at f_g^p and harmonics, each with a rich family of amplitude asymmetric sidebands spaced apart by f_C.

In PG of this group, the second exponential term of eq. (2.11) cannot be conveniently separated as in the previous groups, so that the complete phase expressions $-j\,(kZ_R + q)\,\psi_i|_{i=1\ldots N}$ must be individually evaluated for each spectral component at $f = kf_g^p + qf_C$. Table 2.4 shows the result of the phase calculations for the spectral components around f_g^p for a PG with $Z_R = 126$ and four planet gears positioned at 0°, 97.2°, 174.6° and 282.6°, which corresponds to the example (iv)-c of [IK09]. Fig. 2.11 shows the spectrum with a zoom around f_g^p. The magnitude of each spectral component is equal to $a_q^r v_k^r$ multiplied by the corresponding amplitude of the resultant. In this example, for $f/f_C = 125$ the Fourier coefficients are $a_q^r = 0.1241$ and $v_k = 1$; and the magnitude of the resultant is, from table 2.4, equal to 1.414. Hence, the magnitude of the spectral component is equal to $0.1241 \times 1 \times 1.414 = 0.1755$, as shown in the fig. 2.11. Note also that the sideband structure around f_g^p differs from the sideband structure around its

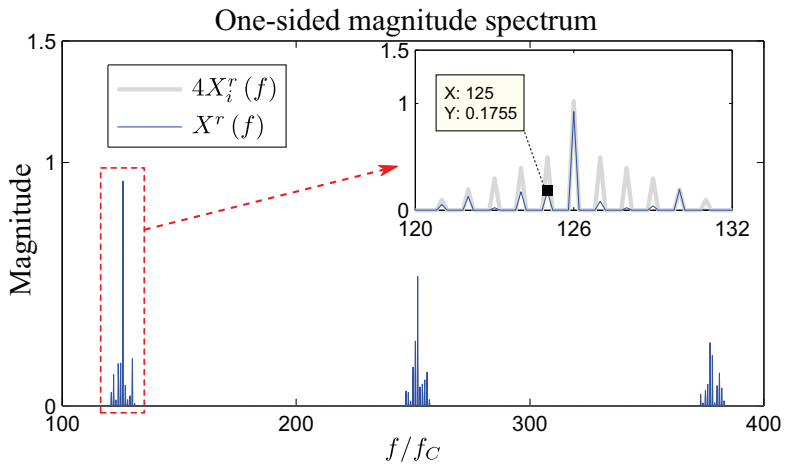

Figure 2.11: Illustration of the spectral structure of a PG of group (D) ($Z_R = 126$; $\psi_1 = 0°$, 97.2°, 174.6° and 282.6°).

harmonics. This is explained by the influence of the term $kZ_r\psi_i$ in the phase expression of each component.

Table 2.4: Phase for the N components around $f = f_g^p$.

q	Phase expression	Phase in the range $[0, 2\pi)$				Resultant	
		$i=1$	$i=2$	$i=3$	$i=4$	Magnitude	Phase
-5	$(121)\,\psi_i$	0	$\frac{67}{100}2\pi$	$\frac{137}{200}2\pi$	$\frac{197}{200}2\pi$	2.194	300.60°
-4	$(122)\,\psi_i$	0	$\frac{47}{50}2\pi$	$\frac{17}{100}2\pi$	$\frac{77}{100}2\pi$	2.583	349.20°
-3	$(123)\,\psi_i$	0	$\frac{23}{200}2\pi$	$\frac{131}{200}2\pi$	$\frac{111}{200}2\pi$	0.562	296.10°
-2	$(124)\,\psi_i$	0	$\frac{48}{100}2\pi$	$\frac{14}{100}2\pi$	$\frac{34}{100}2\pi$	1.744	86.40°
-1	$(125)\,\psi_i$	0	$\frac{75}{100}2\pi$	$\frac{125}{200}2\pi$	$\frac{25}{200}2\pi$	1.414	315.00°
0	$(126)\,\psi_i$	0	$\frac{1}{50}2\pi$	$\frac{11}{100}2\pi$	$\frac{91}{100}2\pi$	3.614	3.60°
1	$(127)\,\psi_i$	0	$\frac{29}{100}2\pi$	$\frac{119}{200}2\pi$	$\frac{139}{200}2\pi$	0.676	232.20°
2	$(128)\,\psi_i$	0	$\frac{14}{25}2\pi$	$\frac{2}{25}2\pi$	$\frac{12}{25}2\pi$	0.243	100.80°
3	$(129)\,\psi_i$	0	$\frac{83}{100}2\pi$	$\frac{113}{200}2\pi$	$\frac{53}{200}2\pi$	0.546	329.40°
4	$(130)\,\psi_i$	0	$\frac{1}{10}2\pi$	$\frac{1}{20}2\pi$	$\frac{1}{20}2\pi$	3.902	18.00°
5	$(131)\,\psi_i$	0	$\frac{37}{100}2\pi$	$\frac{107}{200}2\pi$	$\frac{167}{200}2\pi$	0.381	246.60°

Summary

It has been shown in this section that the vibrations measured by a sensor installed on the outer part of the ring gear of a PG can have very different spectral structures depending on its geometric characteristics. However, it must be remarked that all spectral structures, though different, represent the normal behaviour of the corresponding PG. This is in opposition to fixed-shaft gearboxes, where the spectral structures are roughly the same.

It is also important to recall the assumptions done for the presented analysis (see section 2.2.1), in brief:

(i) vibrations are only generated in the planet-ring meshing processes,

(ii) the vibrations generated in each planet-ring meshing are periodic, have the same amplitude and have no amplitude modulation,

(iii) the vibrations are transmitted to the sensor through the ring gear only.

For instance, if assumption (ii) is not satisfied, then the structure of the spectrum $X^r(f)$ will be affected. This is illustrated in fig. 2.12, which shows the spectrum of the same PG used as example for the group (A) (see fig. 2.8), but where the vibrations generated in each of the planet-ring meshes are taken as sinusoidals with amplitude 1; 0.80 and 0.55 for the three planet-ring meshes respectively. Note the decrease in the amplitude of the existing components and the appearance of new sidebands around f_g^p spaced at f_C.

On the other hand, assumption (i) means that the vibrations generated in the meshing of the sun with the planet gears are not taken into account. This is something that, to the knowledge of the author, has been missed in all published works regarding vibrations in PG. Likewise, transmission paths from the generation point of the vibrations to the sensor other than directly through the ring gear, have been disregarded (assumption (iii)). The following sections deals with the relaxation of these assumptions.

2.2.4. Vibrations generated in the sun-planet gear meshes

The model presented in section 2.2.1 considered only the vibrations generated in the planet-ring gear meshes $v_i^r(t)\,|_{i=1,\dots,N}$. In this section, the vibrations generated in the sun-planet gear

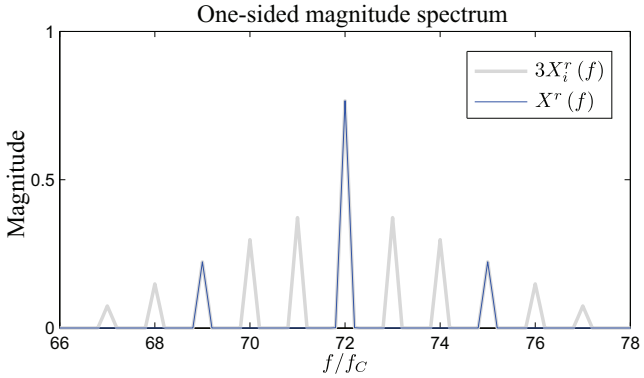

(a)

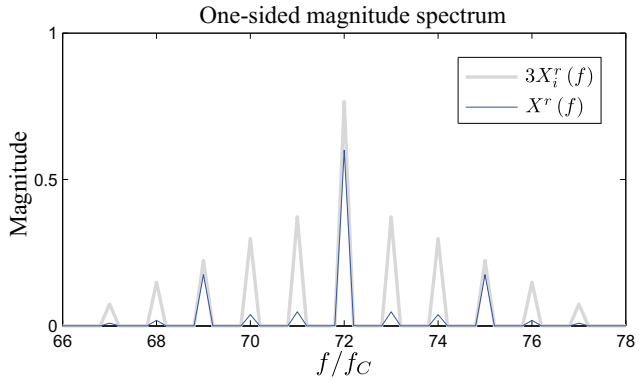

(b)

Figure 2.12: Illustration of the effect of the amplitudes of $v_i^r(t)$ for the PG used as example for the group (A). (a) The amplitudes of $v_1^r(t)$, $v_2^r(t)$ and $v_3^r(t)$ are equal to 1.00. (b) The amplitudes of $v_1^r(t)$, $v_2^r(t)$ and $v_3^r(t)$ are equal to 1.00; 0.80 and 0.55 respectively.

meshes $v_i^s(t)|_{i=1,\dots,N}$ are included and its influence in the spectrum of the vibrations measured by the sensor on the outer part of the ring gear is analysed. For this, following considerations are taken:

(i) vibrations are generated in the planet-ring and in the sun-planet meshes: $v_i^r(t)|_{i=1,\dots,N}$ and $v_i^s(t)|_{i=1,\dots,N}$, as experienced by an observer in the carrier plate;

(ii) the vibrations $v_i^r(t)|_{i=1,\dots,N}$ are periodic and have no amplitude modulation. The Fourier coefficients of $v_1^r(t)$ are represented by v_k^r;

(iii) the vibrations $v_i^s(t)|_{i=1,\dots,N}$ are periodic and have no amplitude modulation. The Fourier coefficients of $v_1^s(t)$ are represented by v_k^s;

(iv) all vibrations are transmitted to the sensor directly through the ring gear only.

It is important to note that $v_i^s(t)$ is generated in the points of contact between the meshing teeth of the sun gear and the i-th planet gear. Thus, consideration (iv) means that the vibrations $v_i^s(t)|_{i=1,\dots,N}$ are transmitted to the sensor through the sun-planet and planet-ring meshing teeth, including the lubricant films inbetween. To account for this, and since this is not the case for the vibrations $v_i^r(t)|_{i=1,\dots,N}$, two different amplitude modulation functions $a_i^r(t)|_{i=1,\dots,N}$ and $a_i^s(t)|_{i=1,\dots,N}$ due to the carrier rotation are used for the vibrations $v_i^r(t)|_{i=1,\dots,N}$ and $v_i^s(t)|_{i=1,\dots,N}$, respectively. All amplitude modulation functions, however, are periodic with the same fundamental period $T_C = 1/f_C$, and are in-phase. More accurate results would be obtained if the shape of both amplitude modulation functions were known. These functions should be specific for each PG and its knowledge would require a highly complex analysis that is out of the scope of this work. In this work both functions $a_i^r(t)$ and $a_i^s(t)$ are taken as bell-shaped functions, being the amplitude of $a_i^s(t)$ lower than the amplitude of $a_i^r(t)$, to account for the attenuation of the vibrations generated in the meshing of the sun with the planet gear $v_i^s(t)$, due to the longer transmission path to the sensor.

As it has been shown, the relative phases between all generated vibrations play a crucial role in the frequency structure of the vibrations measured by the sensor. Therefore, the phase difference between the vibrations $v_i^s(t)|_{i=1,\dots,N}$ is first analysed. Using the angular pitch of the sun gear $\angle_S = 2\pi/Z_S$, the phase difference γ_{si} between the vibration generated in the meshing of the sun with the i-th planet gear $v_i^s(t)$ and the vibration generated in the meshing of the sun with the first planet gear $v_1^s(t)$ can be expressed as:

$$\gamma_{si} = \frac{\psi_i}{\angle_S} = \frac{\psi_i Z_S}{2\pi} \tag{2.20}$$

Since by definition only the non-integer part of the phase differences is retained, it has been demonstrated that $\gamma_{ri} = \gamma_{si}$ [PL04].

It is also important to consider the phase difference γ_{sr}^i between the vibration generated in the meshing of the sun gear with the i-th planet gear $v_i^s(t)$, and the vibration generated in the meshing of the i-th planet gear and the ring gear $v_i^r(t)$. It can be shown that this phase difference is the same for all planets (i.e. $\gamma_{sr}^i = \gamma_{sr}$), and that its magnitude is dependent on the geometry of the gear wheels (base radii, outer radii, pressure angle, planet tooth tickness, etc.). However, if the PG pertains to the group (A) and Z_P is even, then $\gamma_{sr} = 0$ and all vibrations

$v_i^s(t)|_{i=1,\dots,N}$ and $v_i^r(t)|_{i=1,\dots,N}$ are in-phase; Differently, if Z_P is odd, then $\gamma_{sr} = 1/2$. In all other cases γ_{sr} has a constant value other than zero, which can be determined provided the geometry of the gear wheels is known [PL04].

Considering the phase of the meshing of the first planet gear with the ring gear as the reference (i.e. $\gamma_{r1} = 0$), the vibrations generated in the meshing process of the i-th planet gear as experienced by an observer in the carrier plate can be expressed as follows:

$$v_i^r(t) = v_1^r\left(t - \gamma_{ri} T_g^p\right) \tag{2.21a}$$

$$v_i^s(t) = v_1^s\left(t - (\gamma_{ri} + \gamma_{sr}) T_g^p\right) \tag{2.21b}$$

where $v_1^r(t)$ and $v_1^s(t)$ are in-phase by definition.

Since all vibrations are transmitted through the ring gear, the amplitude modulation functions of the vibrations generated on the i-th planet gear $a_i^r(t)$ and $a_i^s(t)$ are related to the amplitude modulation functions of the vibrations generated on the first planet gear $a_1^r(t)$ and $a_1^s(t)$ as follows:

$$a_i^r(t) = a_1^r\left(t - \frac{\psi_i T_C}{2\pi}\right) \tag{2.22a}$$

$$a_i^s(t) = a_1^s\left(t - \frac{\psi_i T_C}{2\pi}\right) \tag{2.22b}$$

Thus, the vibrations measured by the sensor can be written as:

$$\begin{aligned} x^{r,s}(t) &= x^r(t) + x^s(t) = \sum_{i=1}^{N} x_i^r(t) + \sum_{i=1}^{N} x_i^s(t) \\ &= \sum_{i=1}^{N} a_1^r\left(t - t_1 - \frac{\psi_i T_C}{2\pi}\right) v_1^r\left(t - \gamma_{ri} T_g^p\right) + \sum_{i=1}^{N} a_1^s\left(t - t_1 - \frac{\psi_i T_C}{2\pi}\right) v_1^s\left(t - (\gamma_{ri} + \gamma_{sr}) T_g^p\right) \end{aligned} \tag{2.23}$$

where the time shift $t_1 = \frac{\theta_1}{2\pi f_C}$ accounts for the unknown position of the planets at the measurement start.

For the frequency analysis, the Fourier transform of eq. (2.23) is calculated:

$$\begin{aligned} X^{r,s}(f) &= X^{r}(f) + X^{s}(f) = \sum_{i=1}^{N} X_i^r(f) + \sum_{i=1}^{N} X_i^s(f) \\ &= \sum_{k\in\mathbb{Z}} \sum_{q\in\mathbb{Z}} \sum_{i=1}^{N} \left[a_q^r v_k^r + a_q^s v_k^s e^{-j2\pi k\gamma_{sr}}\right] e^{-j2\pi q f_C t_1} e^{-j(kZ_R+q)\psi_i} \delta\left(f - k f_g^p - q f_C\right) \end{aligned} \tag{2.24}$$

It can be observed in eq. (2.24) that for a given frequency f, $X_i^s(f)$ affects the amplitude and the absolute phase of $X^{r,s}(f)$ through the terms $a_q^s v_k^s$ and $e^{-j2\pi k\gamma_{sr}}$, but not the relative distribution in the range $[0, 2\pi)$ of the N components at this frequency, which is determined only by the term $e^{-j(kZ_R+q)\psi_i}$. This means that the components present in the spectrum $X^{r,s}(f)$ are the same as in the spectrum $X^r(f)$; only the amplitudes are different. This is illustrated in fig. 2.13. Fig. 2.13a shows the spectrum $X^r(f)$ of the PG used as an example for the group A, considering only the vibrations generated in the planet-ring gear meshings $v_i^r(t)|_{i=1,\ldots,N}$; fig. 2.13b shows the spectrum $X^{r,s}(f)$ of the same PG considering also the vibrations generated in the sun-planet gear meshings $v_i^s(t)|_{i=1,\ldots,N}$, which were taken as $v_i^s(t) = 1.2 \times v_i^r(t)|_{i=1,\ldots,N}$. The fact that the factor chosen (1.2) is greater than one accounts for the expected higher vibrations generated in the external meshing compared with the vibrations generated in the internal meshing, as explained in section 1.4.1.2. In this example $Z_P = 26$ is even, so that $\gamma_{sr} = 0$ and the term $e^{-j2\pi k\gamma_{sr}}$ of eq. (2.24) equals one, wich means that all spectral components of $X_i^r(f)|_{i=1,\ldots,N}$ and $X_i^s(f)|_{i=1,\ldots,N}$ are in-phase. For the amplitude modulation functions, the following relation was used: $a_i^s(t)|_{i=1,\ldots,N} = 0.65 \times a_i^r(t)|_{i=1,\ldots,N}$. The factor $0.65 < 1$ accounts for the attenuation due to the longer transmission path to the sensor. Therefore, for this example, the relation between both spectra is given by:

$$X^{r,s}(f) = |1 + 1.2 \times 0.65| \times X^r(f) = 1.78 \times X^r(f) \tag{2.25}$$

which is illustrated in fig. 2.13b

As a second example, a PG with $Z_S = 27$, $Z_P = 31$, $Z_R = 90$ and $\psi_i = \left\{0, \frac{2\pi}{3}, \frac{4\pi}{3}\right\}$ is considered. This PG also pertains to the group A. The spectra $X^r(f)$ and $X^{r,s}(f)$ are illustrated in fig. 2.14a and 2.14b. Differently, here Z_P is odd, so that $\gamma_{sr} = 1/2$ and the term $e^{-j2\pi k\gamma_{sr}}$ from eq.

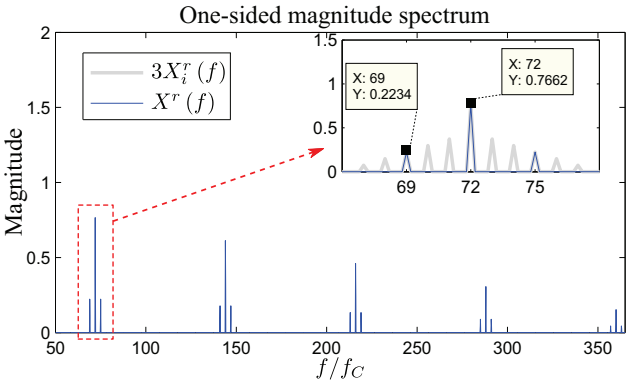

(a)

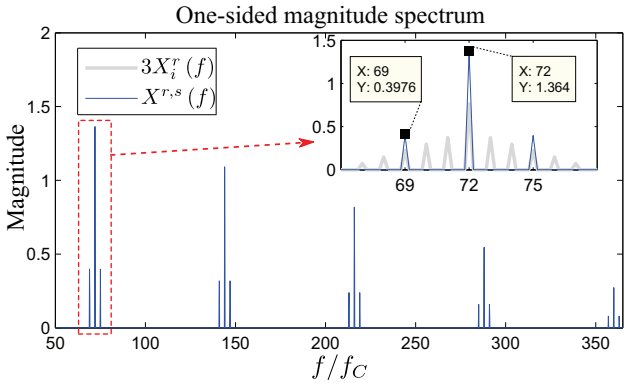

(b)

Figure 2.13: Illustration of the effect of the vibrations generated in the sun-planet gear meshes $x^s(t)$ in the spectrum for the PG used as example for the group A ($Z_S = 18$, $Z_P = 26$, $Z_R = 72$ and $\psi_i = \{0, \frac{2\pi}{3}, \frac{4\pi}{3}\}$. (a) Considering only the vibrations from the planet-ring meshes $x^r(t)$. (b) Considering the vibrations from the planet-ring meshes $x^r(t)$ and the vibrations from the sun-planet meshes $x^s(t)$.

(2.24) takes the values:

$$e^{-j2\pi k\gamma_{sr}} = \begin{cases} 1 & \text{, if } k \text{ is even} \\ e^{-j\pi} & \text{, if } k \text{ is odd} \end{cases} \tag{2.26}$$

where the phase was constrained to the range $[0, 2\pi)$. This means that the spectral components of the vibrations $X_i^r(f)|_{i=1,\dots,N}$ and $X_i^s(f)|_{i=1,\dots,N}$ are all in-phase for even values of k, so that all components add constructively. However, if k is odd, then the spectral components of $X_i^r(f)|_{i=1,\dots,N}$ and $X_i^s(f)|_{i=1,\dots,N}$ have opposite phase, so that the components of $X_i^r(f)|_{i=1,\dots,N}$ add destructively with the components of $X_i^s(f)|_{i=1,\dots,N}$. Mathematically, the relation between

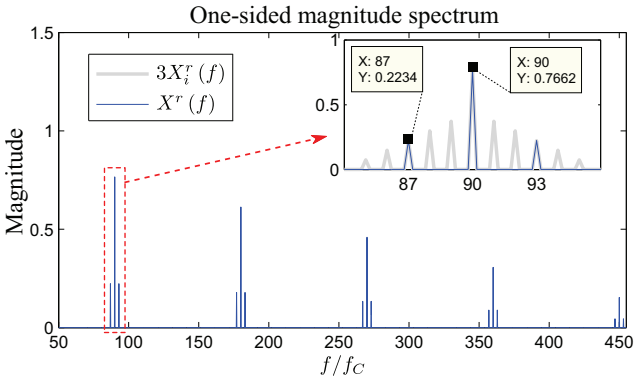

(a)

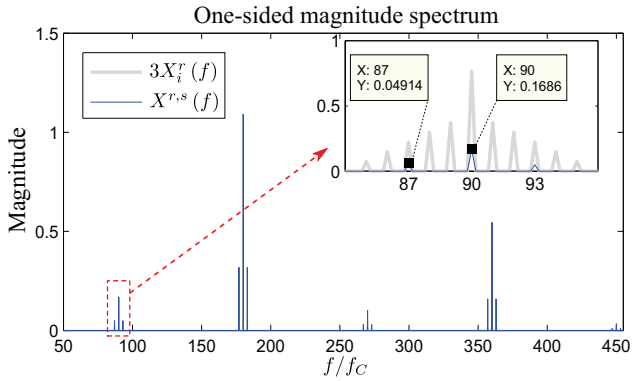

(b)

Figure 2.14: Illustration of the effect of the vibrations generated in the sun-planet gear meshes $x^s(t)$ in the spectrum for a PG of group A with $Z_S = 27$, $Z_P = 31$, $Z_R = 90$ and $\psi_i = \{0, \frac{2\pi}{3}, \frac{4\pi}{3}\}$. (a) Considering only the vibrations from the planet-ring meshes $x^r(t)$. (b) Considering the vibrations from the planet-ring meshes $x^r(t)$ and the vibrations from the sun-planet meshes $x^s(t)$.

both spectra can be written as:

$$X^{r,s}(f) = \begin{cases} |1 + 1.2 \times 0.65| \times X^r(f) = 1.78 \times X^r(f) & \text{, if } k \text{ is even} \\ |1 - 1.2 \times 0.65| \times X^r(f) = 0.22 \times X^r(f) & \text{, if } k \text{ is odd} \end{cases} \tag{2.27}$$

which is shown in fig. 2.14b.

Other cases with γ_{sr} other than zero or 1/2 would affect the amplitudes of the spectrum differently. Since the value of γ_{sr} depends on geometrical values that are not available at this point, the evaluation for other cases is not presented in this work. However, this can be easily done by following the procedure presented here, provided γ_{sr} is known.

2.2.5. Transmission of vibrations through the sun gear and carrier plate

Till this point, the transmission of the vibrations generated in the planet-ring gear meshes and sun-planet gear meshes have been considered to be transmitted to the sensor only directly through the ring gear. However, these vibrations can also be transmitted through the sun gear and through the carrier plate to the case of the PG, and from there to the sensor. This is illustrated in fig. 2.15, where the following notation is used:

TP_R^r: Direct transmission path of the vibrations generated in the planet-ring gear meshes through the ring gear,

TP_R^s: Direct transmission path of the vibrations generated in the sun-planet gear meshes through the ring gear,

TP_{SC}^r: Transmission path of the vibrations generated in the planet-ring gear meshes through the sun gear and carrier plate, and

TP_{SC}^s: Transmission path of the vibrations generated in the sun-planet gear meshes through the sun gear and carrier plate.

In the development of the vibration model in section 2.2.2, it was shown that due to the relative movement of the planet gears with respect to the sensor, the transmission path TP_R^r acts as an amplitude modulation function of the vibrations generated in the meshing of the planet gears with the ring gear $v_i^r(t)|_{i=1,\dots,N}$. Similarly, in section 2.2.4 it was shown that the vibrations generated in the meshing of the sun gear with the planet gears $v_i^s(t)|_{i=1,\dots,N}$ are amplitude modulated due to the variable transmission path TP_R^s.

Differently, the transmission paths TP_{SC}^r and TP_{SC}^s are not affected by the relative movement of the planets with respect to the sensor (see fig. 2.15). Hence, TP_{SC}^r and TP_{SC}^s remain constant during the functioning of the PG. An accurate representation of the shape and magnitude of TP_{SC}^r and TP_{SC}^s is, like in the case of the other transmission paths, outside the scope of this work. They are considered here as a constant function that attenuates the corresponding vibrations. The time delay of the vibrations generated in the planet-ring gear meshes due to the difference in length of the transmission paths TP_R^r and TP_{SC}^r; and of the vibrations generated

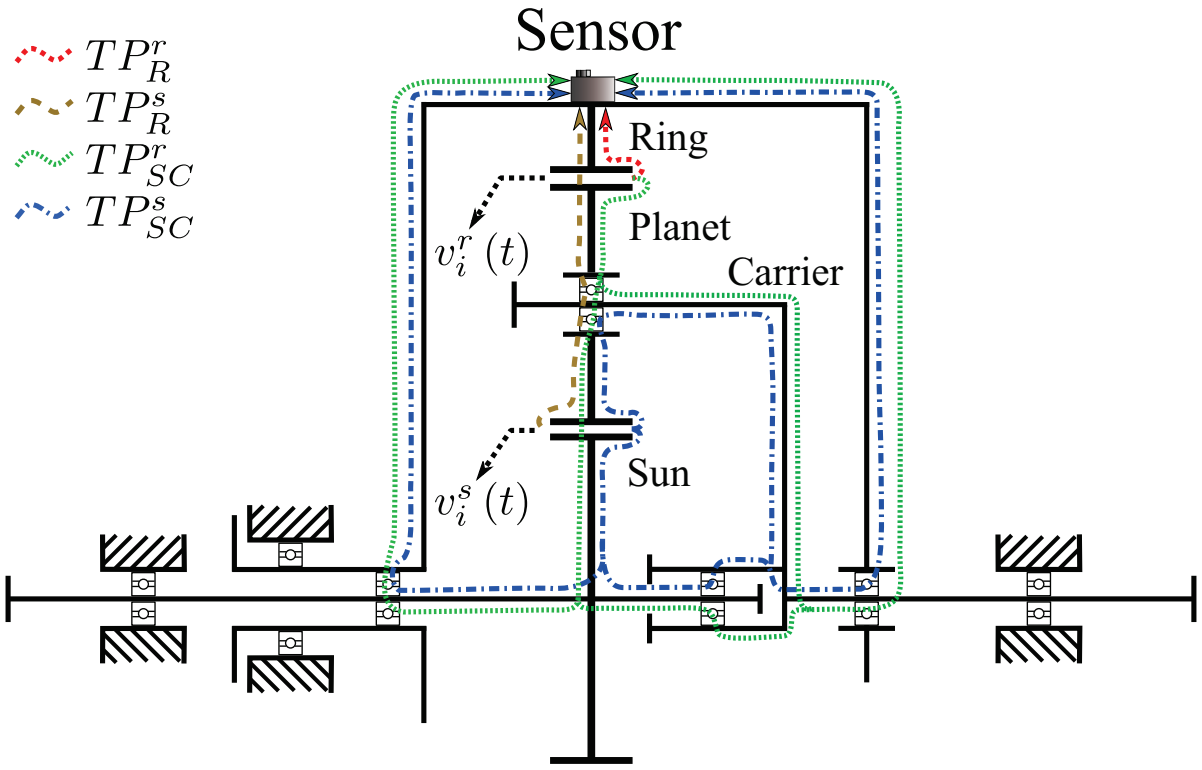

Figure 2.15: The vibrations generated in the planet-ring and sun-planet gear meshes are also transmitted to the sensor through the sun gear and carrier plate.

in the sun-planet gear meshes due to the difference in length of TP_R^s and TP_{SC}^s are considered to be small enough to be neglected.

The vibrations transmitted through TP_R^s and TP_{SC}^s will produce spectral components at the gear mesh frequency f_g^p and harmonics, whose amplitude depends on the degree of attenuation of $v_i^r(t)|_{i=1,\dots,N}$ and $v_i^s(t)|_{i=1,\dots,N}$. The vibration measured by the sensor can thus be expressed as:

$$x(t) = v^r(t)|_{TP_R^r} + v^s(t)|_{TP_R^s} + v^r(t)|_{TP_{SC}^r} + v^s(t)|_{TP_{SC}^s} \tag{2.28}$$

where:

$v^r(t)|_{TP_R^r}$ represents the vibrations generated in the planet-ring gear meshes that are transmitted to the sensor directly to the ring gear (i.e. $v^r(t)|_{TP_R^r} = x^r(t) = \sum_{i=1}^{N} x_i^r(t)$);

$v^s(t)|_{TP_R^s}$ represents the vibrations generated in the sun-planet gear meshes that are transmitted to the sensor directly to the ring gear (i.e. $v^s(t)|_{TP_R^s} = x^s(t) = \sum_{i=1}^{N} x_i^s(t)$);

$v^r(t)|_{TP^r_{SC}}$ represents the vibrations generated in the planet-ring gear meshes that are transmitted through the sun gear and carrier plate; and

$v^s(t)|_{TP^s_{SC}}$ represents the vibrations generated in the sun-planet gear meshes that are transmitted through the sun gear and carrier plate.

The transmission paths through the sun gear and carrier plate are taken as a constant value: $TP^r_{SC} = A^r_{SC} \in [0,1]$ and $TP^s_{SC} = A^s_{SC} \in [0,1]$, where the extreme values of the range mean total attenuation and zero attenuation respectively. After substitution, eq. (2.28) becomes:

$$x(t) = \sum_{i=1}^{N} x^r_i(t) + \sum_{i=1}^{N} x^s_i(t) + A^r_{SC} \sum_{i=1}^{N} v^r_i(t) + A^s_{SC} \sum_{i=1}^{N} v^s_i(t) \tag{2.29}$$

where

$$x^r_i(t) = a^r_1\left(t - t_1 - \frac{\psi_i T_C}{2\pi}\right) v^r_i(t) \tag{2.30a}$$

$$x^s_i(t) = a^s_1\left(t - t_1 - \frac{\psi_i T_C}{2\pi}\right) v^s_i(t) \tag{2.30b}$$

$$v^r_i(t) = v^r_1\left(t - \gamma_{ri} T^p_g\right) \tag{2.30c}$$

$$v^s_i(t) = v^s_1\left(t - (\gamma_{ri} + \gamma_{sr}) T^p_g\right) \tag{2.30d}$$

as defined in the previous sections.

For the frequency analysis, the Fourier transform of eq. (2.29) is calculated. The result of this is given in eq. (2.31).

$$X(f) = X^r(f) + X^s(f) + \mathcal{F}\left\{A^r_{SC} \sum_{i=1}^{N} v^r_1\left(t - \gamma_{ri} T^p_g\right)\right\} + \mathcal{F}\left\{A^s_{SC} \sum_{i=1}^{N} v^s_1\left(t - (\gamma_{ri} + \gamma_{sr}) T^p_g\right)\right\} \tag{2.31}$$

where the sum of the first two terms $X^r(f) + X^s(f) = X^{r,s}(f)$ is given in eq. (2.24), and the third and fourth terms are given by the following expressions:

$$\mathcal{F}\left\{A^r_{SC}\sum_i^N v_1^r\left(t-\gamma_{ri}T_g^p\right)\right\} = A^r_{SC}\sum_{k\in\mathbb{Z}}\sum_{i=1}^N v_k^r e^{-jkZ_R\psi_i}\delta\left(f-kf_g^p\right) \tag{2.32}$$

$$\mathcal{F}\left\{A^s_{SC}\sum_i^N v_1^s\left(t-\left(\gamma_{ri}+\gamma_{sr}\right)T_g^p\right)\right\} = A^s_{SC}\sum_{k\in\mathbb{Z}}\sum_{i=1}^N v_k^s e^{-jkZ_R\psi_i}e^{-j2\pi k\gamma_{sr}}\delta\left(f-kf_g^p\right) \tag{2.33}$$

It is noted from eqs. (2.32) and (2.33) that the vibrations transmitted through the sun gear and carrier plate influence only the components at the gear mesh frequency f_g^p and harmonics of the spectrum of the vibrations measured by the sensor. The magnitude of all other components are only a result of the vibrations transmitted directly through the ring gear.

Finally, substituting eqs. (2.24), (2.32) and (2.33) into eq. (2.31) and rearranging, eq. (2.31) becomes:

$$X(f) = \begin{cases} \sum_k\sum_q\sum_{i=1}^N\left[a_q^r v_k^r + a_q^s v_k^s e^{-j2\pi k\gamma_{sr}}\right]e^{-j2\pi qf_C t_1}e^{-j(kZ_R+q)\psi_i}\delta\left(f-kf_g^p-qf_C\right) & \text{if } q\neq 0 \\ \sum_k\sum_{i=1}^N\left[\left(a_0^r+A^r_{SC}\right)v_k^r+\left(a_0^s+A^s_{SC}\right)v_k^s e^{-j2\pi k\gamma_{sr}}\right]e^{-jkZ_R\psi_i}\delta\left(f-kf_g^p\right) & \text{if } q=0 \end{cases} \tag{2.34}$$

where k, $q\in\mathbb{Z}$.

Fig. 2.16a illustrates the spectrum $X(f)$ of eq. (2.34) for a PG of group (A) with $Z_S=18$, $Z_P=26$, $Z_R=72$ and $\psi_i=\left\{0;\frac{2\pi}{3};\frac{4\pi}{3}\right\}$. In this example, the following Fourier coefficients and constants for the transmission path through the sun and carrier plate were used:

$k=1,2,3,4$ and 5;

$v_k^r=\{1;0.8;0.6;0.4$ and $0.2\}$;

$v_k^s=1.2\times v_k^r$;

$q=0,1,2,3,4,5$ and 6;

$a_q^r=\{0.2554;0.1241;0.0993;0.0745;0.0496$ and $0.0248\}$;

$a_q^s=0.65\times a_q^r$;

$A^r_{SC} = 0.1$; and

$A^s_{SC} = 0.15$

As an example, the magnitude of the spectral component at $f/f_C = 72$ (i.e. $k = 1$ and $q = 0$) is calculated using eq. (2.34). According to the Fourier coefficients and constants used for the transmision paths through the sun and carrier plate, this is given by:

$$\sum_{i=1}^{N} [(0.2554 + 0.1) \times 1 + (0.65 \times 0.2554 + 0.15) \times 1.2] = 2.204 \tag{2.35}$$

as shown in fig. 2.16a. For comparison, fig. 2.16b shows the spectrum of the same PG without considering the transmission of vibrations through the sun gear and carrier plate. It is noted how only the magnitude of the components at the gear mesh frequency and harmonics are influenced, but not the magnitude of the sidebands.

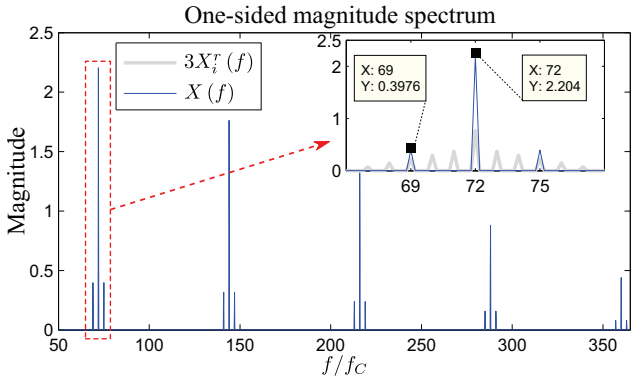

(a)

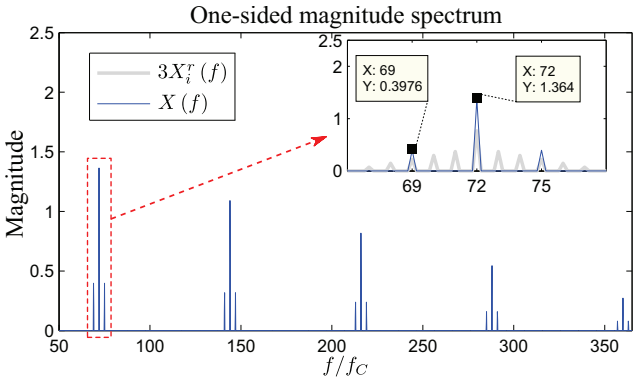

(b)

Figure 2.16: Illustration of the effect of the vibrations transmitted through the sun gear and carrier plate for the PG used as example for the group A ($Z_S = 18$, $Z_P = 26$, $Z_R = 72$ and $\psi_i = \{0, \frac{2\pi}{3}, \frac{4\pi}{3}\}$). (a) Considering the vibrations transmitted through the sun gear and carrier plate (TP^r_{SC} and TP^s_{SC}). (b) Considering only the vibrations transmitted directly through the ring gear (TP^r_R and TP^s_R).

2.2.6. Summary and comments

The keys to understand the vibrations generated in an epicyclic gearbox are the phase differences between the meshing processes present in the gearbox and the phase differences of the amplitude modulation functions, due to variations in the transmission paths. The former depends on geometrical characteristics of the gearbox, and are the same independent on the type of configuration of the EG; the latter depends on the measurement arrangement and/or on the configuration of the EG.

In this section, a phenomenological model has been developed for the vibrations measured on a PG with a sensor mounted on the outer part of the ring gear. The model considers all internal and external meshing processes present in the gearbox. It also takes the transmission paths

through the ring gear and through the sun gear and carrier plate into account.

The development of the model has been presented in a step-by-step procedure, so that it can be taken as a basis for the development of models for a star and solar gearbox. The same is valid for other sensor locations.

As it will be presented in chapters 3.3 and 3.4, the model shows good agreement with test bench and industrial measurements.

2.3. Acoustic emission model for planetary gearboxes

As presented in section 1.4.2, AE are generated during the meshing of the gears in epicyclic gearboxes. In this section, a model of the acoustic emissions generated in the meshing processes of epicyclic gearboxes is presented. Like in chapter 2.2, the case of a planetary gearbox with a sensor mounted in the outer part of the ring gear is considered. The model can be expanded to other configurations and measurement arrangements by taking the proper considerations. The objective of this section is, essentially, to present and describe the characteristics that differentiate the AE from the vibrations measured by the corresponding sensors.

2.3.1. Model development

It was observed in field and test bench measurements, that the AE generated in the gearing process constitute non-stationary signals, which experience some randomness in the amplitude and time of ocurrence of the bursts. This is illustrated in fig. 2.17, where portions of the AE signal corresponding to succesive revolutions of the carrier plate are plotted together. The extraction of each portion was possible thanks to the simultaneous measurement of a one-per-revolution pulse signal from the shaft of the carrier plate.

Due to the similarity of the observed signals, the model presented here is based on the model of the vibrations observed on faulty bearings developed in [RAC01].

For reasons of space, only the AE generated in the meshing between the planet gears and the ring gear transmitted to the sensor through the ring gear are consireded[4]. In this case, the AE generated in the meshing of the N planet gears with the ring gear as measured by the sensor $y^r(t)$ can be expressed as:

$$\begin{aligned} y^r(t) &= \sum_{i=1}^{N} y_i^r(t) \\ &= \sum_{i=1}^{N} \sum_{k} A_{k_{\left(t_1+\frac{\psi_i T_C}{2\pi}\right)}}^{i} s\left(t - kT_g^p - \tau_k^i - \gamma_{ri} T_g^p\right) + n(t) \end{aligned} \tag{2.36}$$

[4]The influence of the planet-sun meshing processes and the transmission through the sun gear and carrier plate can be analysed by following the procedure presented for the vibrations.

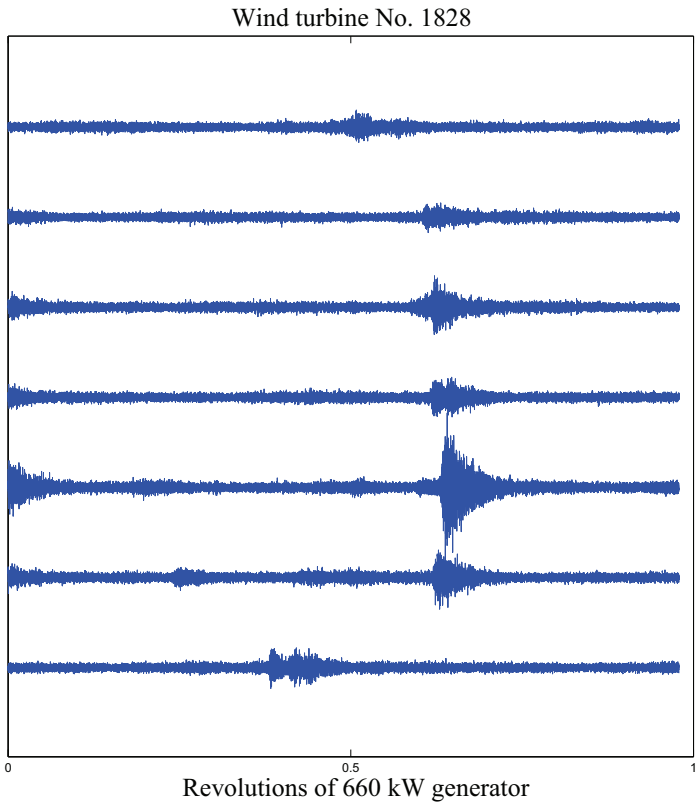

Figure 2.17: Several synchronized portions of the AE signal measured in the PG of a wind turbine.

where:

- $y_i^r(t)$ are the AE generated in the meshing of the i-th planet gear with the ring gear, as measured by the sensor installed on the outer part of the ring gear.

- $\{A_k^i\}_{k\in\mathbb{Z}}$ is a periodically delta-correlated random point process, which is correlated with a periodic process with period T_C, to account for the amplitude modulation due to the variable transfer function from the source of the AE to the sensor, such that $\mathbb{E}\{A_k^i\} = \mathbb{E}\left\{A_{k+T_C}^i\right\} = \overline{A_k^i}$, where $\mathbb{E}\{\cdot\}$ is the expected value. The superscript i is used in the notation to account for differences between the statistical characteristics of the processes generated in the meshing of each of the planet gears with the ring gear. The notation $A_{k_{\left(t_1+\frac{\psi_i T_C}{2\pi}\right)}}$ used in eq. (2.36) refers to the periodically delta-correlated random point that is correlated with the same periodic process with which the process $\{A_k^i\}_{k\in\mathbb{Z}}$ is correlated, but that is time-shifted by an amount $t_1 + \frac{\psi_i T_C}{2\pi}$. This permits to define the amplitude modulation function for the i-th planet as a time-shifted version of the amplitude modulation function of the first planet, by considering the relative angular

position of the planet gears in the PG. The time shift t_1 accounts for the unknown position of the planet gears at the start of the measurement. Put in simple words, the random point process $\{A_k^i\}_{k\in\mathbb{Z}}$ accounts for random deviations of the AE burst from the periodic process with period T_C that describes the amplitude modulation effect due to the variable transmission path.

- $s(t)$ is the AE time waveform generated due to the impact generated by asperity contact at the pure rolling portion during the meshing of two teeth.
- T_g^p is the gear meshing period (i.e. the inverse of the gear meshing frequency f_g^p).
- $\{\tau_k^i\}_{k\in\mathbb{Z}}$ is a zero-mean delta-correlated random point process with probability density function (PDF) $\varphi_\tau(\tau_k^i)$. The superscript i indicates that this process can have different statistic characteristics for the AE coming from each of the planet-ring gear meshes. This process accounts for random variations in the time of ocurrence of the AE bursts.
- $\{n(t)\}_{t\in\mathbb{R}}$ is a zero-mean stationary additive background noise that accounts for other sources of AE.

The random variations in amplitude and time of arrival of the AE bursts, which are taken into account in the model of eq. (2.36) by the random processes $\{A_k^i\}_{k\in\mathbb{Z}}$ and $\{\tau_k^i\}$, are probably due to the high sensitive characteristics of the mechanism of generation of the AE. Further, it is noted that the model presented in eq. (2.36) incorporates the randomness of the arrival times around a fixed mesh of period T_g^p.

2.3.2. Analysis of the deterministic part

The deterministic part is analysed by taking the expected value of $y(t)$. Considering the AE coming from the meshing of a single planet gear with the ring gear, that is:

$$\begin{aligned} m_{y_i}^r(t) &= \mathbb{E}\{y_i^r(t)\} \\ &= \mathbb{E}\left\{\sum_k A_{k_{\left(t_1+\frac{\psi_i T_C}{2\pi}\right)}}^i\right\}\mathbb{E}\left\{s\left(t-kT_g^p-\tau_k^i-\gamma_{ri}T_g^p\right)\right\}+\mathbb{E}\{n(t)\} \\ &= \sum_k \overline{A_{k_{\left(t_1+\frac{\psi_i T_C}{2\pi}\right)}}^i}\int_{\mathbb{R}} s\left(t-kT_g^p-\tau_k^i-\gamma_{ri}T_g^p\right)\varphi_\tau\left(\tau_k^i\right)\,d\tau_k^i \end{aligned} \tag{2.37}$$

where use has been made of the properties of $\{A_k^i\}_{k\in\mathbb{Z}}$ and $\{n(t)\}$, and the fact that both are independent processes. Also the statistical definition of the expected value $\mathbb{E}\{X\} = \int_{-\infty}^{+\infty} xf(x)\,dx$ has been used, where $f(x)$ is the PDF. The integral in eq. (2.37) can be expressed as a convolution, so that the deterministic part of $y_i^r(t)$ becomes:

$$m_{y_i}^r(t) = \sum_k \overline{A_k^i}_{\left(t_1+\frac{\psi_i T_C}{2\pi}\right)} s\left(t-(k+\gamma_{ri})T_g^p\right) * \varphi_\tau(t) \tag{2.38}$$

Following the procedure of [RAC01], now $m_{y_i}^r(t)$ is analysed in the frequency domain, for which the Fourier transform (FT) of eq. (2.38) is calculated.

$$\begin{aligned} M_{y_i}^r(f) &= \mathcal{F}\left\{m_{y_i}^r(t)\right\} \\ &= \sum_k \overline{A_k^i}_{\left(t_1+\frac{\psi_i T_C}{2\pi}\right)} \mathcal{F}\{s(t)\} e^{-j2\pi f(k+\gamma_{ri})T_g^p} \mathcal{F}\{\varphi_\tau(t)\} \\ &= \sum_k \overline{A_k^i}_{\left(t_1+\frac{\psi_i T_C}{2\pi}\right)} S(f)\,\Phi_\tau^{i\,*}(f)\, e^{-j2\pi f(k+\gamma_{ri})T_g^p} \end{aligned} \tag{2.39}$$

where $S(f)$ is the FT of $s(t)$, and $\Phi_\tau^i(f)$ is the characteristic function of the process $\{\tau_k^i\}_{k\in\mathbb{Z}}$. Considering that $\overline{A_k^i}_{\left(t_1+\frac{\psi_i T_C}{2\pi}\right)}$ is periodic with period $T_C = 1/f_C$; it can be expressed as a Fourier series (FS). After substitution of the FS and rearrangement, eq. (2.39) yields:

$$M_{y_i}^r(f) = \sum_k \sum_q a_q^i e^{j2\pi k T_g^p (qf_C - f)} S(f)\,\Phi_\tau^{i\,*}(f)\, e^{-j2\pi q f_C\left(t_1+\frac{\psi_i T_C}{2\pi}\right)} e^{-j2\pi f\gamma_{ri}T_g^p} \tag{2.40}$$

where a_q^i are the Fourier coefficients of $\overline{A_k^i}$, and $q \in \mathbb{Z}$. Using Poisson's summation formula[5], the following result is obtained for $M_{y_i}^r(t)$:

$$M_{y_i}^r(f) = \sum_k \sum_q \frac{a_q^i}{T_g^p} S(f)\,\Phi_\tau^{i\,*}(f)\, e^{-j2\pi q f_C t_1} e^{-jq\psi_i} e^{-j2\pi f\gamma_{ri}T_g^p} \delta\left(f - kf_g^p - qf_C\right) \tag{2.41}$$

It is noted from eq. (2.41), that $M_{y_i}^r(f)$ takes non-zero values only for the frequencies $f = kf_g^p + qf_C$.

Since in the PG all N planet gears mesh with the ring gear simultaneously, the sensor experiences the sum of the AE generated in each of the planet-ring gear meshing. Invoking its

[5]The Poisson's summation formula is given by $\sum_{k=-\infty}^{+\infty} \delta(t-kT) = \frac{1}{T}\sum_{k=-\infty}^{+\infty} e^{j2\pi kt/T}$

linearity property, the FT of the deterministic part of the AE coming from the meshing of all planet gears with the ring gear as measured by the sensor, $M_y^r(t)$, is given by:

$$\begin{aligned} M_y^r(f) &= \sum_{i=1}^{N} M_{y_i}^r(t) \\ &= \frac{1}{T_g^p} \sum_q \sum_k \sum_{i=1}^{N} a_q^i S(f) \Phi_\tau^{i\,*}(f) e^{-j2\pi q f_C t_1} e^{-jq\psi_i} e^{-j2\pi f \gamma_{ri} T_g^p} \delta\left(f - k f_g^p - q f_C\right) \end{aligned} \tag{2.42}$$

It is noted in eq. (2.42), that for a given frequency $f = k f_g^p + q f_C$, the amplitude of $M_y^r(t)$ is determined by the interaction of N components, each with the same frequency and with an amplitude given by the term $\frac{a_q^i S(f) \Phi_\tau^{i\,*}(f)}{T_g^p}$. From this term, a_q^i and $\Phi_\tau^{i\,*}(f)$ are dependent on the planet gear i, so that the amplitude of the N components will be (generally) different. This, under consideration of the influence of the relative phase of each component (which is given by the term $e^{-jq\psi_i} e^{-j2\pi f \gamma_{ri} T_g^p}$), will typically produce no suppresion of components in the spectrum of the AE measured by the sensor, so that a spectrum with components at all $f = k f_g^p + q f_C$ is expected. Depending on the degree of randomness of the processes involved, and on the group the PG pertains, particular structures of the spectrum can be found. However, the structural analysis of the spectrum is not straightforward, because the characteristics of the random processes are difficult to estimate, as they can depend on many variables of the system.

It is also important to note that according to the theory of probabilities, the term $\Phi_\tau^{i\,*}(f)$ in (2.42) is such that $\left|\Phi_\tau^{i\,*}(f)\right| \leq \Phi_\tau^{i\,*}(0) = 1$, which defines a low-pass filter [RAC01][MC04]. Therefore, the deterministic part of the AE is constrained to the low frequencies only.

2.3.3. Analysis of the stochastic part

The stochastic part of the AE signal can be obtained simply by substracting the deterministic part from the original signal. However, due to the low-pass filter effect of the term $\Phi_\tau^{i\,*}(f)$, the influence of the deterministic part is negligible in the high frequencies, so that in this portion the signal can be considered purely stochastic. Since AE are high frequency signals by nature, they are primarily stochastic signals. This is confirmed by fig. 2.18, which shows in the upper plot the original AE signal measured in a PG. The middle plot shows the estimation of the

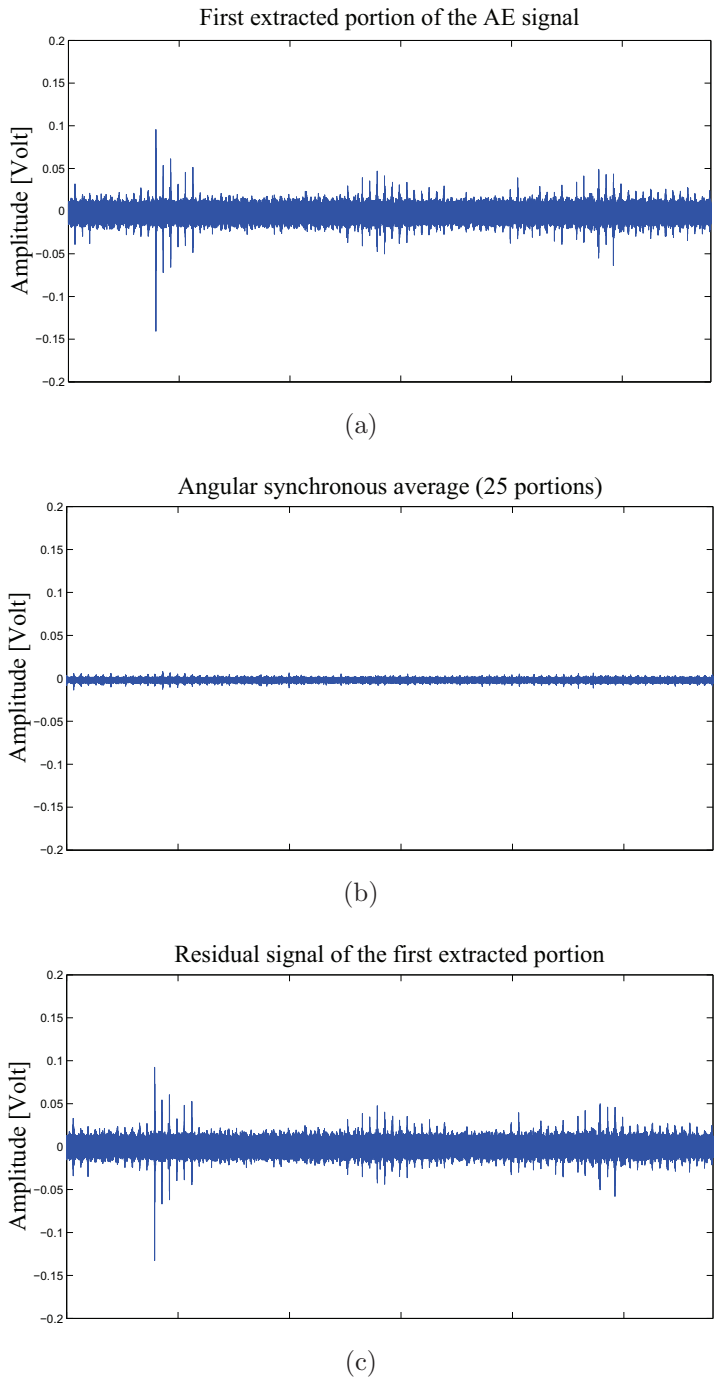

Figure 2.18: One carrier rotation portion of the (a) original AE signal, (b) deterministic part, and (c) stochastic part.

deterministic part of the signal, which was obtained by angular synchronous averaging based on the carrier rotation period. The lower plot shows the residual signal obtained by substraction of the estimated deterministic part from the original AE signal. The high stochastic characteristic of the signal is evident from this figure.

For the analysis, the autocovariance function (ACVF) is considered, which completely characterises the second-order statistics[6] of the stochastic part, which are related to the energy intensity and interactions [Ant07]. The ACVF is defined as:

$$K^r_{yy_i}(t,\,\tau) \triangleq \mathbb{E}\left\{\left[y^r_i\left(t+\frac{\tau}{2}\right)-m^r_{y_i}\left(t+\frac{\tau}{2}\right)\right]\left[y^r_i\left(t-\frac{\tau}{2}\right)-m^r_{y_i}\left(t-\frac{\tau}{2}\right)\right]^*\right\} \tag{2.43}$$

It can be demonstrated that:

$$K^r_{yy_i}(t,\,\tau) = R^r_{yy_i}(t,\,\tau) - \mathbb{E}\left\{y^r_i\left(t+\frac{\tau}{2}\right)\right\}\mathbb{E}\left\{y^{r*}_i\left(t-\frac{\tau}{2}\right)\right\} \tag{2.44}$$

where $R^r_{yy_i}(t,\,\tau) = \mathbb{E}\left\{y^r_i\left(t+\frac{\tau}{2}\right)y^{r*}_i\left(t-\frac{\tau}{2}\right)\right\}$ is the autocorrelation function (ACF).

From the proposed AE model of eq. (2.36), one has:

$$y^r_i(t) = \underbrace{\sum_k A^i_{k_{\left(t_1+\frac{\psi_i T_C}{2\pi}\right)}}\, s\left(t-kT^p_g-\tau^i_k-\gamma_{ri}T^p_g\right)+n(t)}_{a(t)} \tag{2.45}$$

It is assumed that the random processes $\{A^i_k\}, \{\tau^i_k\}$ and $\{n(t)\}$ are mutually uncorrelated (i.e. the cross-correlations between $a(t)$ and $n(t)$ are zero: $R_{an}(t,\,\tau) = R_{na}(t,\,\tau) = 0$). Thus, based on (2.44), to calculate the ACVF $K^r_{yy_i}(t,\,\tau)$, first the ACF $R^r_{yy_i}(t,\,\tau)$ is calculated as:

$$R^r_{yy_i}(t,\,\tau) = R_{aa}(t,\,\tau) + R_{nn}(t,\,\tau) \tag{2.46}$$

where $R_{aa}(t,\,\tau)$ is the ACF of $a(t)$ in eq. (2.45); and $R_{nn}(t,\,\tau)$ ist the ACF of $n(t)$. After some calculation steps, the following result is obtained for $R_{aa}(t,\,\tau)$ in eq. (2.46):

$$\begin{aligned} R_{aa}(t,\,\tau) &= \sum_k \overline{A^i_{k_{\left(t_1+\frac{\psi_i T_C}{2\pi}\right)}}}^{\,2} f(t,\,\tau) \\ &\text{where} \\ f(t,\,\tau) &= \int s\left(t+\frac{\tau}{2}-(k+\gamma_{ri})T^p_g-\tau^i_k\right)s^*\left(t-\frac{\tau}{2}-(k+\gamma_{ri})T^p_g-\tau^i_k\right)\varphi_\tau\left(\tau^i_k\right)\,d\tau^i_k \end{aligned} \tag{2.47}$$

[6] The analysis up to the second order is mostly sufficient for the description of the signal

The integral $f(t,\,\tau)$ is recognized as a convolution, so that eq. (2.46) yields:

$$\begin{aligned} R^r_{yy_i}(t,\,\tau) &= \sum_k \overline{A^i_{k_{\left(t_1+\frac{\psi_i T_C}{2\pi}\right)}}}^{\,2} \left[s\left(t+\frac{\tau}{2}-(k+\gamma_{ri})\,T_g^p\right) s^*\left(t-\frac{\tau}{2}-(k+\gamma_{ri})\,T_g^p\right)\right] * \varphi_\tau(t) \\ &\quad + R_{nn}(t,\,\tau) \end{aligned} \tag{2.48}$$

Substituting eq. (2.48) into eq. (2.44), and using the result obtained in eq. (2.38), the following expression for the ACVF is obtained:

$$\begin{aligned} K^r_{yy_i}(t,\,\tau) &= \sum_k \overline{A^i_{k_{\left(t_1+\frac{\psi_i T_C}{2\pi}\right)}}}^{\,2} \left[s\left(t+\frac{\tau}{2}-(k+\gamma_{ri})\,T_g^p\right) s^*\left(t-\frac{\tau}{2}-(k+\gamma_{ri})\,T_g^p\right)\right] * \varphi_\tau(t) - \\ &\quad \sum_k \overline{A^i_{k_{\left(t_1+\frac{\psi_i T_C}{2\pi}\right)}}}^{2} \left[s\left(t+\frac{\tau}{2}-(k+\gamma_{ri})\,T_g^p\right) * \varphi_\tau(t)\right] \left[s\left(t-\frac{\tau}{2}-(k+\gamma_{ri})\,T_g^p\right) * \varphi_\tau(t)\right]^* \\ &\quad + K_{nn}(t,\,\tau) \end{aligned} \tag{2.49}$$

where $K_{nn}(t,\,\tau) = R_{nn}(t,\,\tau)$, because $\mathbb{E}\left\{n\left(t+\frac{\tau}{2}\right)\right\} = \mathbb{E}\left\{n^*\left(t-\frac{\tau}{2}\right)\right\} = 0$. Eq. (2.49) shows that the ACVF depends not only on the time lag τ, but also on the instantaneous time t, which means that the stochastic part is non-stationary. To evaluate the spectral structure of the signal, the power spectral density (PSD) $P^r_{y_i}(f)$ of the stochastic part is calculated from the ACVF. The result of this is given in eq. (2.50).

$$P^r_{y_i}(f) = \frac{1}{T_g^p} \sum_q \sum_k |S(f)|^2 \left[b_0^i - c_0^i |\Phi_\tau(f)|^2\right] e^{-j2\pi q f_C t_1} e^{-jq\psi_i} + P_n(f) \tag{2.50}$$

where $S(f)$ is the FT of $s(t)$; b_0^i is the mean value of $\overline{A^i_{k_{\left(t_1+\frac{\psi_i T_C}{2\pi}\right)}}}^{\,2}$; c_0^i is the mean value of $\overline{A^i_{k_{\left(t_1+\frac{\psi_i T_C}{2\pi}\right)}}}^{2}$; and $P_n(f)$ is the PSD of $n(t)$. It is noted that the term between brackets acts as a high-pass filter, because $\left|\Phi^{i\,*}_\tau(f)\right| \leq \Phi^{i\,*}_\tau(0) = 1$. It is also noted from eq. (2.50) that due to the characteristics of $S(f)$, $P^r_{y_i}(f)$ is a continuous function of f. As a result, the spectral structure of $P^r_{y_i}(f)$ does not show any discrete component.

It must be recalled, that $P^r_{y_i}(f)$ represents the PSD of the stochastic part of the AE signal when only one planet i is considered. When all planets are considered, the sum of the AE

generated in each planet/ring mesh must be taken into account:

$$P_y^r(f) = \sum_{i=1}^{N} P_{y_i}^r(f) \tag{2.51}$$

As observed from eq. (2.51), the structure of $P_y^r(f)$ is also continuous in f.

Finally, the sensor will experience the deterministic and the stochastic part of the AE coming from all planet/ring meshes simultaneously. The degree of randomness of the processes involved in the signal will define the proportion between the two parts. From the measurements carried out during the development of this work, it was observed that the influence of the stochastic part is such that the discrete components from the deterministic part are not recognizable. Accordingly, the frequency content analysis of the AE observed in a PG is not possible with the conventional stationary signal processing tools such as the FT or PSD. This result is expected from fig. 2.18, from which is clear that the AE signal is mainly non-stationary. Cyclostationary[7] tools such as the envelope spectrum, spectral correlation density or spectral coherence are suitable for the analysis of this kind of signals, since they aim to describe the periodicities of the energy flow of the signal rather than the periodicities of the signal itself.

It is important to understand that the differences in the spectral structure of the models proposed for the vibrations and AE (i.e. discrete spectrum vs. continuous spectrum) is due to the different characteristics of the mechanisms involved in the generation of each of them. Thus, vibrations were considered periodic, whereas in the AE some random fluctuations are allowed.

2.3.4. Cyclostationarity

In this section a brief overview of the theory of cyclostationarity is presented. Through this, it is intended to clarify some definitions, present the most important results and, essentially, to provide the reader with a synopsis of cyclostationarity. The content presented in this section is based mainly in the following works [Gar87] [Gar91] [Ga94] [Gia99] [RAC01] [ABREB04] [Ant07] [Ant09]. The reader interested in more about this subject is kindly asked to refer to these excellent references.

[7] more about cyclostationarity will be presented in section 2.3.4

2.3.4.1. Definition

Cyclostationary signals are a type of non-stationary signals whose statistical properties change periodically with time (or angle of rotation). This is in opposition to stationary signals, whose statistical properties remain constant with time; and to random signals, whose statistical properties change (but not periodically) with time. Cyclostationary signals are generally random in its waveform, but exhibit some hidden periodicity in its energy flow, which is generated by some periodic process. The period of the hidden periodic process in the signal is called *cycle*; and its inverse, *cyclic frequency*, which is denoted by the symbol α.

In mechanical systems it is usual to find periodic movements of mechanical components that modulate the vibration or sound being generated, as is the case in gears, reciprocating machines, etc., thus constituting cyclostationary signals. Actually, the stationary approach is hardly met in reality even in mechanical systems working at constant operating conditions of torque, rotational speed, etc. Interestingly, cyclostationary signals include periodic and random stationary signals as particular cases. Hence, the cyclostationary approach should be taken whenever possible [Ant07][Ant09].

Formally, a signal *exhibits* cyclostationarity if exists a combination of linear and non-linear transformations that produces periodic components as a result. It is said that a signal exhibits cyclostationarity at the cyclic frequency α, if there is a combination of linear and non-linear transformations that produce a pure sinusoidal with frequency α.

2.3.4.2. Order of cyclostationarity

Relying on the formal definition given above, the *order of cyclostationarity* is determined by the maximum order of the transformations used to obtain periodic components. According to this, following definitions are made:

1. A signal is *first-order cyclostationary (CS1)* with fundamental cycle T, if only a linear transformation is sufficient to obtain a periodic signal. In particular, if the first-order moment is periodic with fundamental period T; mathematically:

$$m_X(t) \triangleq \mathbb{E}\{X(t)\} = m_X(t+T) \tag{2.52}$$

CS1 signals show periodic time histories, such as the observed in vibrations generated by unbalance, eccentricity, gear meshing, flexible couplings, etc. Some additive random stationary background noise can be present.

2. A signal is *second-order cyclostationary (CS2)* with fundamental cycle T, if the order of the non-linear transformation needed to obtain a periodic signal is two. In particular, if its second-order moment (i.e. the autocorrelation function, ACF) is periodic with fundamental period T; mathematically:

$$R_{XX}(t_1, t_2) \triangleq \mathbb{E}\{X(t_1) X^*(t_2)\} = R_{XX}(t_1 + T, t_2 + T) \tag{2.53}$$

CS2 signals are stochastic processes with periodic amplitude or/and frequecy modulations, such as the vibrations generated by impact forces, friction forces, combustion forces, the AE generated in the meshing process of gears, etc.

3. A signal is *n-th-order cyclostationary (CSn)* with fundamental cycle T, if the order of the non-linear transformation needed to obtain a periodic signal is $n > 2$. Such signal is also called high-order cyclostationary [GS94].

Furthermore, a process which is both CS1 and CS2 is called *wide-sense* cyclostationary; whereas a process whose moments till infinity are periodic is called *strict-sense* cyclostationary.

2.3.4.3. Poly-cyclostationarity

It is noted that the definitions 1, 2 and 3 of the previous section assume the existence of a single periodic process with fundamental cycle T. However, a signal can contain several hidden periodic processes with different fundamental cycles. According to this, it is distinguished between a signal which *exhibits* cyclostationarity and a signal which *is* cyclostationary at a given order. Denoting by $\mathcal{A}$ the set of all cyclic frequencies α present in the signal obtained after the appropriate linear and non-linear transformations:

- A signal *exhibits* cyclostationarity at a cyclic frequency α, if the set $\mathcal{A}$ contains α and its multiples, *among other* cyclic frequencies.

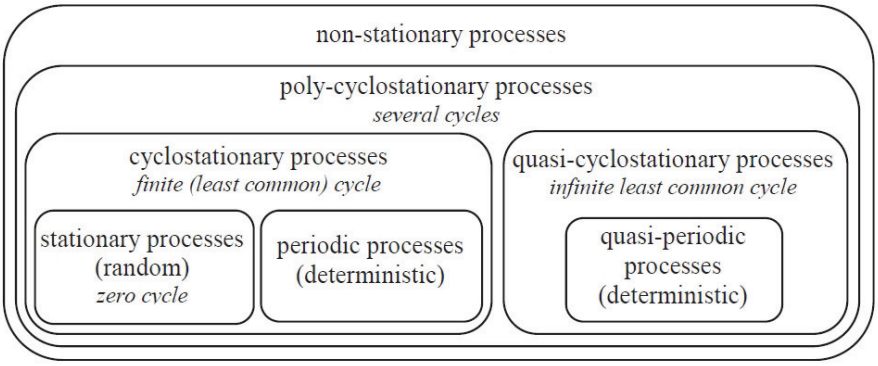

Figure 2.19: Different types of processes and their relation [ABREB04].

- A signal *is* cyclostationary at a cyclic frequency α, if the set $\mathcal{A}$ contains *only* α and its multiples.

Moreover, if for a signal which exhibits cyclostationarity, the cyclic frequencies contained in $\mathcal{A}$ are such that they share no integer common factor, the signal is said to be poly-cyclostationary.

Fig. 2.19 shows a representation of the different types of processes revised in this section, and how they are related. In this figure, a block inside a larger block means that the former is a particular case of the latter.

2.3.4.4. Pure and impure cyclostationarity

From the definitions of section 2.3.4.2, it is noted that a signal which is first-order cyclostationary, will be cyclostationary at all orders. For example, the ACF of a periodic signal $p(t)$ is:

$$R_{PP}(t_1, t_2) \triangleq \mathbb{E}\{p(t_1)\, p^*(t_2)\} = p(t_1)\, p^*(t_2) = m_P(t_1)\, m_P^*(t_2) \tag{2.54}$$

The ACF in eq. 2.54 is periodic, because it depends on the first-order moment $m_p(t)$, which is periodic. The same occurs for higher orders. Hence, all moments of a periodic signal are periodic. However, the periodicity of the moments of order $n > 1$ is only a result of the periodicity of the first-order moment. Hence, a periodic signal is *pure* cylclostationary at the first order (denoted PCS1), but *impure* at higher orders. Distinguishing between pure and impure cyclostationarity is important, because a PCS1 signal does not require the cyclostationary approach for its analysis, since the classical stationary approach suffices.

In order to distinguish between pure and impure cyclostationarity, the cumulant functions – instead of the moments– are used. For example, the cumulant function of second order (i.e. the autocovariance function, ACVF) substracts the impure terms induced by the first order moment, thus allowing to evaluate the pureness of the second-order cyclostationarity. The same holds for higher orders, where higher-order cumulant functions are used. In the example of the periodic signal, its ACVF reads:

$$\begin{aligned} K_{PP}(t_1, t_2) &\triangleq \mathbb{E}\left\{\left[p(t_1) - m_P(t_1)\right]\left[p^*(t_2) - m_P^*(t_2)\right]\right\} \\ &= R_{PP}(t_1, t_2) - m_P(t_1)\, m_P^*(t_2) = 0 \end{aligned} \tag{2.55}$$

This result reflects no cyclostationarity at the second order for the periodic signal $p(t)$. Accordingly, the ACVF should be used instead of the ACF to evaluate if a process is PCS2.

2.3.4.5. Why cyclostationarity?

The cyclostationary approach presents several advantages for the fault diagnosis of mechanical systems through the assessment of variables such as vibrations and AE. This comes from the fundamental fact that the observed signals hardly meet the stationary condition, which is inherently assumed when processed with conventional tools such as the Fourier transform or the power spectral density (PSD). It is clear from fig. 2.19, that cyclostationary encompasses a larger family of signals and, therefore, is a more general and powerful approach than the stationary. In the last years of research in the field of cyclostationarity applied to the fault detection of rotating machines, it has been found that in several cases the signals from a non-faulty system are generally stationary; whereas under the presence of a fault the signals have a cyclostationary behaviour. This is because a fault typically produces a strong and repetitive release of vibration energy.

Important results have been obtained in the application of cyclostationarity to machine's fault detection. For example, in the field of gear diagnosis, it has been found that some failures like spalling produce periodic modulations in the signal which are well detected using the cyclostationary approach [CSL00]. Interestingly, it has been postulated that low-frequency vibrations measured in gears behave as CS1 signals, whereas high-frequency vibrations present

PCS2 characteristics. Moreover, it has been argumented that the former is a result of the macro phenomena, and the latter is a result of the micro-phenomena involved in the gearing process [RAS08]. This is in perfect accordance with the observations made in the model development of the AE for planetary gearboxes presented in section 2.3.1. The field of bearing diagnosis is a classical example of vibration signals that are mostly stationary –mostly stationary noise– when the bearing suffers no failure, and are CS2 (or PolyCS2) under the presence of localized faults. Transients are observed in the signal each time a rolling element roll over the damaged zone [RAC01][AR02][AR03]. A third example of cyclostationary signals from mechanical systems are the vibrations and sound observed in reciprocating machines (e.g. compressors, internal combustion engines). Such systems operate in a cyclic manner, undergoing a series of non-stationarities produced by different angle-locked events, such as openings and closings of valves.

In relation to AE signals, much more insight can be gained provided they are treated under the cyclostationary approach. This is mainly due to their high "transient nature". In fact, the stationary approach would provide no useful information, as was shown in the frequency analysis presented in sections 2.3.2 and 2.3.3.

2.3.4.6. Signal processing tools for cyclostationary analysis

Cyclostationary-based signal processing (SP) tools exploit the special properties of cyclostationary (CS) signals to reveal their hidden periodicities, thus providing more information than the usual stationary SP tools. Again, if a signal is stationary, then no new information will be obtained by using cyclostationary SP tools.

In order to illustrate what cyclostationary SP tools essentially do, the simple interpretation presented in [Ant09] is used. Fig. 2.20 shows the typical filterbank interpretation of the PSD $P_x(f)$, which is a measure of the frequency distribution of the energy carried by the signal. In this figure, the signal $x(t)$ is passed through a bank of narrow band band-pass filter of width Δ_f, centered on the frequency f_i. From each of the filtered signals $x_{\Delta_f}(t;\, f)$, the average power $P_x(f_i;\, \Delta_f)$ is calculated as : $P_x(f_i;\, \Delta_f) = \lim_{T\to\infty} \frac{1}{T} \int_T \left| x_{\Delta_f}(t,\, f) \right|^2 dt$, which is a constant value as shown in the figure. The PSD $P_x(f)$ is obtained by repeating the procedure for all filtered signals while taking the limit as $\Delta_f \to 0$ and normilising by Δ_f. It is well known that if the signal contains some periodic components, the PSD will reveal them as discrete lines at

the corresponding frequencies; if not, the PSD will be a continuous function of f (even if the signal presents hidden periodicities!).

The key idea of cyclostationary-based SP tools consists in decomposing the energy flow of the filtered signals not into a constant value –as done in the PSD–, but into periodic values, thus revealing the frequency structure of the energy flow with time. The process is illustrated in fig. 2.21. Here, the first steps are as in the PSD. However, from each filtered signal $x_{\Delta_f}(t;\, f_i)$ no constant value is calculated. Instead, the mean instantaneous power of each filtered signal $P_x(t,\, f_i;\, \Delta_f)$ is determined. The collection of all mean instantaneous powers, which is a time-frequency representation, is called *instantaneous power spectrum* $P_x(t,\, f;\, \Delta_f)$, and reveals the frequency structure of the energy flow in time. The evaluation of the periodicitiy of the instantaneous power spectrum is a natural step forward, which is accomplished by the determination of its Fourier coefficients. Actually, it is this key step which reveals the hidden periodicities (if existent) of the signal. The collection of Fourier coefficients is called *cyclic modulation spectrum* denoted by $P_x^{\alpha}(f;\, \Delta_f)$, and is a frequency-cyclic frequency representation (fig. 2.21).

Considering that the envelope of a signal is some function that envelopes the fluctuations of its energy flow as a function of time, the instantaneous power spectrum can be interpreted as a collection of envelopes of succesive band-pass-filtered versions of the signal. However, the introduction of the filterbank in the definition of the instantaneous power spectrum makes it a more powerful tool. Indeed, the integral of the instantaneous power spectrum along the f-axis would merge the set of all envelopes into a single waveform similar to the classical envelope. The same relation is observed between the cyclic modulation spectrum and the envelope spectrum.

The instantaneous power spectrum $P_x(t,\, f;\, \Delta_f)$ and the cyclic modulation spectrum $P_x^{\alpha}(f;\, \Delta_f)$ are affected by the uncertainty principle and, therefore, constitute no densities. As such, they do not conserve energy and are not unique. More advanced signal processing tools have been developed, which overcome this problem. Basically, they exploit the property that hidden periodicities produce correlation in the frequency domain. This property, also called "*spectral redundancy*"[Gar91][Ga94], provides the basis for the development of one of the most powerful cyclostationary SP tools: the *spectral correlation density (SCD)*. The SCD, mathematically

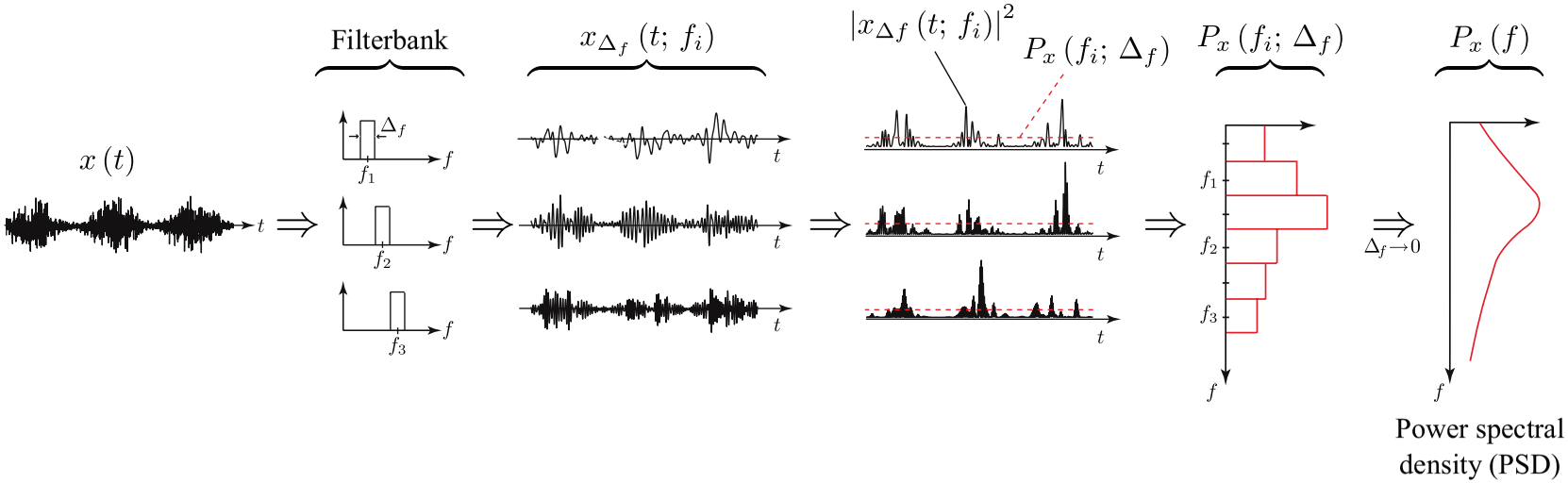

Figure 2.20: Filterbank interpretation of the PSD (figure adapted from [Ant09]).

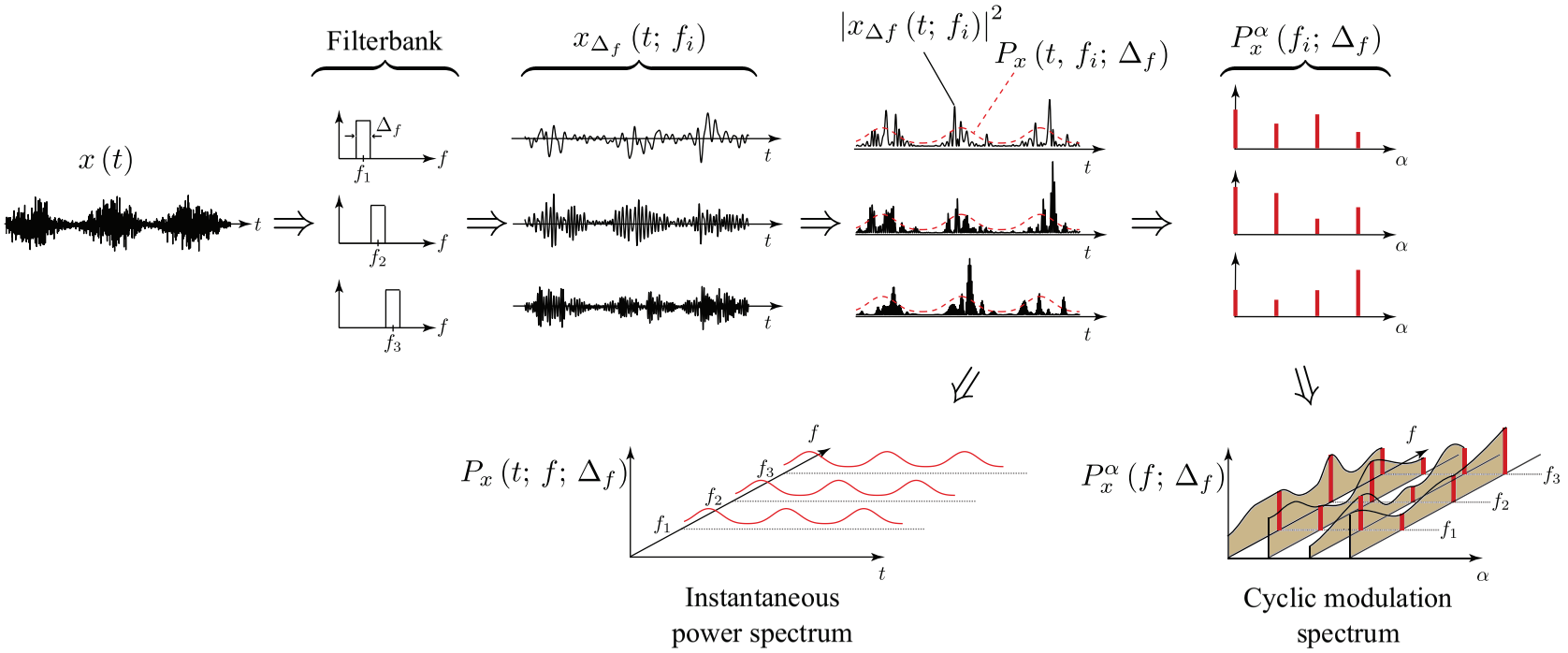

Figure 2.21: Filterbank interpretation of the *instantaneous power spectrum* and *cyclic modulation spectrum* (figure adapted from [Ant09]).

defined as

$$S_{xx}^{\alpha}(f) = \lim_{\Delta_f \to 0} \lim_{T \to \infty} \frac{1}{T\Delta_f} \int_T x_{\Delta_f}(t;\, f + \alpha/2)\, x_{\Delta_f}^{*}(t;\, f - \alpha/2)\, e^{-j2\pi\alpha t}\, dt \tag{2.56}$$

is indeed a density and, therefore, is unique, thus overcoming the problems of the previous tools. It is noted that as a particular case, when $\alpha = 0$ the SCD becomes the PSD. Energy normalisation of the SCD results in the *spectral coherence (SCoh)*, whose squared magnitude takes values only between 0 and 1 and provides a unitless measurement of the strength of correlation in the frequency domain. The SCoh is mathematically defined as:

$$\gamma_{xx}^{\alpha}(f) = \frac{S_{xx}^{\alpha}(f)}{\sqrt{S_{xx}^{0}(f + \alpha/2)\sqrt{S_{xx}^{0}(f - \alpha/2)}}} \tag{2.57}$$

Several estimators of the SCD and SCoh have been proposed, the most spread being the based in the *averaged cyclic periodogram*. A thorough review of this subject is presented in [Ant07].

Relation with conventional SP tools

The relation between the cyclic modulation spectrum and the SCD is that the latter, being a density, is a fundamental constituent of the former [Ant09]. The same is valid between the instantaneous power spectrum and the quantity known as the *Wigner-Ville spectrum*. The Wigner-Ville spectrum is, in turn, related to the SCD in the same manner as the instantaneous power spectrum relates to the cyclic modulation spectrum (see fig 2.22). The Wigner-Ville spectrum is related to the Wigner-Ville *distribution*, which is a (more) known time-frequency distribution, being equal to the mean value of it.

A formal proof of the relation between the SCD and the envelope spectrum is given in [RAC01]. It states that if the signal is dominated by the stochastic part (as is ussually the case for the high frequencies, in particular for AE signals), the integral along f of the SCD is equivalent to the Fourier transform of the envelope of the squared signal, i.e.:

$$\int_{\mathbb{R}} S_{xx}^{\alpha}(f)\, df = \lim_{W \to \infty} \frac{1}{W} \int_W \mathbb{E}\left\{|x(t)|^2\right\} e^{-j2\pi\alpha t}\, dt \tag{2.58}$$

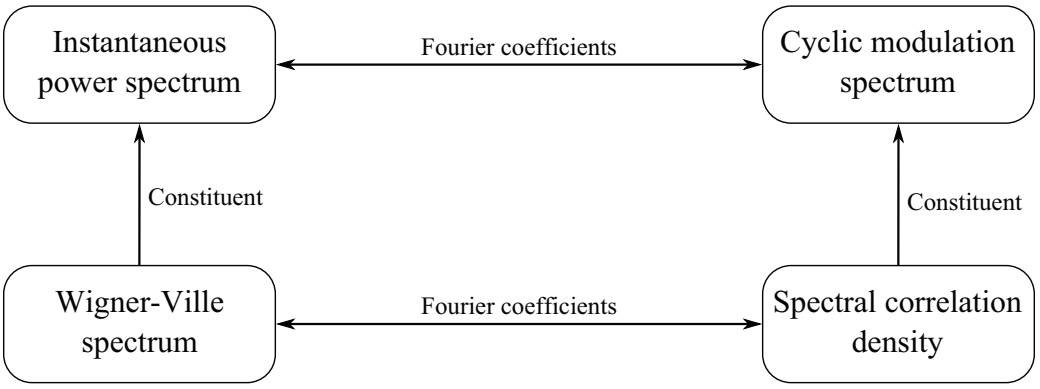

Figure 2.22: Relation between different cyclostationary quantities.

This important result should make clear that the well known envelope signal processing constitutes fundamentally a cyclostationary tool[8]. Eq. (2.58) provides a rich cyclostationary background to this classical tool. Furthermore, it shows that the envelope is a particular case of the SCD.

2.3.4.7. Bearing fault detection with cyclostationary tools

Rolling element bearing diagnosis is probably the area within machine diagnosis that has taken more profit from cyclostationarity. This is because it has been observed that the vibration signals exhibit high leveles of second-order cyclostationarity under the presence of localized faults. In this case the signal contains a series of apparently periodic high frequency transients with possible amplitude modulation depending on the location of the fault (inner ring, outer ring or rolling element).

Further analysis of the signals showed that the transients do not occur under a periodic basis, as apparent from the signals. The time interval between two succesive transients is actually a random variable. The reason for this relies on the random slip existing between rolling elements and the rolling races, which is caused by the different load distribution around the bearing [RAC00]. As a result, the signal is not periodic, but exhibits second-order cyclostationarity. Accordingly, CS-based tools are best suited to reveal the fault, even when masked by other sources of vibrations contained in the signal.

[8]Moreover, the author proposes the use of the cyclic frequency α instead of frequency f in the abscissa of the envelope spectrum

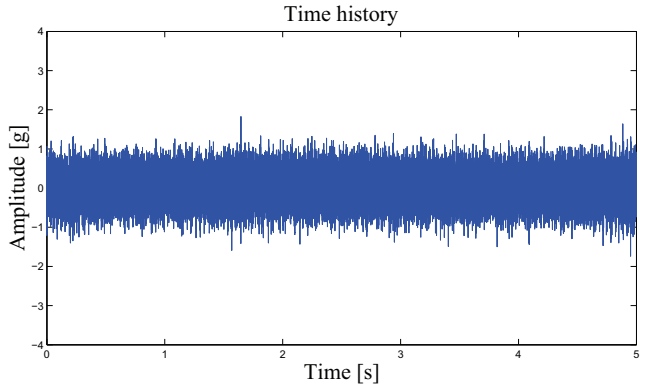

(a)

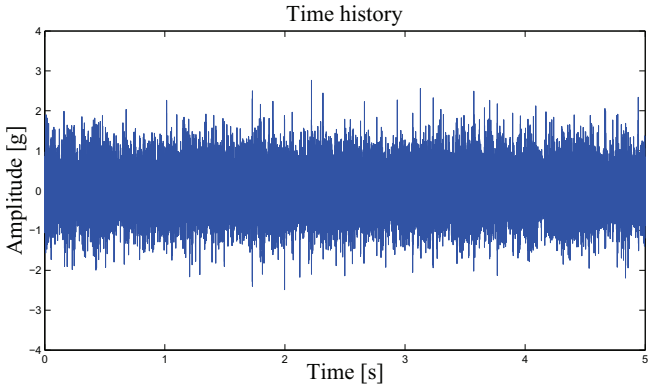

(b)

Figure 2.23: Time histories of vibrations measured (a) without failure, (b) with a localized fault in the outer race.

An example should clarify the advantages of the cyclostationary approach. Fig. 2.23a shows the time history of a vibration signal measured on a test bench with a non-faulty bearing; fig. 2.23b shows the signal after replacement by a bearing with a localized fault in the outer race. The rotational frequency is in both cases of 30 Hz, for which a fault frequency of ≈ 94.8 Hz is expected.

The next step usually consists in evaluating the FFT-Spectrum, which corresponds to the stationary approach. Fig. 2.24 shows the spectrum of both signals of fig. 2.23. In both spectrums some discrete components are found in the low frequency range, which are caused by some periodic process involved in the machine. Only a very slight change in amplitude in the high frequency range is observed, but no discrete component is recognized.

Following, the spectral coherence (SCoh) is calculated for both signals and are presented in fig. 2.25. From fig. 2.25a it is noted that the SCoh of the non-faulty case presents some non-

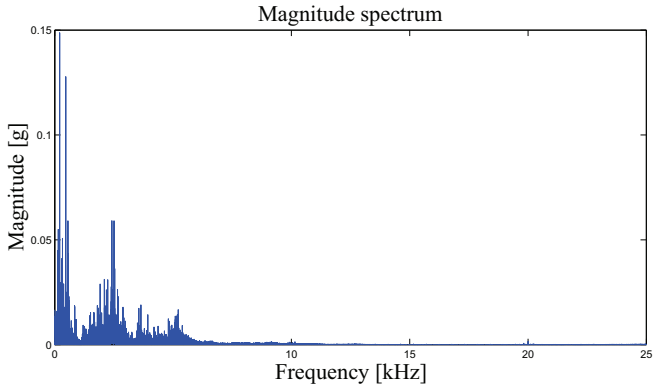

(a)

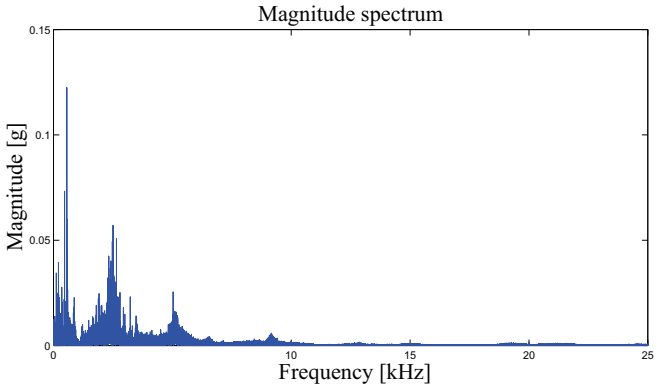

(b)

Figure 2.24: Corresponding magnitude spectrum of signals of fig. 2.23b. (a) without failure (b) with a localized fault in the outer race.

zero components for $\alpha \neq 0$ at the lower frequencies (up to roughly 6 kHz). This components are possibly a result of the periodic components present in the signal (i.e. they are impure second-order cyclostationary). On the other hand, the SCoh of fig. 2.25b shows clear evidence of the fault by revealing discrete components along the α-axis for $\alpha \approx 94$ Hz and harmonics. Moreover, it is noted that this components are continuous along the f-axis within a range of about 15 to 25 kHz.

Finally, the classical envelope is evaluated. The typical procedure consists in filtering the signal in a frequency band that contains the non-stationarities. Then the envelope of the filtered signal is calculated by using, for example, the rectification method or the Hilbert transform. Typically the frequency band for the filter is determined by trial and error, usually around a known resonance zone. The envelope spectrum is highly dependent on the choice of the frequency range of the filter. The filter should be chosen such that no other sources of vibrations present in the signal are contained; otherwise the components at the fault frequency can be masked.

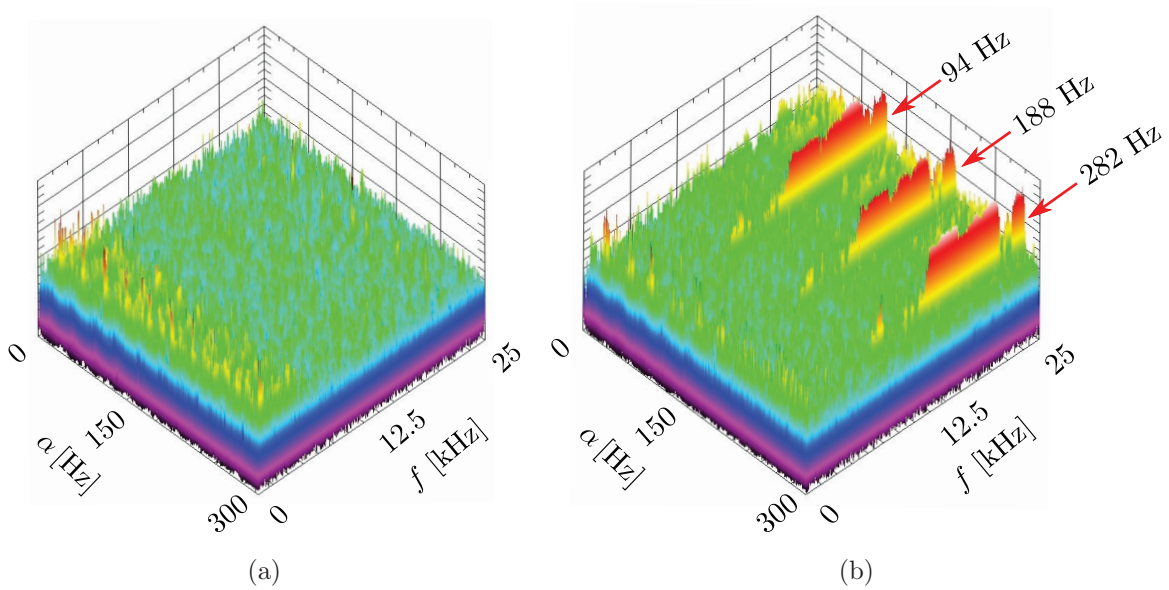

Figure 2.25: Corresponding spectral coherence of the signals of fig. 2.23b. (a) without failure (b) with a localized fault in the outer race.

Fig. 2.26a shows the envelope spectrum calculated from the faulty signal by using no filter. It is clear that such spectrum presents no information about the fault. Fig. 2.26b shows the envelope spectrum calculated by using a high pass filter with cutoff frequency of 6 kHz, which was the filter chosen by the analyst using the typical procedure. The SCoh of fig. 2.25b shows clearly that better results would have been obtained, should a high pass filter with cutoff frequency of 15 kHz had been used. This result is shown in fig. 2.26c. The Scoh of fig. 2.25b also makes clear that the non-zero components at the lower frequencies would mask the components due to the fault if they are included in the calculation of the envelope (as is the case of the envelope shown in fig. 2.26a)

Now the model developed for the AE in a PG is recalled. Eq. (2.41) showed that the random part present in the model of the AE for PG (eq. (2.36)) acts as a low-pass filter of the deterministic part, thus not allowing the recognition of discrete components at the high frequencies. On the other hand, eq. (2.50) showed that the PSD of the stochastic part is a continuous function of f, unable to reveal the hidden periodicities of the signal. Now, the SCD of the stochastic part of the model is calculated. The result is presented in eq. (2.59)

$$
\begin{aligned}
S^{\alpha}_{y_i y_i}(f) &= \frac{1}{T_g^p}\sum_q\sum_k S\left(f+\frac{\alpha}{2}\right)S^*\left(f-\frac{\alpha}{2}\right)\left[b_q^i\Phi_\tau^* - c_q^i\Phi_\tau^*\left(f+\frac{\alpha}{2}\right)\Phi_\tau\left(f-\frac{\alpha}{2}\right)\right]\cdot \\
&\quad e^{-j2\pi q f_C t_1}e^{-j\left(q+\frac{\alpha}{f_C}\right)} \quad \text{, if } \alpha = qf_C + kf_g^p\alpha, \text{ and } \alpha \neq 0 \\
&= \frac{1}{T_g^p}\sum_q\sum_k |S(f)|^2\left[b_0^i - c_0^i|\Phi_\tau(f)|^2\right]e^{-j2\pi q f_C t_1}e^{-jq\psi_i} + P_n(f) \quad \text{, if } \alpha = 0 \\
&= 0 \quad \text{, elsewhere}
\end{aligned}
\tag{2.59}
$$

Eq. (2.59) indicates that the SCD of the stochastic part of the model is a continuous function along the f-axis. It also points out that it presents non zero discrete components along the α-axis only for the cyclic frequencies $\alpha = qf_C + kf_g^p \neq 0$, thus revealing the hidden periodicities of the signal. It is also noted that when $\alpha = 0$, the PSD is obtained (eq. (2.50)). This confirms that the stationary approach is a particular case of the cyclostationary approach, as was indicated in fig. 2.19.

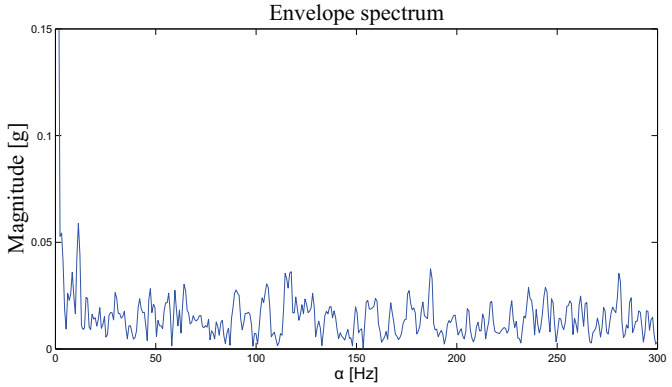

(a)

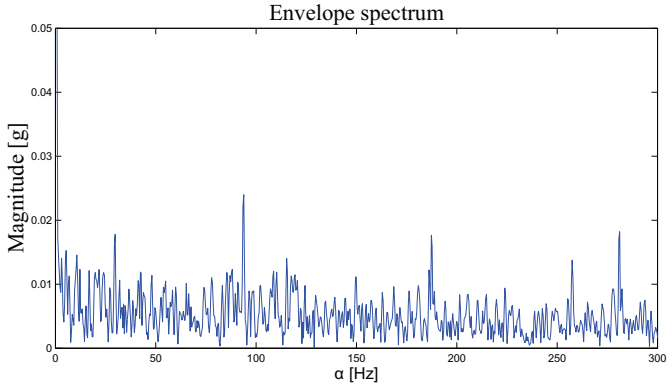

(b)

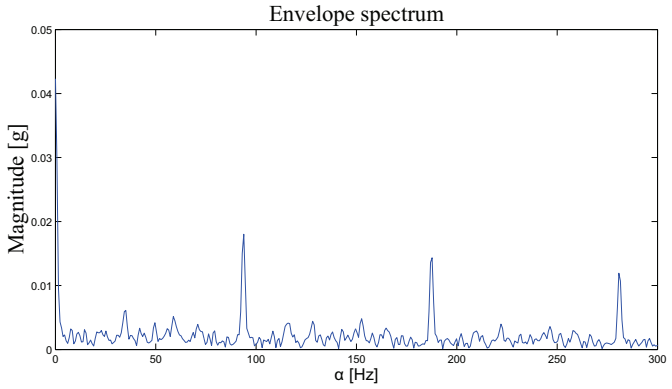

(c)

Figure 2.26: Envelope spectrum of the signal of fig. 2.23b calculated (a) without filter, (b) with high pass filter with cutoff frequency 6 kHz, and (c) with with high pass filter with cutoff frequency 15 kHz.

2.3.5. Summary and comments

It has been shown in this chapter that the AE signals observed when measuring in a planetary gearbox constitute non-stationary signals. When only one planet is considered, such signal is very similar to the vibration signal observed in the case of a bearing with a localized fault. Likewise, the AE generated in a planetary gearbox are dominated by the cyclostationary part of order greater than one; in particular by its second-order cyclostationary part. Additionally, a model for the AE measured in a planetary gearbox was proposed and the assessment of the periodic and stochastic part of the signal was presented. It was shown that the stationary approach would provide no information about the hidden periodicities of the signal. Differently, cyclostationary tools such as the envelope, spectral correlation density, or spectral coherence are tools able to reveal this information.

In addition, in section 2.3.4.7 it was shown that vibration signals from rolling bearings with localized fault exhibit second-order cyclostationary. In chapter 3 it will be shown that the same applies for AE signals. Considering that planetary gearboxes use bearings to allow the rotation of its gear wheels, if one of them presents a localized fault, one could reasonably expect that cyclostationary analysis would provide a way to differentiate the sources from AE and, therefore, to diagnose the fault.

3. Test bench and industrial measurements in planetary gearboxes

3.1. Introduction

Measurements on real mechanical systems consitute a critical part within research projects, which essentially provide the means to prove if the theory developed applies in reality. It is a part that involves different, demanding tasks, and where usually several issues have to be solved. When the results are favorable, this part also represents the natural transition to the industrial application of the methodologies involved, like algorithms, procedures, etc.

Measurements of vibrations and AE were carried out on a planetary gearbox test bench. The signals from the sensors were acquired with a measurement system, which was specially developed to meet the different requirements of the needed measurements. The test bench allowed to perform the measurements under different conditions of load and rotational speed. It was also possible to alter the functioning condition of the PG by seeding defects on its different components. The vibration and AE signals were analysed by using the stationary and cyclostationary approach. Due to the large amount of data available, only selected results are presented for each of the following cases: non-faulty PG, PG with localized defect on the inner race of one planet bearing, and PG with single tooth flank defect on one planet gear wheel.

Industrial measurements of vibrations and AE were also carried out on the PG of different machines working under normal operating conditions. First, the PG of two bucket wheel excavators were measured during a period of approximate one hour each. Then, long term periodic measurements were carried out on the PG of three wind turbines. It was hoped that one of the PG could develop a defect during the measurement campaign, however this has not

been the case till now. Accordingly, all results from the industrial measurements correspond to the non-faulty case. Nevertheless, it must be pointed out, that it were precisely the observations made from the industrial measurement that motivated the development of the AE model, the study of the cyclostationary theory and the implementation of its signal processing tools.

3.2. Measurement system

Experimental tests usually require some special capabilities from the measurement system that are specific to the particular task to be carried out. Usually, no commercial solution is readily available in the market, so that a *tailor-made* measurement system must be somehow developed. In this project the situation was not different. The principal requirements came from the features needed for the acquisition of the AE signals. Additionally, it was required that the system should be able to work in stand-alone operation and perform periodic acquisitions and storage of data from different sensors for long periods of time (several months).

As a solution, a PC-based measurement system was chosen. The advantage of such a system relies in its flexibility. A measurement software (SW) is in charge of controlling the measurement hardware and do the data handling. It is programmed so as to fulfill the requirements of the measurement task. The measurement hardware can be exchanged according to the application. The programming of the SW is actually the most difficult and slow part to carry out, because of the diversity of the activities involved. In this chapter, a brief description of the measurement system developed for the experimental tests is presented.

3.2.1. General description

A measurement system was developed for the simultaneous acquisition, digitalisation and storage of vibration, acoustic emissions and other voltage signals. Fig 3.1 shows a global view of the system used for the measurements in bucket wheel excavators. It consists basically of an industrial computer equipped with the appropriate data acquisition hardware. The specially developed measurement software runs in the computer and properly controls the hardware to acquire the signals provided by the sensors. The software also provides the interface with the user for the configuration of the system (number of channels, sampling rate, type of measurement, etc.). It is also in charge of the storage of the digitised data.

3.2.2. Measurement hardware

Following, the main hardware used in the system is listed together with a brief description. Specific information can be found in the website of the corresponding manufacturer:

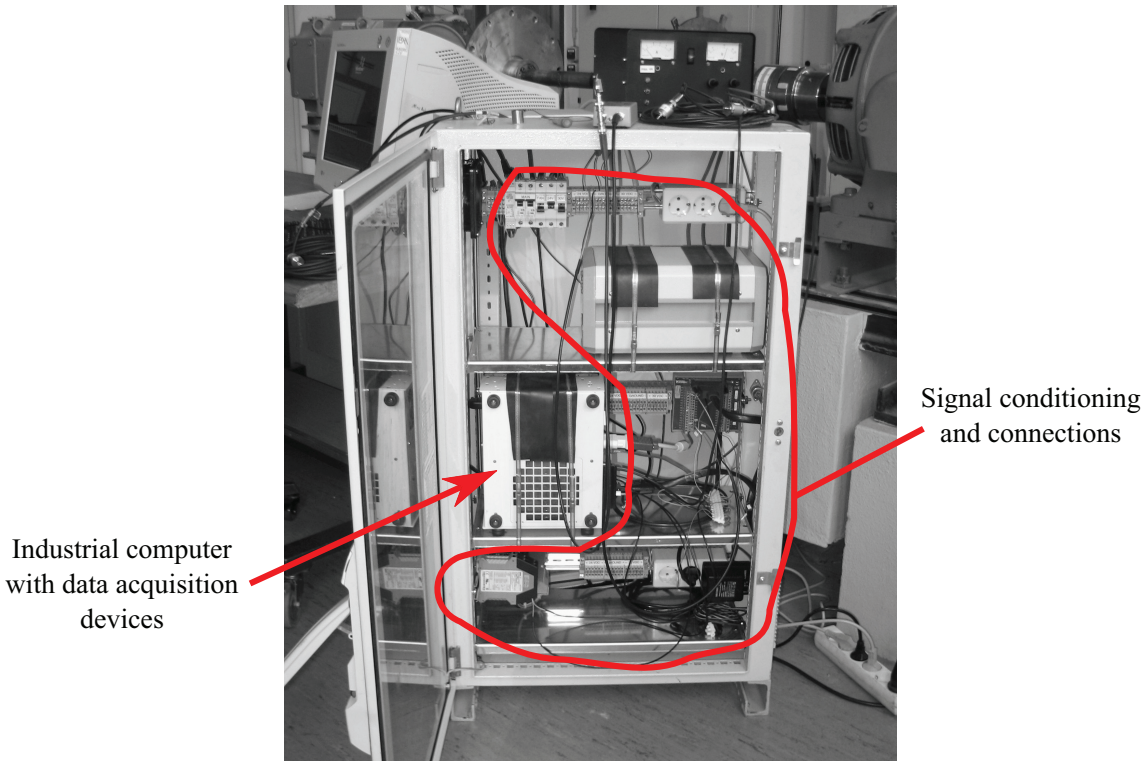

Figure 3.1: Global view of the measurement system.

- Chassis NI PXI-1031: the chassis constitutes the physical structure of the system. The controller and the measurement devices are installed in its slots. The interconnection and synchronization between the devices is possible due to the high speed buses located in the backplane of the chassis.

- Controller NI PXI-8105: is actually a PC embedded into a compact unit designed to meet industry standards. The PXI 8105 used contains a 2.0 GHz Intel Core Duo T2500 processor running windows XP, 2 GB RAM and 500 GB HDD.

- Data acquisition device NI PXI-4472b: this device is specially designed for the acquisition of accelerometer signals. It has a programmable high-pass filter with cutoff frequency of 0.5 Hz for removal of the DC component, programmable power supply (integrated electronic piezoelectric, IEPE), 24 bit resolution and simultaneous sampling of eight channels with maximum sampling rate of 102.4 kS/s.

- Data acquisition device NI PXI-6132: this device is designed for high sampling rate acquisitions. Hence, it was selected for the measurement of the AE signals. The main

features of the device are: 14 bit resolution and simultaneous sampling of four channels with maximum sampling rate of 2.5 MHz (3 MHz for single channel measurement).

- Data acquisition device NI PXI-6251: this multifunction device was selected for the acquisition of voltage signals from tachometers, temperature probes, etc. The main features of the device are: 16 bit resolution and multiplexed acquisition of 16 channels with maximum aggregate sampling rate of 1 MHz (1.25 MHz for single channel measurement).

- Accelerometer sensors FAG 602M36/M010BZ (frequency range (±3 dB): 0.5 Hz−10 kHz), Tebüco LN-02 (frequency range (±3 dB): 4 Hz − 25 kHz) and PCB Piezotronics (frequency range (±3 dB): 0.2 Hz − 20 kHz).

- Acoustic emissions sensor Kistler 8152B211 with coupler Kistler 5125B1: Broadband AE sensor with frequency range between 100 kHz and 900 kHz (±10 dB).

- Photoelectric sensor Banner Mini-Beam: used as a one pulse-per-revolution tachometer by pointing to a reflective adhesive band glued on the shaft.

- PT100 temperature probe and signal converter Phoenix contacts Pt100 MINI MCR: used for measurement of reference temperature of the lubricant of the gearbox.

3.2.3. Developed measurement software

The measurement SW was entirely programmed for the application in the programming suite LabVIEW 8.6. The SW permits the acquisition of data in two modes: *single-shot continuous acquisition* and *automated periodic acquisition*. In the first mode, the measurement starts and stops when the corresponding buttons are clicked. In the second mode, the system will permanently perform periodic measurements of a configurable length till the stop button is clicked. The interval between successive measurements is configurable as well. Fig 3.2a shows the section of the configuration panel where the measurement mode selection is done. Here the user defines whether to perform an automated periodic, or a single-shot measurement. The parameters “Acquire [Blocks]”, “every...”and “Reference timestamp”define how the periodic measurement will be performed. The parameter “Verification value (greater than or equal to...) [signal units]”defines a threshold for the mean value of some verification signal, so that

each periodic measurement will be stored only if the mean value of the verification signal exceeds the defined threshold. For example, the configuration shown in figure 3.2a will result in a measurement of length 600 *blocks* that will be performed each 60 minutes starting at 11:00:00 of 06/02/2009, if the mean value of the verification signal exceeds the value of 1.5 [signal units].

During the measurement, the acquisition of each channel is done in successive blocks of data. Each block consists of a given number of samples and represents a given amount of time. For example, if the block size is configured to 50000 and the sampling rate is 100 kHz, then the block will have a length of 50000/100000 = 0.5 seconds. Fig. 3.2b shows the configuration panel of the 4472b device. Here the parameters "Rate"and "Samples/Block 4472b"are equal, so that each block has a time length of one second. It is important to keep the time length of the blocks equal for the three measurement devices. Fig. 3.2b also shows how the configuration of the channels is performed. The column "Include?"specifies which channels must be included in the measurement; the column "ICP?"specifies which channels must be power-supplied from the system (IEPE); the column "DC?"specifies for which channels the DC component must be included; the column "Verif. Signal"specifies which channel must be considered as a verification signal for the periodic measurement. If none is selected, then the verification prior each measurement is ignored and all periodic measurements will take place.

Once the configuration is ready, the measurement task is started by clicking the button "Start Measurement". According to the measurement mode that has been selected, a new measurement window comes into sight. Fig. 3.3 shows the window corresponding to the periodic measurement mode. The clock indicates how much time is left for the next measurement to start. The round light indicators in the middle section turn on when a block of data is being written to the hard disc, and turn off when the storage is ready. It is important that the write-to-disk task of the data takes shorter than the length of the block defined in the configuration of the devices. In practice, this means that it is important to see the round light indicators blinking. If not, this would mean that the write tasks take longer than the time it takes for new data to be acquired, so that some data will start to accumulate in the buffers. During the measurement, the state of the buffer for each measurement device is indicated by the horizontal bars at the left of the round light indicators. The size of the buffer is defined by the controls grouped under "Buffers"in the configuration panel (fig. 3.2a). Eventually, if the acquisition is long enough, the buffers can reach its maximum capacity, which would lead to the loss of

(a)

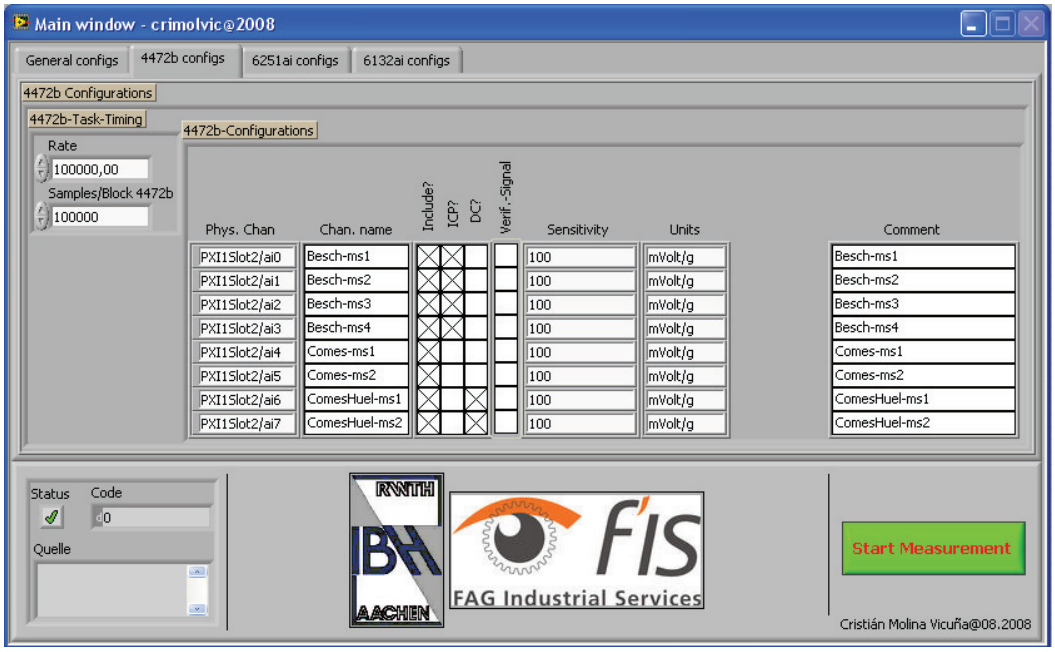

(b)

Figure 3.2: Configuration panel of the measurement SW. (a) Configuration of buffers and measurement mode, and (b) configuration of data acquisition device.

continuity of the acquired data. In this case, the program will return an error message and will stop. Since the writing speeds of the system can vary depending on parameters such as sampling rates, type of hard disk, processor charge, temperature, etc., some tests should be

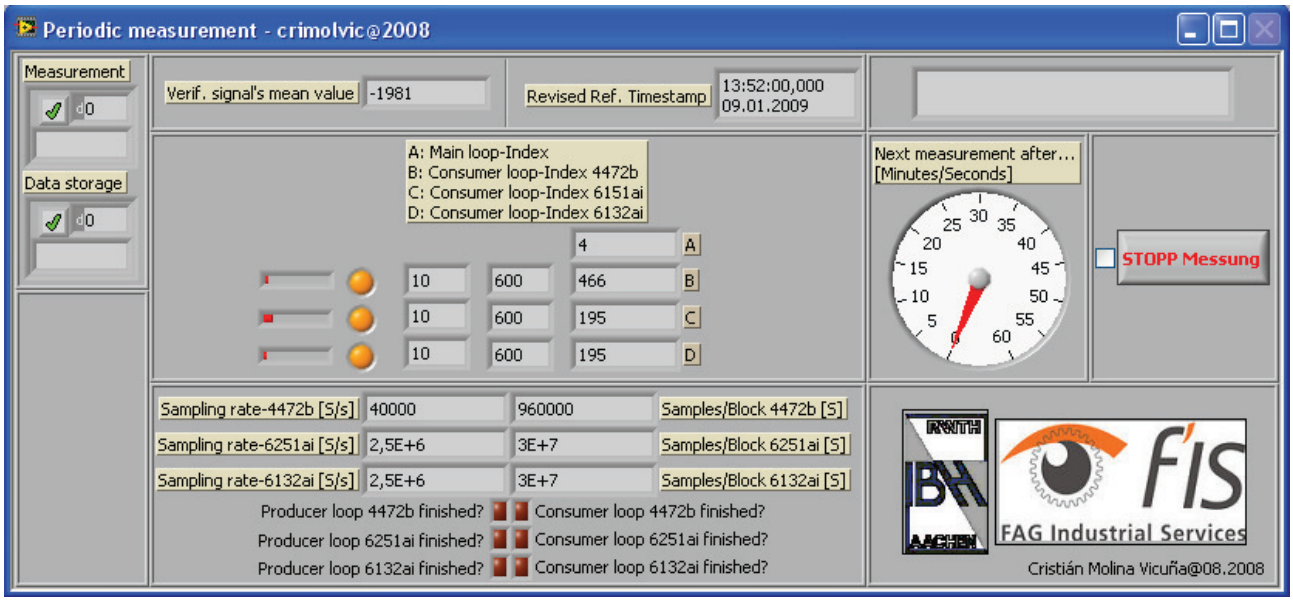

Figure 3.3: Periodic measurement window.

Figure 3.4: Structure of the stored data.

made previous to the measurement, in order to determine an appropriate block length. In this thesis, a block length of 1 second was used for all measurements.

A succesful measurement produces a set of files containing the data as a result. They are stored within a folder called after the date and time at the beginning of the measurement (e.g. 20080812-144446). This folder has the structure shown in fig. 3.4. The folders "4472b", "6231ai"and "6251ai"contain the actual measured data in raw format, in form of binary files[1]. The file "*_Config.txt"stores the configuration used for the measurement; the three remaining files store the scalling coefficients needed when reading the data from the raw binary files, to obtain the actual values of the signal in Volts (or g in the case of accelerometer data).

[1]Following data types were used for the storage of the measured data in the binary files: I16 for data from the devices 6132 and 6251; I32 for the device 4472b

Due to the high sampling rate capabilities of the system, large amount of data –in form of files– can be generated. For example, when measuring signals from 8 accelerometer sensors at 100 kHz, 2 AE sensors at 2.5 MHz and 4 voltage signals at 250 kHz, the system would generate a data flow of $(8 \times 1 \cdot 10^5 \times 32 + 2 \times 2.5 \cdot 10^6 \times 16 + 4 \times 2.5 \cdot 10^5 \times 16)/8 = 15.2$ MB/s. This point should be considered when dealing with long measurements.

3.3. Measurements on the planetary gearbox test bench

3.3.1. Description of the test bench and planetary gearbox

The test bench used consists basically of an asynchronous motor (22 kW) connected to the sun gear of the planetary gearbox (PG) through a flexible coupling; the output of the PG –i.e. the carrier plate– is connected to a DC generator also through a flexible coupling. The PG has three planet gears positioned at $\psi_i = 0;\ 2\pi/3$ and $4\pi/3$, which are mounted on needle bearings INA NK17/20. The number of teeth of the wheel gears is $Z_S = 18$, $Z_P = 26$ and $Z_R = 72$. More information about the PG is given in appendix A. The motor and the generator are controlled through frequency converters, so that the speed and load are adjustable. Fig. 3.5 shows a picture of the test bench together with the measurement equipment. Fig. 3.6 shows a detailed view of the mounting of the acceleromenter and AE sensor. As noted in this figure, a flat surface was milled to ensure the proper mounting of the sensors.

Phase analysis of the gear meshing processes

Following, the phases of the gear meshing processes involved in the PG are scrutinized. Referring to eq. (2.1), the phase difference between the planet-ring gear meshing processes is given by:

$$\{\gamma_{ri}\} = \frac{\{\psi_i\}}{\angle_R} = \frac{\{\psi_i\}\, Z_R}{2\pi} = \left\{ \frac{(0)\,72}{2\pi};\ \frac{(2\pi/3)\,72}{2\pi};\ \frac{(4\pi/3)\,72}{2\pi} \right\} = \{0;\ 24;\ 48\} \tag{3.1}$$

All $\gamma_{ri}|_{i=1,\,2,\,3}$ are integer, which means that all planet-ring gear meshing processes are in-phase. Thus, according to the classification given in section 2.2.3, the PG pertains to the group (A) (i.e. PG with equally spaced planet gears and in-phase planet-ring gear meshes).

Now, the phase differences between the meshing processes of the planet gears with the sun gear are evaluated by using eq. (2.20):

$$\{\gamma_{si}\} = \frac{\{\psi_i\}}{\angle_S} = \frac{\{\psi_i\}\, Z_S}{2\pi} = \left\{ \frac{(0)\,18}{2\pi};\ \frac{(2\pi/3)\,18}{2\pi};\ \frac{(4\pi/3)\,18}{2\pi} \right\} = \{0;\ 6;\ 12\} \tag{3.2}$$

Like in the previous case, all $\gamma_{si}|_{i=1,\,2,\,3}$ are integer, which means the sun-planet gear meshing processes are also in-phase. Finally, since the PG pertains to the group (A) and $Z_P = 26$ is

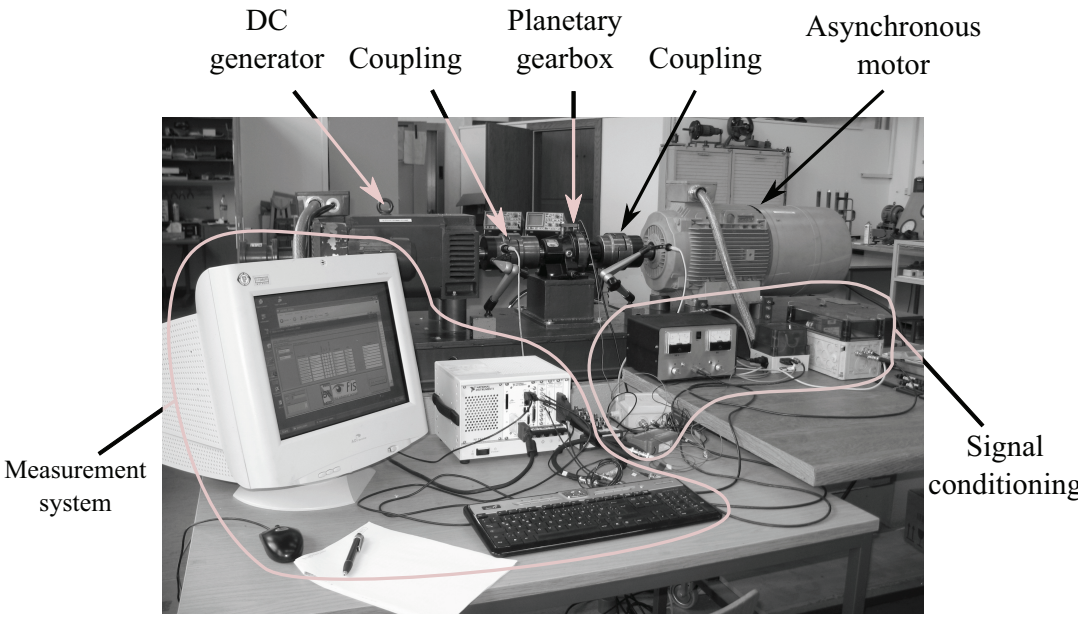

Figure 3.5: General view of the test bench and measurement equipment.

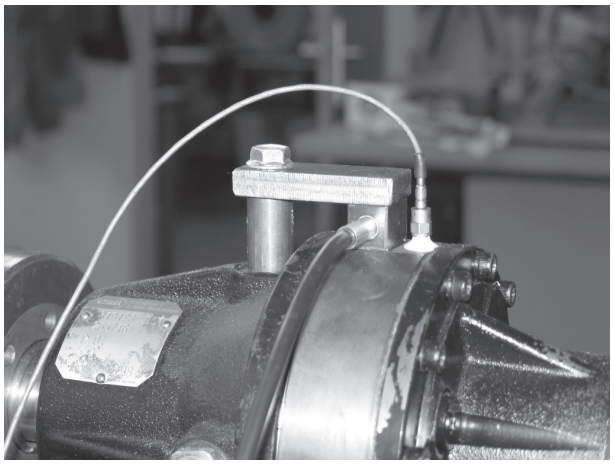

Figure 3.6: Sensor mounting; left: AE sensor, right: accelerometer.

even, the phase difference between the planet-ring gear meshing processes and the sun-planet gear meshing processes is $\gamma_{sr} = 0$. Hence, it is concluded that all gear meshing processes taking place in this particular PG are in-phase.

3.3.2. Measurements and results

Several measurements were undertaken under different fault conditions of the PG: non-faulty, planet gear fault and planet bearing fault (inner ring). For each fault condition, measurements under different levels of load and speed were performed. As expected, the measurement campaign produced a large amount of data; for reasons of space, only selected results are presented.

3.3.2.1. Non-faulty gearbox

First the non-faulty case is presented. The rotational speed of the motor is 1800 rpm and the load is 65 Nm. The gear mesh frequency can be calculated using eq. (1.7a): $f_g^p = \frac{Z_S Z_R}{Z_S+Z_R} |f_S| = \frac{18\times72}{18+72}\left(\frac{1800}{60}\right) = 432$ Hz. Fig. 3.7 shows the magnitude spectrum of the signal measured by the accelerometer around the components at the gear mesh frequency and its first harmonic. In accordance with the model presented in chapter 2.2, components at f_g^p and multiples with sidebands spaced at $3 \times f_C$ are recognized. Some sidebands spaced at f_C are also present, specially around f_g^p (fig. 3.7a). Their presence can be due to differences in the shape between the vibrations generated in the meshing processes of each planet. Fig. 3.8 shows the spectrum of the AE signal which, as explained in chapter 2.3, is a broadband spectrum unable to reveal the hidden periodicities of the signal. Fig. 3.9 shows the spectral coherence caculated for the AE signal, where discrete components along the α-axis are clearly recognized for α_g^p and $2 \times \alpha_g^p$, thus revealing the hidden periodicity of the signal. This figure also shows that the second order cyclostationarity is exhibited in the frequency range above $f \approx 100$ kHz. Based on this, the envelope spectrum of the AE signal was calculated by previously filtering the AE signal with a high pass filter with cutoff frequency of 100 kHz. This is shown in fig. 3.10, where discrete components at α_g^p with some sidebands spaced at α_C are evidenced. Note that the sidebands are also recognized in the spectral coherences of fig. 3.9, although not that clear due to its coarser resolution.

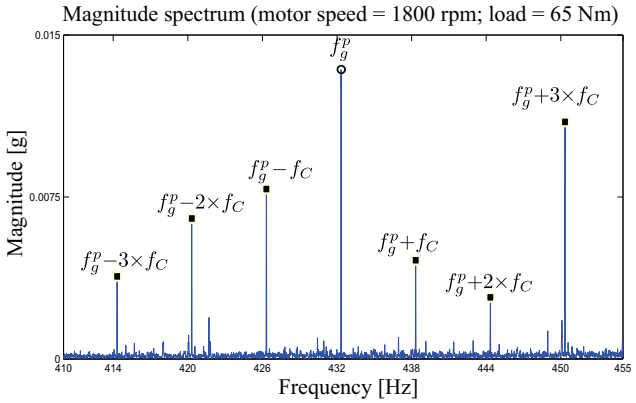

(a)

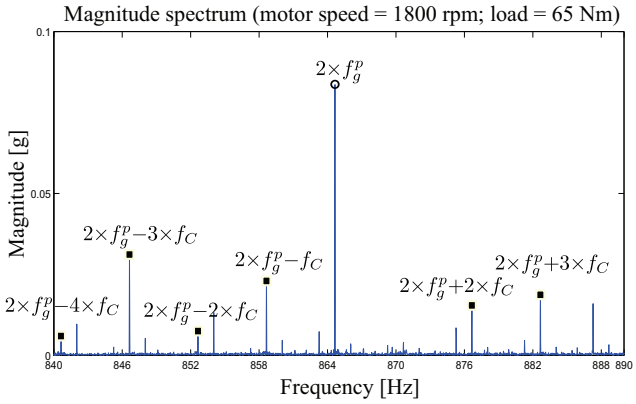

(b)

Figure 3.7: Spectrum of the acceleration signal. (a) Portion around the gear mesh frequency $f_g^p = 432$ Hz, and (b) portion around $2 \times f_g^p$.

3.3.2.2. Localized planet bearing defect

Subsequently, the PG was disassembled and a localized inner ring fault was seeded in the bearing of one planet gear wheel by using an electrical engraving machine. The process is illustrated in fig. 3.11. The result was a very light fault, despite somewhat heavier look observed in the picture. Afterwards, the faulty inner ring was mounted on the PG and the set of measurements was repeated. The results presented in the next lines correspond to a measurement taken with the motor turning at 1200 rpm and a load of 65 Nm. The fault frequency factor (BPFI[2]) was calculated for the geometry of the bearing by using the well known formulae [How94]. This gave the result BPFI ≈ 8.05. Hence, the fault frequency is given by $_{\text{fault}_\text{b}} = \text{BPFI} \times f_{B_7}$, where f_{B_7} is as given in eq. (1.5g). Considering the rotational speed of the motor, $f_{\text{fault}_\text{b}} \approx 89.2$ Hz.

[2]BPFI: ball pass frequency of the inner race. For calculation details, see appendix A

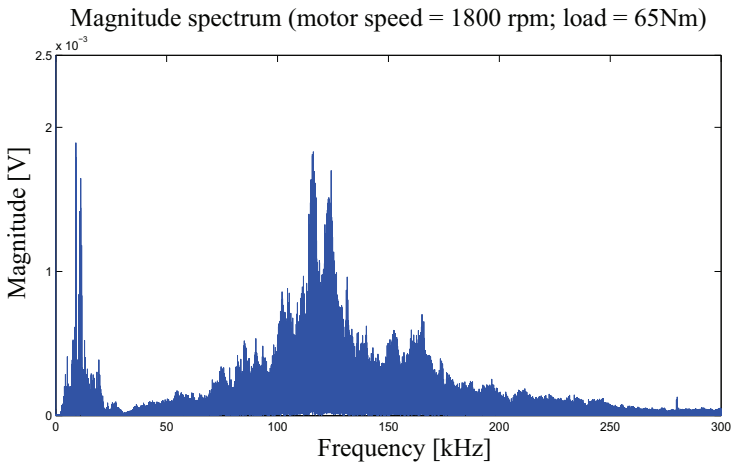

Figure 3.8: Spectrum of the AE signal.

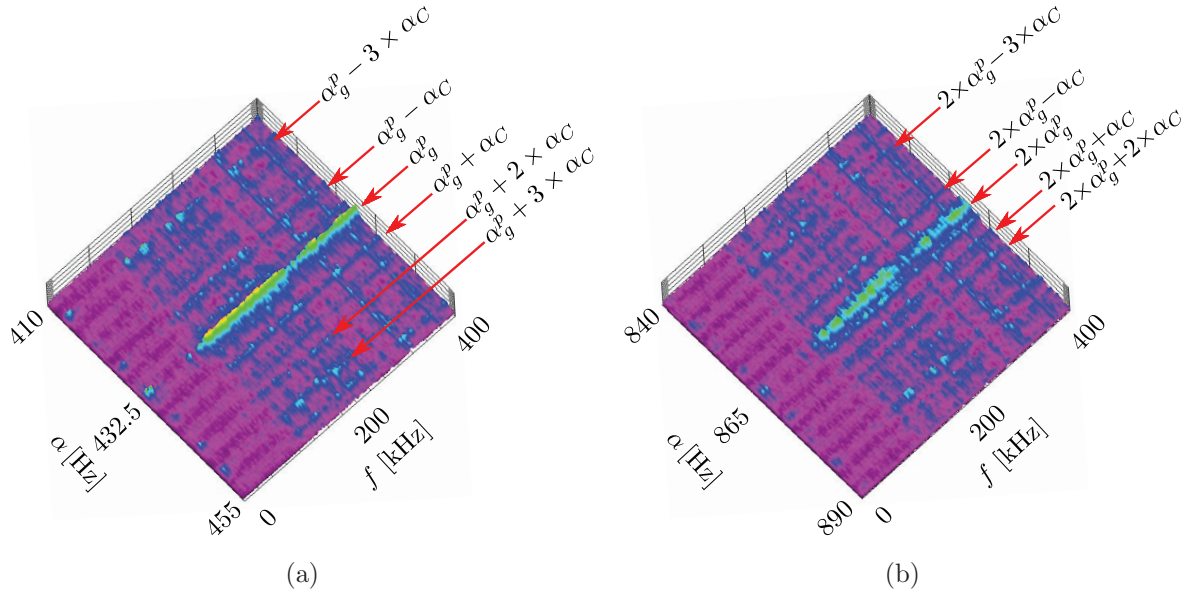

Figure 3.9: Spectral coherence of the AE signal. (a) Portion around the gear mesh frequency $\alpha_g^p = 432$ Hz, and (b) portion around $2 \times \alpha_g^p$.

Fig. 3.12a shows the spectral coherence of the AE signal, where a discrete component at the fault cyclic frequency $\alpha_{\text{fault}_\text{b}}$ with sidebands at 4 Hz are clearly observed. The distance of the sidebands coincides with the rotational cyclic frequency of the carrier plate α_C. The pattern of the discrete components observed along the α-axis is a clear indicator of the fault. The fault produces a series of bursts in the AE signal, which would be seen with constant amplitude by an observer standing and rotating with the carrier plate[3]. Differently, the sensor experiences the

[3]In the conventional case, the inner ring rotates with respect to the resultant force acting on the bearing. This produces an amplitude modulation of the bursts generated when a rolling element rolls over the damaged

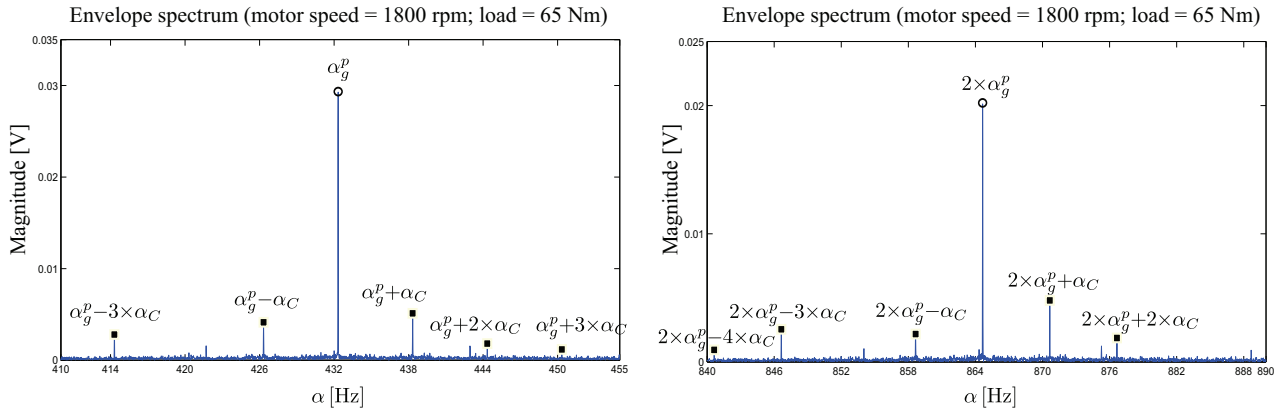

Figure 3.10: Envelope spectrum of the AE signal. (a) Portion around the gear mesh frequency $\alpha_g^p = 432$ Hz, and (b) portion around $2 \times \alpha_g^p$.

Figure 3.11: Localized inner ring defect being seeded.

same series of bursts but with an amplitude modulation due to the periodic revolving motion of the planets around the sun gear, which has a fundamental cyclic frequency equal to α_C. The spectral coherence also shows that the fault is best observed in the frequency range between $f \approx 100$ kHz and $f \approx 220$ kHz. Accordingly, the envelope of the filtered version of the signal within this frequency range was calculated and is presented in fig. 3.13a. As expected, the

zone, as the fault periodically enters and leaves the loaded zone. Contrary, in planet bearings is the outer ring that rotates with respect to the resultant force acting on the bearing. There is no rotation of the inner ring with respect to the resultant force acting on the bearing. Therefore, under the presence of a localized inner ring defect, no amplitude modulation at the relative rotational frequency of the inner and outer ring occurs.

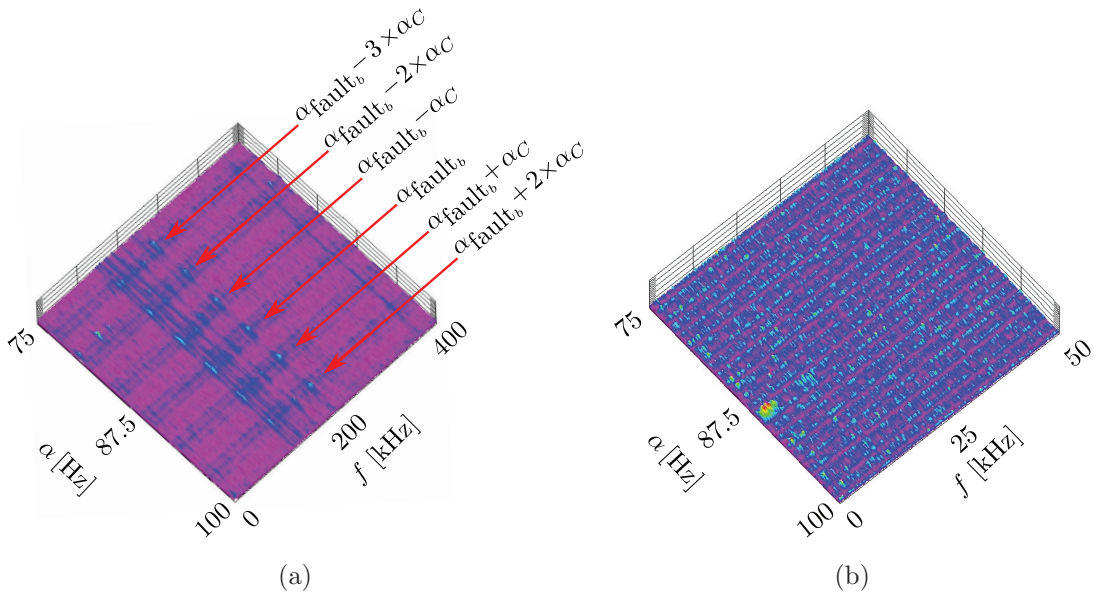

Figure 3.12: Spectral coherence for the signals measured with localized inner ring fault. (a) Of the AE signal, and (b) of the acceleration signal.

envelope spectrum also reveals the fault.

Fig. 3.12b shows the spectral coherence of the acceleration signal. Contrary to the spectral coherence of the AE signal, no signs of the fault are found. Correspondingly, the envelope of the acceleration signal does not present discrete components at the fault cyclic frequency (see fig. 3.13b).

3.3.2.3. Single tooth flank defect of planet gear wheel

The gearbox was again stopped, the faulty planet bearing was replaced by a non-faulty and a fault was seeded on the surface of one planet gear's tooth flank. Fig. 3.14 shows the seeded defect, which was accomplished with the electrical engraving machine. The defect produced can be described as roughness spread over the complete tooth flank; it is essentially a surface defect. Since the planet gears meshes with both, the ring and sun gear with opposite tooth flanks, the fault will mesh with the ring gear or with the sun gear depending on the rotational direction of the input shaft. However, in both cases, the frequency with which the faulty tooth flank comes in contact with either a ring tooth flank, or a sun tooth flank is the same and its given by the relative rotational frequency of the planet gear with respect to the carrier plate,

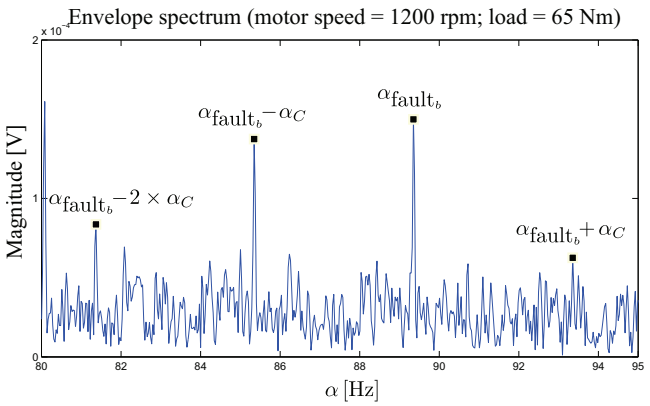

(a)

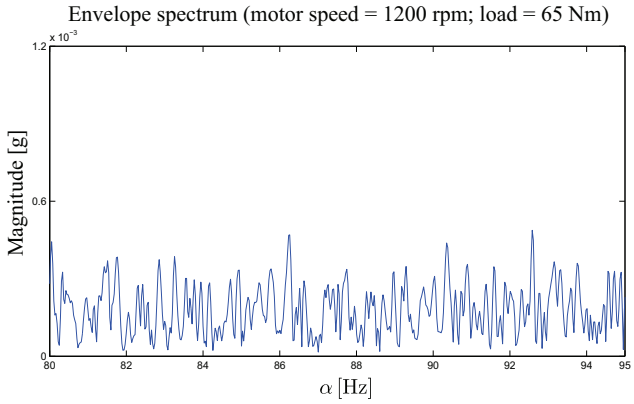

(b)

Figure 3.13: Envelope spectrum for the signals measured with localized inner ring fault. (a) Of the AE signal (band pass filter between 100 kHz and 220 kHz, and (b) of the acceleration signal (high pass filter with cutoff frequency 30 kHz).

which is calculated as follows:

$$f_{\text{fault}_\text{g}} = f_{P|C} = |f_P| + |f_C| = \frac{Z_S Z_R}{Z_P\,(Z_S + Z_R)} f_S \tag{3.3}$$

The results presented next correspond to a measurement taken with the motor turning at 1800 rpm and a load of 65 Nm. For this motor speed, the fault frequency is $f_{\text{fault}_\text{g}} = 16.62$ Hz. Fig. 3.15a shows the spectral coherence of the AE signal around the first gear mesh component. It is possible to recognize discrete components along the α-axis for the gear mesh cyclic frequency with sidebands spaced at $\alpha = 6$ Hz. Although not so clear in the figure, one pair of sidebands spaced at $\alpha = 16.62$ is also present. This modulation is indicative of the seeded defect, and is clearer in the envelope spectrum of the AE, which was calculated from the filtered version of the AE signal in the frequency range between 80 kHz – 300 kHz, and is presented in fig. 3.16a.

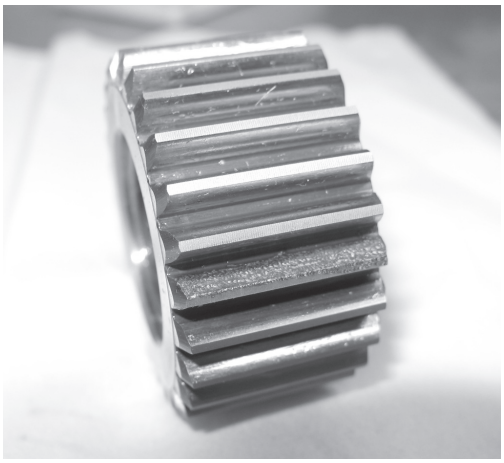

Figure 3.14: Localized planet gear single flank tooth defect.

Subsequently, the spectral coherence was calculated for the acceleration signal, and is presented in fig. 3.15b. As observed, only discrete componets along the α-axis are observed in the low frequencies (up to $f \approx 25$ kHz) and are probably impure second-order cyclostationary. No evident sign of the fault is found in this case. Finally, the envelope spectrum of the high-pass filtered acceleration signal (cutoff frequency of 30 kHz) was calculated, see fig. 3.16b. Here only one sideband is observable, thus providing no clear evidence of the fault.

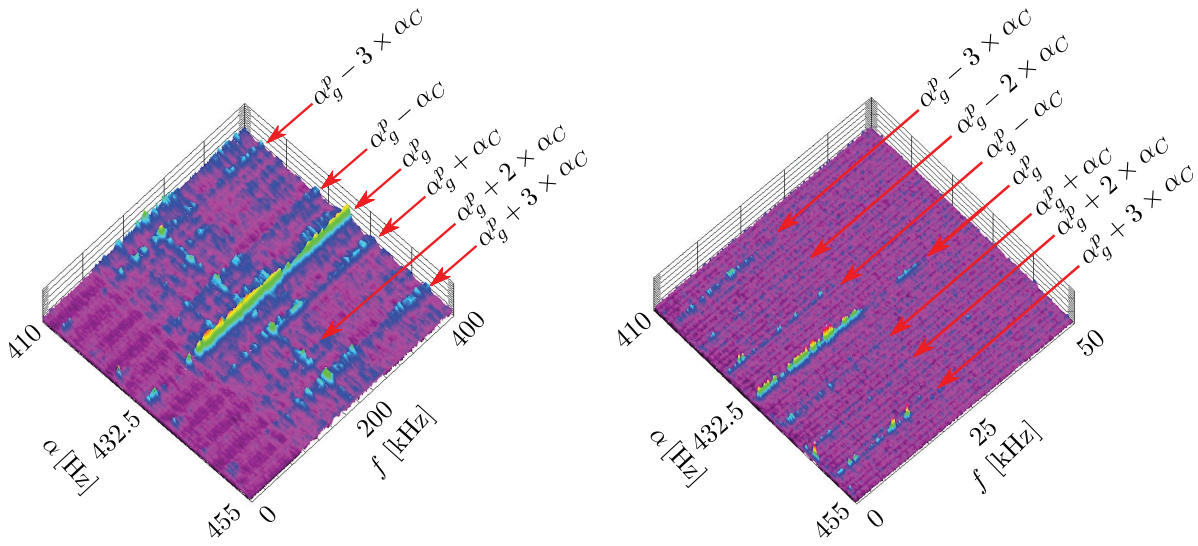

(a) (b)

Figure 3.15: Spectral coherence of the signals measured with planet gear's single tooth flank defect. (a) Of the AE signal, and (b) of the acceleration signal.

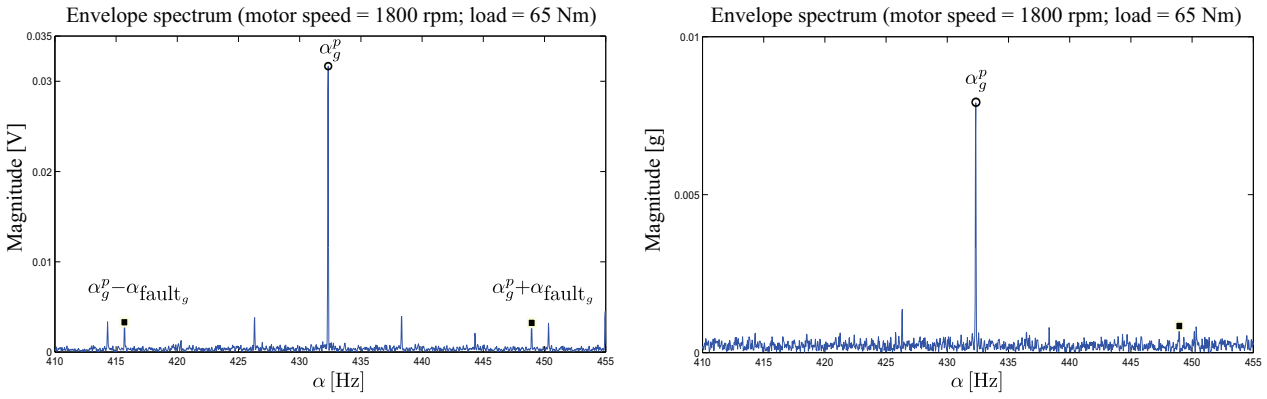

(a) (b)

Figure 3.16: Envelope spectrum of the signals measured with planet gear's single tooth flank defect. (a) Of the AE signal (band pass filter between 80 kHz and 300 kHz, and (b) of the acceleration signal (high pass filter with cutoff frequency 30 kHz).

3.4. Industrial measurements

Measurements were undertaken on the planetary gearbox of two bucket wheel excavators (BWE) used in open-pit lignite mining, and on the planetary gearbox of three wind turbines (WT). In all cases, the condition of the gearboxes under measurement was unknown. In the case of the BWE, only one measurement –for approximate one hour– on each gearbox was possible. In the case of the WT, daily periodic measurements were taken for several months. The data analysed till date has shown no evident sign of any fault. At the date this thesis was ended, measured data from the WT was still being provided and analysed.

Even though no sign of fault was observed, the data provided rich information, which allowed the examination of the signals' behaviour on real conditions. The industrial measurements also included the challenge of the analysis of AE signals on machines whose operation included constant variations of load and speed.

As it can be imagined, the measurement campaigns originated an extremely large amount of data, which led to a similar amount of results. In the following sections, a brief description of the measurement objects and the type of measurements is given, and only selected results are presented.

3.4.1. Measurements on the planetary gearbox of bucket wheel excavators

Vibrations and acoustic emissions were measured in the planetary gearbox of two BWE in two lignite open pit mines in Germany. Both BWE are identical in construction. Two PG are connected in series and constitute the last reduction stages in the drive system of the bucket wheel. Fig. 3.17 shows a general view of the BWE. Fig 3.18a shows the technical drawing of the gearbox. The sensors were installed on the outer part of the ring gear of the second planetary stage, as marked in fig. 3.18a and shown in fig 3.18b.

The measurement system was installed at a distance of about 20 m from the PG, and it was controlled wireless from the operator's room. Several measurements were conducted during a period of approximate one hour on each BWE. All data was stored locally on the hard drive of the measurement system. Once the system was dismounted, the data was retrieved for

Figure 3.17: General view of the BWE.

processing and analysis at the University.

3.4.1.1. Description of the object under measurement

As shown in fig. 3.18a, the gearbox of the drive system of the bucket wheel consist first of a fixed-shaft straight bevel reduction stage, followed by two fixed-shaft spur gear stages. The output of the latter is connected to the sun gear of the first planetary stage. The carrier plate of the first planetary stage is connected to the sun gear of the second planetary stage. Finally, the carrier plate of the second planetary stage is connected to the bucket wheel. The total reduction ratio of the gearbox is 349.7 : 1. The nominal rotational speed of the motor is 990 rpm, by which the bucket wheel completes 2.83 revolutions in one minute.

Both planetary stages have three equally spaced planets gears. All gear wheels from both planetary stages are spur gears. The number of teeth of the gear wheels of the first planetary stage are $Z_{S_1} = 21$, $Z_{P_1} = 64$ and $Z_{R_1} = 150$. The number of teeth of the gear wheels of the second planetary stage are $Z_{S_2} = 27$, $Z_{P_2} = 31$ and $Z_{R_2} = 90$ (more information about the planetary stages is provided in appendix B). It can be demonstrated that both stages pertain to the group (A) (PG with equally spaced planets and in-phase planet-ring meshes). It can also be shown that all meshing processes involved in the first stage are in-phase; whereas in the second

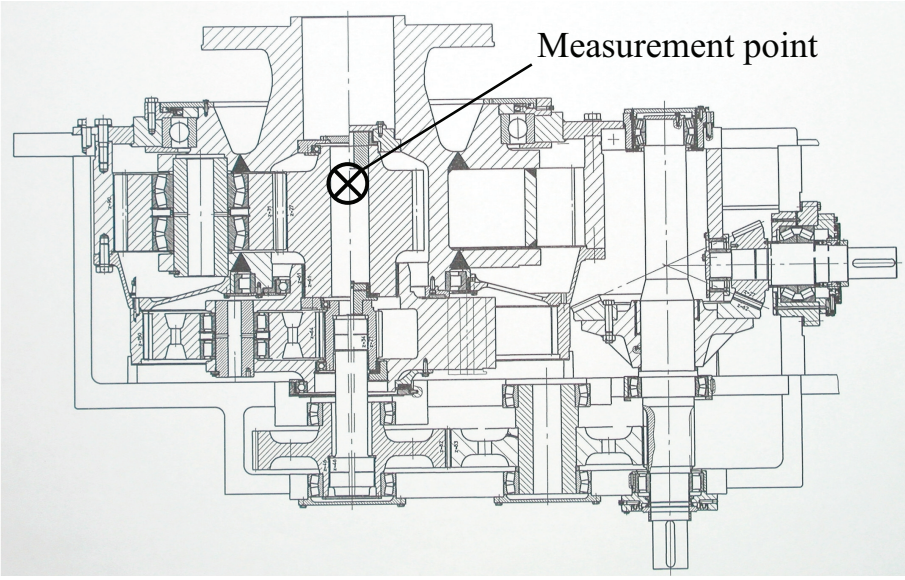

(a)

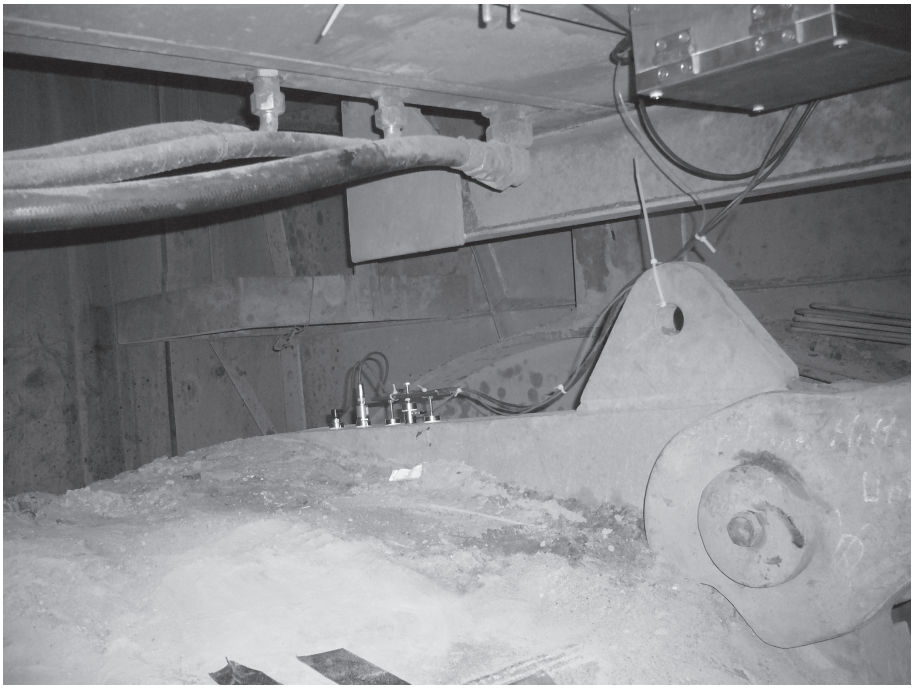

(b)

Figure 3.18: (a) Technical drawing of the gearbox. (b) AE and acceleration sensor mounted on the PG.

stage, all planet-ring meshing processes are in-phase, all planet-sun meshing processes are in phase, but there is a phase difference between the planet-ring mesh processes and planet-sun mesh processes (i.e. $\gamma_{rs} \neq 0$).

3.4.1.2. Operating conditions

The BWE is used to reclaim the overburden which contains the lignite. As the bucket wheel rotates, each bucket digs in the overburden, gets full of earth and transfers it into a conveyor belt when it reaches the uppermost position. The process is done repetitively by each bucket in the bucket wheel. Evidently, the forces involved in such a digging process are variable, so that the load acting on the gearbox is variable as well. Furthermore, this variable load produces variability in the rotational speed of the complete drive. Accordingly, the analysis was done in the angular domain. Unfortunately, only a voltage signal representative of the rotational speed of the sun gear of the first planetary stage was available for this task. Such signal is not the ideal for the conversion of the signals from the time domain to the angle domain, since some noise will be introduced into the signal in the process. However, the result is considerably superior than the obtained when working directly with the signals in time domain.

3.4.1.3. Results

A high amplitude modulation was observed in the AE signals already during the measurements. Fig. 3.19a illustrates this by showing a portion of the AE signal after angular resampling. It was found that the amplitude modulation of the AE is caused by the load variation due to the bucketing process, thus revealing the existence of an influence of the load on the AE generated on the gear meshing processes of the gearbox. Fig. 3.19b shows a joint plot of the envelope of the AE and the inverted rotational frequency of the sun gear of the first planetary stage. This figure illustrate the influence of the load on the AE. The inverted rotational frequency (i.e. multiplied by minus one) is used as a rough estimation of the load variability.

Fig. 3.20a shows a portion of the spectral coherence of the AE signal around the gear mesh component of the first planetary stage. A discrete component along the α-axis is observed for the gear mesh cyclic order of the first planetary stage $\alpha^p_{g_1}$. Some sidebands around this component spaced at three times the carrier plate cyclic order of the first planetary stage (α_{C_1})

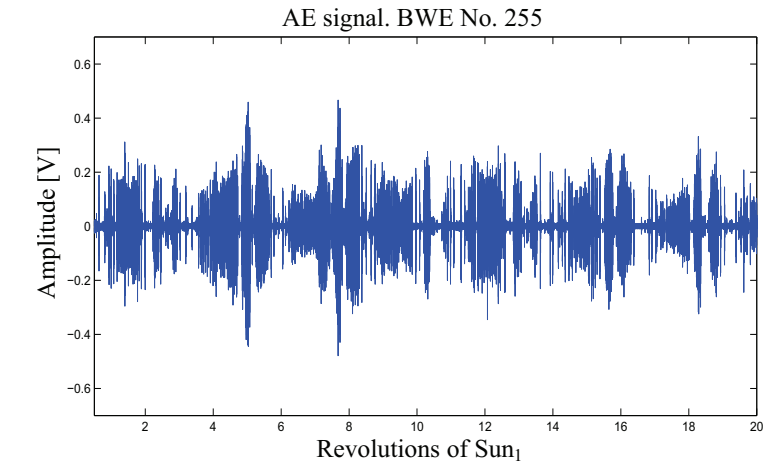

(a)

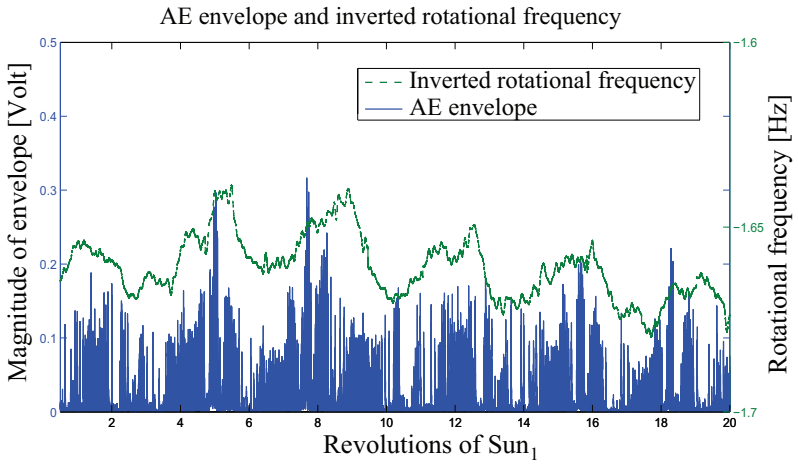

(b)

Figure 3.19: (a) AE signal in angle domain. (b) Envelope of AE and inverted rotational frequency of the sun gear of the first planetary stage.

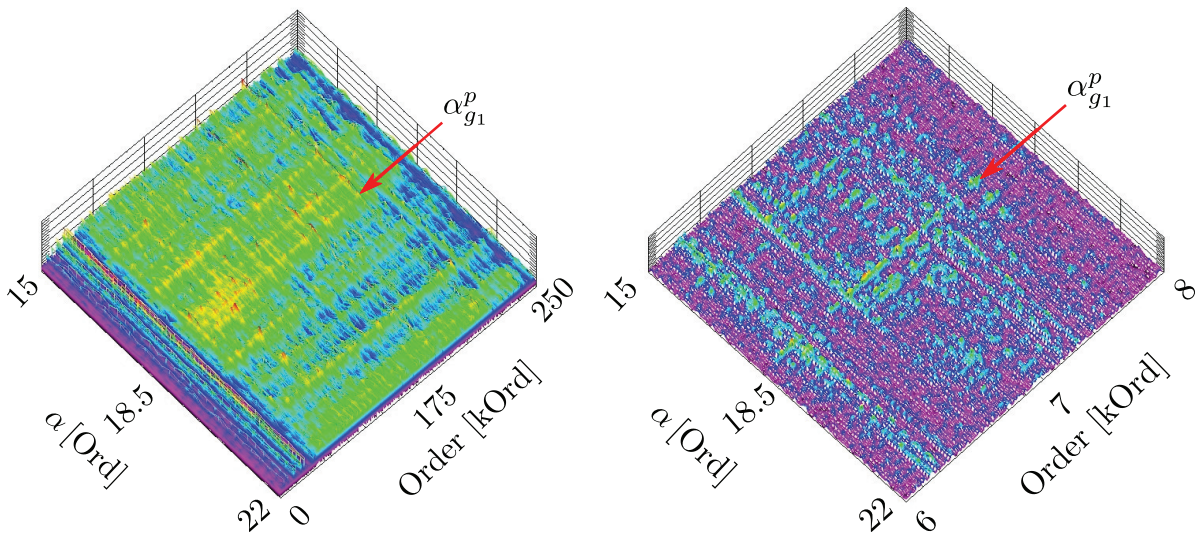

Figure 3.20: Spectral coherence of the signals after angular resampling (a) of the AE signal, and (b) of the acceleration signal.

are barely recognized. They should become clearer by improving the cyclic frequency resolution $\Delta\alpha$; however, this was not possible due to restriction on the computational resources. The spectral coherence also shows that the optimum envelope spectrum is obtained when previously filtering the AE signal in angle domain with a high pass filter with cutoff frequency of ≈ 50 kOrd. In the frequency domain, this is equivalent to a high pass filter with cutoff frequency of ≈ 80 kHz. Hence, the envelope was first calculated from the filtered AE signal in time domain. Then, the envelope was angular resampled. Finally, the magnitude spectrum was calculated from the angular resampled envelope of the AE. The portion around the gear mesh component of the first planetary stage is presented in fig. 3.21a. Since the computational demands needed for the processing of the envelope are lower than the demands for the processing of the spectral coherence, it is possible to handle a longer AE signal. As a consequence, an improved cyclic order resolution is achieved, which allows to clearly distinguish the sidebands at $3 \times \alpha_{C_1}$ around the gear mesh component. No sidebands were observed at α_{C_1}, as it was expected from the analysis provided in chapter 2.3. One reason for this might be the suboptimal angular resampling procedure employed.

Interestingly, no components were observed at the gear mesh cyclic order of the second planetary stage, even though the measurement point was closer to this stage than to the first stage. The

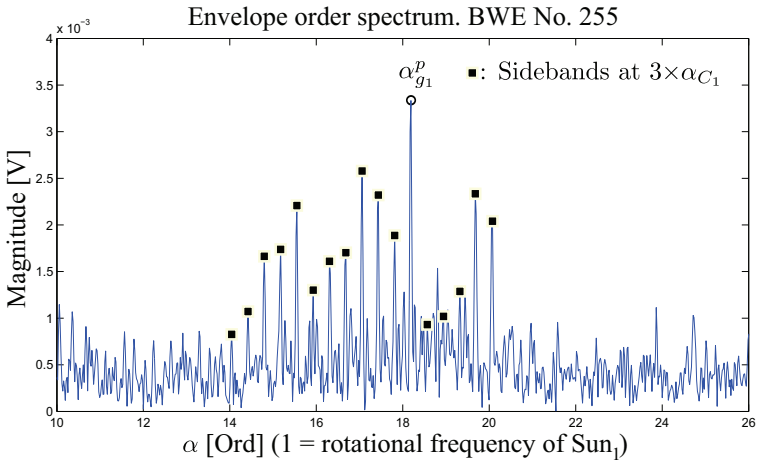

(a)

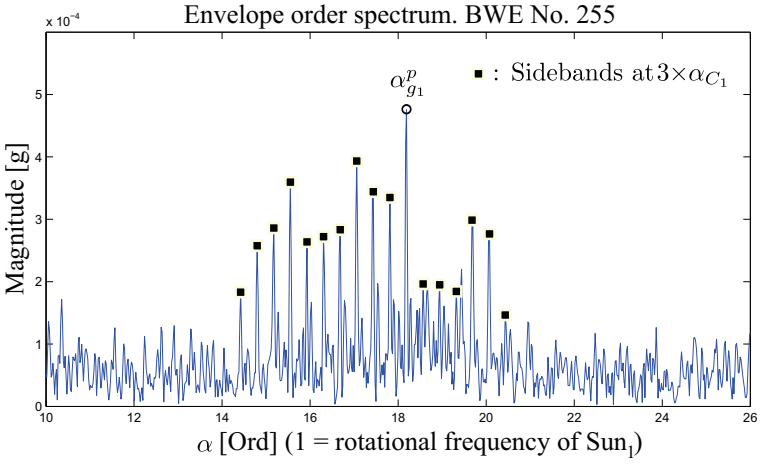

(b)

Figure 3.21: Portion of the envelope order spectrum (a) of the AE signal, and (b) of the acceleration signal.

author believes that in the second stage, due to the much lower rotational frequency of the gear wheels, the impacts produced due to asperity contact have less energy and therefore lower amplitude AE transients are generated, which are not detected by the sensor.

Fig. 3.20b shows a portion of the spectral coherence of the acceleration signal where some discrete components along the α-axis related with the meshing process of the first planetary stage are observed. Following, the envelope order spectrum of the acceleration signal was calculated by previously passing the signal through a high pass filter with cutoff frequency of 10.8 kHz. The envelope order spectrum, shown in fig. 3.21b, permits the clear identification of the gear mesh component with the sidebands spaced at α_{C_1}.

3.4.2. Measurements on the planetary gearbox of wind turbines

A long term measurement campaign was conducted on the planetary gearbox of three wind turbines Vestas V-47 in northern Germany. Each WT was equipped with the measurement system described in chapter 3.2. The system was installed on the nacelle of the WT (see fig. 3.22 and fig. 3.23a), and was configured to perform daily measurements of length 20 minutes. The sensors were installed on the top outer part of the ring gear, as illustrated in fig. 3.23b. The measured data was first locally stored in the hard drive of the measurement system. Afterwards, when the measurement system was idle, the data was transfered via fiberglass cable to an external hard drive connected to a computer installed in the tower base. Before the external hard drive was full of data, it was exchanged for another empty hard drive, and the hard drive with data was delivered to the University for analysis. The computer on the tower base also allowed the remote control of the measurement system on the nacelle. Fig. 3.22 illustrates the measurement scheme.

3.4.2.1. Description of the object under measurement

Each WT is equipped with two generators, one with 200 kW nominal power, and the other with a 660 kW nominal power. The use of one or the other generator depends on the wind conditions. When the 200 kW-generator is used, the rotor rotates with a nominal speed of 20 rpm; when the 660 kW generator is used, the nominal speed of the rotor is 26 rpm. When operating at the higher speed, the power is transmitted from the wind to the generator through

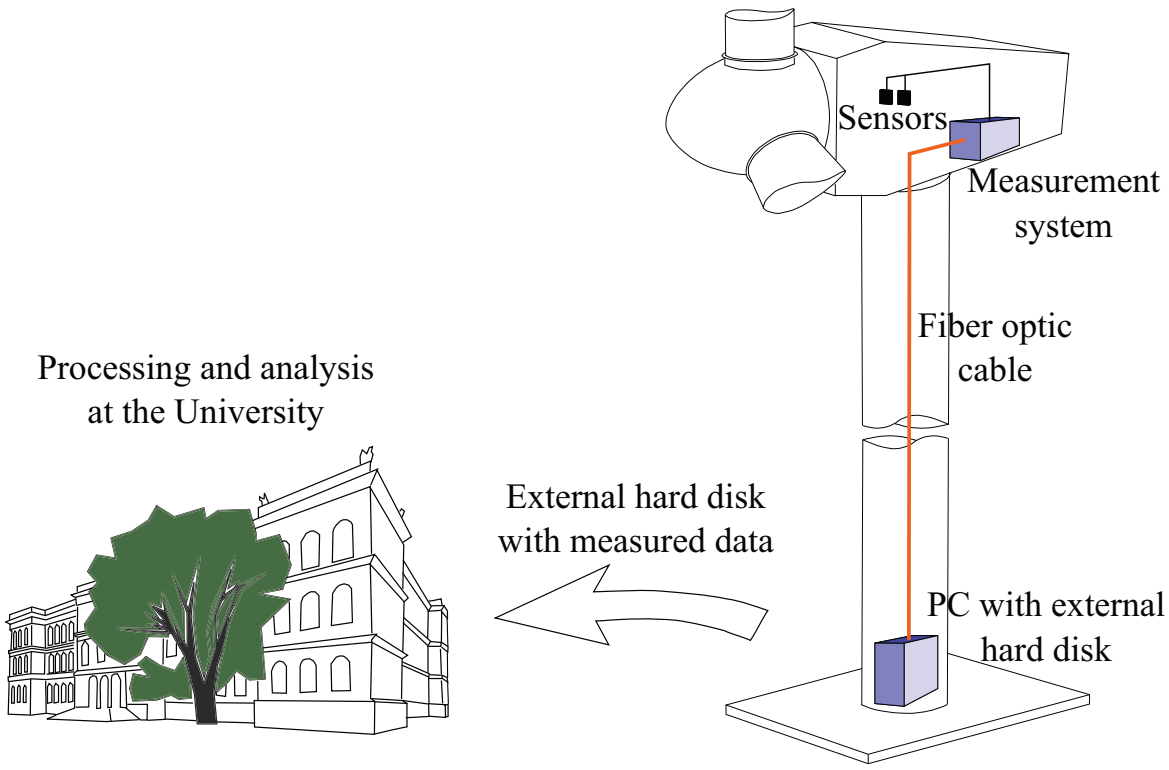

Figure 3.22: Scheme of the measurement solution implemented for the wind turbines.

the rotor, a single-stage planetary gearbox and a two-stage fixed-shaft helical gearbox. When operating at the lower speed, a third fixed-shaft helical stage is added. The rotor shaft is coupled to the carrier plate, thus constituting the input of the PG; the output being the sun shaft. The PG has three equally spaced planet gears. The number of teeth of the gear wheels are $Z_S = 18$, $Z_P = 34$ and $Z_R = 87$ (more information about the PG is given in appendix C). It can be shown that this PG pertains to the group (A), and that all meshing processes taking place have the same phase.

3.4.2.2. Operating conditions

The wind speed determines both, the load acting on the system and the rotational speed of the shafts. As previously explained, the control system of the WT allows only two possible constant rotational speeds for the rotor. Naturally, the load can be continuously variable. A change on the generator will cause a sudden change in the rotational speed, thus producing some transients, as shown in fig. 3.24. In this figure also some slight rotational speed variations during the operation with both generators are observed. It is well known that variations of

(a) (b)

Figure 3.23: (a) Measurement system and signal conditioning hardware installed on the nacelle of the WT. (b) AE and acceleration sensors mounted on the top outer part of the ring gear

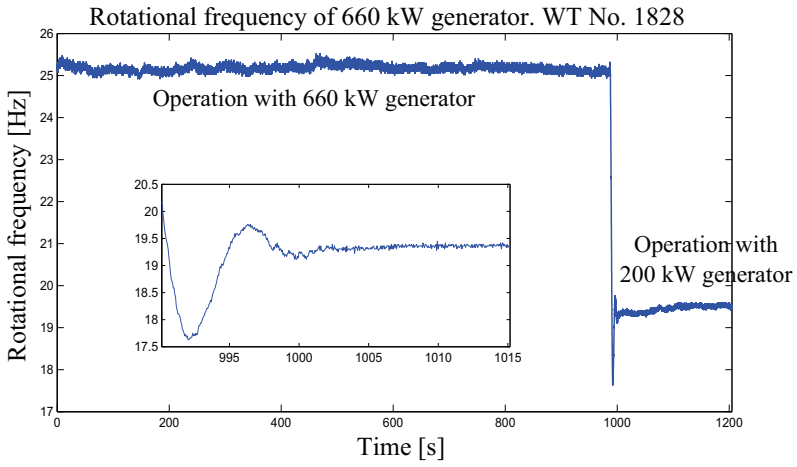

Figure 3.24: Example of rotational frequency of the 660 kW generator shaft during a measurement.

speed produce smearing of spectral component, thus hindering the analysis. To overcome this problem, angular resampling was introduced as the first stage of the sequence of signal processing tools used. A signal providing one pulse per revolution of the 660 kW generator shaft was used for this task.

3.4.2.3. Results

Some results of the measurements were already presented in the development of the AE model in chapter 2.3, to show that the AE signals measured in the PG are dominated by the stochastic

part –see figs. 2.17 and 2.18. For the same reason, there is no necessity to estimate and extract the deterministic (i.e. the fist-order cyclostationary) part to proceed with the second-order cyclostationary analysis.

As previously explained, the signals were first brought to the angular domain to avoid the inconviniences due to possible rotational speed variations during the measurements. Fig. 3.25a shows the portion of the spectral coherence around the gear mesh cyclic order, calculated from the AE signal. A discrete component along the α-axis is clearly recognized for the cyclic order correspondent to the gear mesh component α_g^p. Also sidebands at three times the carrier plate cyclic order ($3 \times \alpha_C$) are observed. Fig. 3.26 shows the envelope order spectrum of the AE signal. Due to its finer resolution, it is also possible to recognize sidebands at the carrier plate cyclic order α_C and, interestingly, at the cyclic order $\alpha_{P|_C}$, which corresponds to the relative rotational frequency of the planet gear wheels with respect to the carrier plate. Considering the analysis presented in section 3.3.2.3, this is an indicator of an event that occurs in the gearing process of one (or more) planet gear wheel(s) with the ring gear or sun gear, and that repeats once per revolution of the planet gear wheel with respect to the carrier plate. This event can be caused by a single flank tooth defect, as in the case of the test-bench measurements; however, it can also be due to the part of the transmission error of the planet gear wheel(s) that is caused by some degree of eccentricity, uneven tooth spacing, etc. (see fig. 1.8). Considering that the same behaviour was observed in the three WT, the author believes that in this case the latter cause is more probable than the former. That is, it is not considered a fault, but a characteristic of the operation of these particular type of planetary gearbox.

Similarly, fig. 3.25b shows the spectral coherence of the angular resampled acceleration signal. Here, the component at the gear mesh cyclic order is also observed. The presence of the sidebands, however, is not as clear as in the case of the AE. Finally, the order spectrum of the acceleration signal is presented in fig 3.27. As expected, sidebands at three times the cyclic order correspondent to the rotational frequency of the carrier plate ($3 \times \alpha_C$) are observed. No sidebands at $1 \times \alpha_C$ and at the cyclic order correspondent to the relative rotational frequency of the planet gear wheels with respect to the carrier plate $\alpha_{P|_C}$ are recognized.

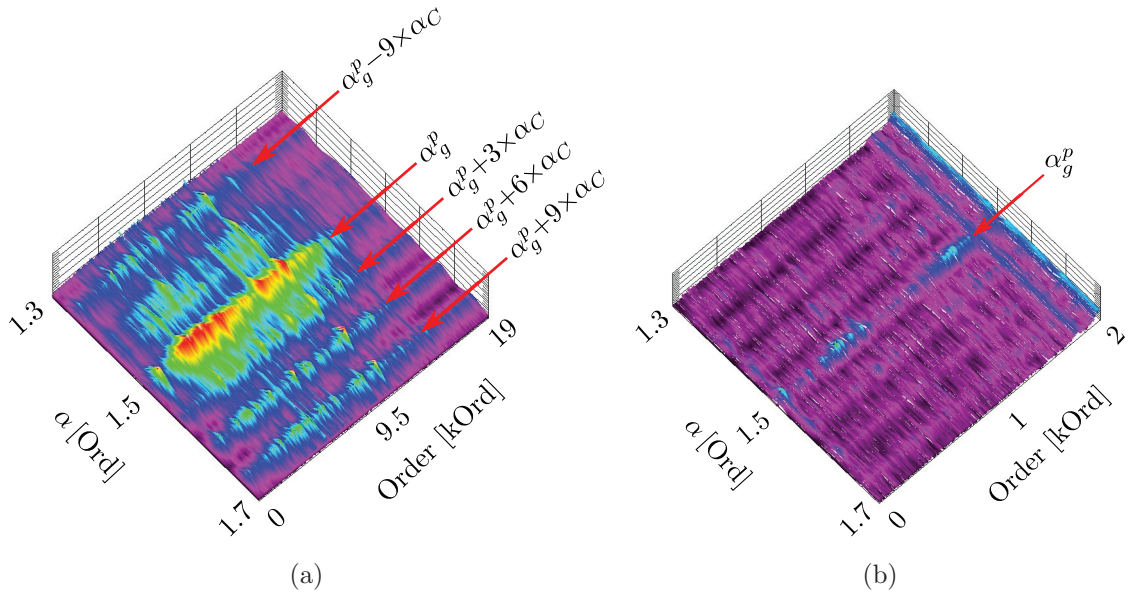

Figure 3.25: Spectral coherence of the signals after angular resampling. (a) Of the AE signal, and (b) of the acceleration signal.

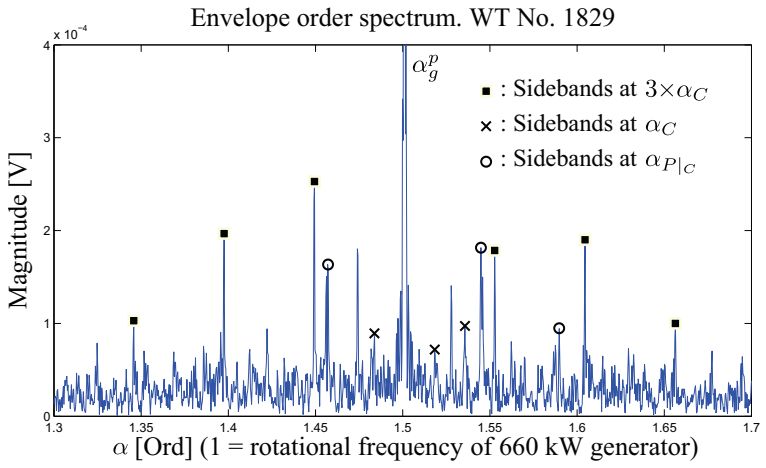

Figure 3.26: Portion of the envelope order spectrum of the AE signal around the gear mesh component.

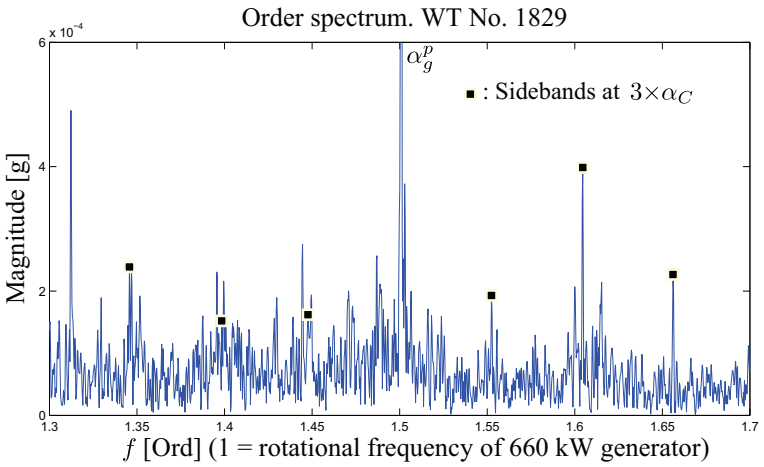

Figure 3.27: Portion of the order spectrum of the acceleration signal around the gear mesh component.

3.5. Summary and comments

Several issues had to be solved during the development of the measurement system. However, the final product proved to be reliable when responding to the different measurement requirements. Furthermore, care was taken to provide the measurement system with the capabilities of performing single-shot continuous and automated periodic measurements. Both capabilities encompass the majority of the situations found in research measurements. Hence, the developed system is a unit readily available for future requirements.

As presented in section 3.3, the results obtained from the AE signals were better than the results obtained from the acceleration signal, in the sense that the seeded defects were clearly identified only in the former. However, this was the case only when dealing with light failures. In measurements taken with heavier failures, the results from both signals similarly showed clear evidence of the faults.

During the test bench measurements, a close relation between the rotational speed of the motor and the amplitude of the AE coming from the gear meshing processes was observed: the higher the rotational speed, the higher the AE amplitudes and viceversa. This is illustrated in fig. 3.28. Here, the discrete components observed correspond to the gear mesh component and harmonics, each with its corresponding sidebands. It is observed that the magnitude of all components increased by a factor of ≈ 10 when changing the rotational speed from 1200 rpm to 1800 rpm. It is also observed that the magnitude of the components did not change significantly with the load variations. Similarly, a clear relation between the amplitudes of AE and the temperature of the lubricant was not observed. Differently, the AE signals measured on the bucket wheel excavators showed a high relation with the load (see fig. 3.19b).

The relation between rotational speed and the amplitudes of AE was also observed in the measurements on the wind turbines. This is illustrated in fig. 3.29. Fig. 3.29a shows a sample of the AE signal when the WT was operating with the 660 kW generator (higher rotational speed, see fig. 3.24); fig. 3.29b shows a sample of the AE signal when the WT was operating with the 200 kW generator (lower rotational speed). The magnitudes of the AE bursts are clearly higher in the former. A voltage signal proportional to the electrical power being generated was also measured. This signal provides a measure of the load acting on the system. Its value during the time portions illustrated in figures 3.29a and 3.29b, was of 3.5 Volt for both. The

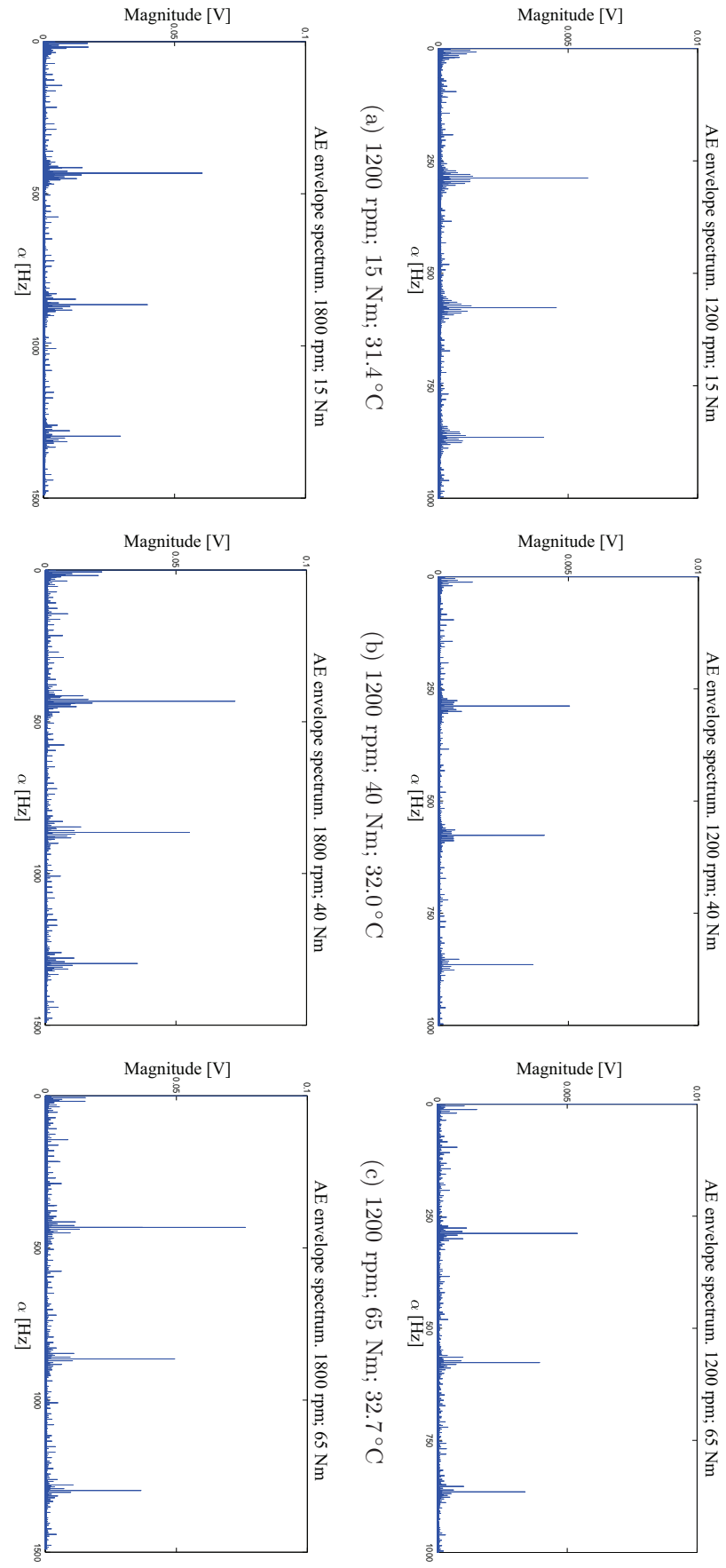

(a) 1200 rpm; 15 Nm; 31.4 °C

(b) 1200 rpm; 40 Nm; 32.0 °C

(c) 1200 rpm; 65 Nm; 32.7 °C

(d) 1800 rpm; 15 Nm; 33.9 °C

(e) 1800 rpm; 40 Nm; 35.1 °C

(f) 1800 rpm; 65 Nm; 35.6 °C

Figure 3.28: AE envelope spectra (AE band pass filtered between 50 kHz and 200 kHz)

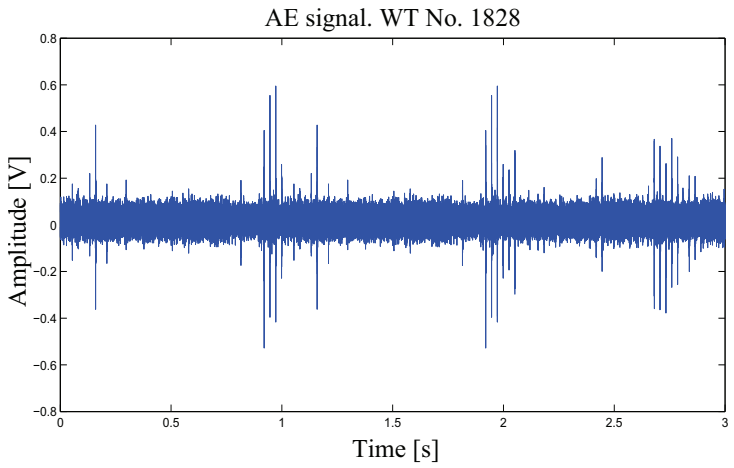

(a)

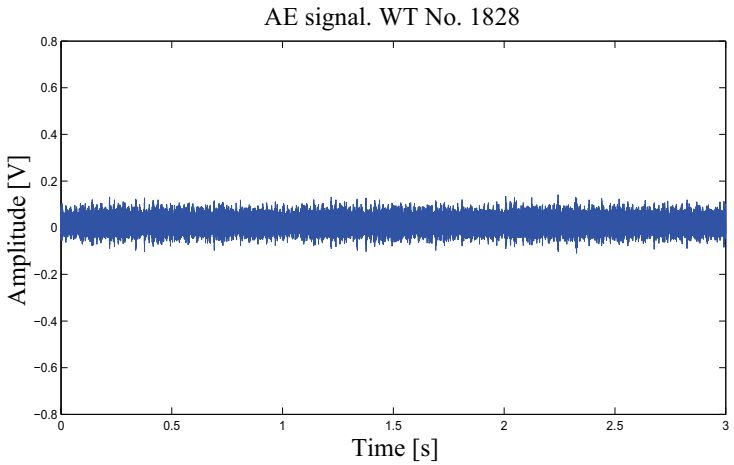

(b)

Figure 3.29: Portion of the AE signal during (a) higher rotational speed operation, and (b) lower rotational speed operation.

temperature measured on the output lubricant pipe of the planetary gearbox was of 51.0 °C for fig. 3.29a, and of 50.7 °C for fig. 3.29b. Being the load and temperature nearly the same for both measurements, the increase observed in the AE signal should be a result of the increase on the rotational speed of the gearbox.

4. General conclusion and outlook

4.1. General conclusion

In this research work, the problem of the vibration and the acoustic emissions (AE) analysis for the condition monitoring of epicyclic gearboxes has been addressed.

First, the kinematic analysis of a single-stage epicyclic gearbox has been performed and it was extended to multi-stage epicyclic gearbox. The mechanism of generation of vibrations and AE in epicyclic gearboxes were studied. Taking this into account, analytical models have been separately developed for the vibrations and acoustic emissions observed in a single-stage planetary gearbox, when measured with a sensor mounted on the outer part of the ring gear. Care was taken to develop and analyse the model in a step-by-step way, so that similar models can be developed for other configurations of epicyclic gearboxes and/or other sensor locations.

The proposed vibration model considered the vibrations as deterministic signals and included first the vibrations generated in the meshing between the planet gears and the ring gear and the transmission path of the vibrations to the sensor through the ring gear. The model was analysed in the frequency domain by using the stationary approach (the Fourier transform). It was shown that, depending on geometrical characteristics, the vibrations measured on different planetary gearboxes can have different spectral structures, all representing the normal, unfaulty case. However, it was presented that planetary gearboxes can be classified in four different groups, each showing specific features on the structure of the vibration spectrum. Each group was carefully studied and examples were used to aid the understanding. Afterwards, the influence on the spectrum of the vibrations generated in the meshing between the planet gears and the sun gear was investigated. The same was done for the transmission path of the vibrations to the sensor through the sun gear and carrier plate.

The proposed AE model considered the amplitude and time of arrival of the AE bursts as random processes. Accordingly, the analysis was performed separately for the deterministic and statochastic part. For the deterministic part, the stationary approach was used. It was shown that this part can only provide information about the signal on the low frequencies. Considering the high frequency nature of AE, the analysis of this part is not best suited for diagnosis purposes. Similarly, it was shown that the stationary approach applied for the analysis of the stochastic part results in a continuous spectrum, which is unable to provide any information about the signal. Differently, the cyclostationary approach was shown to be able to reveal the information, thus constituting a most valuable tool for the analysis of acoustic emissions in epicyclic gearbox.

For better comprehension purposes, the most important concepts, results and signal processing tools of the cyclostationary theory were presented and illustrated through an example.

Both proposed models should help the reader to understand the vibrations and AE generated in an epicyclic gearbox. It is emphasized, that the key point for this relies in the consideration of the time shift that can exist between the different gear meshing processes that simultaneously occur in the gearbox; and on the consideration of the transmission path of the vibrations and AE from their source to the sensor, which depends on the choice of the measurement point.

Measurements of vibrations and AE were carried out on the planetary gearbox of bucket wheel excavators and wind turbines. The signals were analysed by using the cyclostationary approach. Although no fault was observed, the measurements provided valuable information for the development of the AE model. In addition, a relation between the load and the amplitude of the AE generated in the gear meshing processes was observed in the AE signals from the bucket wheel excavators. In the case of the wind turbines, a relation between the rotational speed and the amplitude of the AE signals was observed.

Measurements of vibrations and AE were undertaken on a planetary gearbox test bench. Localized bearing and single-tooth flank defects with different levels of damage were seeded in one planet gear of the gearbox. The measurements were carried out under these two faulty conditions and under the non-faulty conditions for different combinations of rotational speed and load. The cyclostationary approach was used to process the AE and vibration signals. The results revealed that in the light level of damage, only the AE signals provided clear evidence of the faults. In other levels of damage, the results from both signals evidenced the fault.

The influence of the rotational speed, load and temperature of the lubricant on the amplitude of the AE generated in the gear meshing processes was investigated through measurements in the planetary gearbox test bench. The results suggested that the rotational speed is the most influential parameter; a higher rotational speed results in higher amplitudes of the AE and viceversa. A similar influence was observed for the load, but only at the lowest rotational speed measured (600 rpm); at higher rotational speeds, the load showed no evident influence in the amplitude of the measured AE. In the same manner, no clear relation between the temperature of the lubricant and the AE was found from the experiments carried out.

The main difference between the proposed models and the measured signals was the existence of sidebands around the gear mesh frequency spaced at the carrier rotational frequency only in the measured signals. An explanation for this could be the differences between the amplitude or shape of the vibrations and AE generated in each meshing process.

All industrial and test bench measurements were carried out with a system specially developed to fulfill the requirements of the measurement tasks. This system allows the acquisition of signals in two modes: single-shot continuous measurement and automated periodic measurements. Both represent the most typical requirements needed for measurements in research activities. Hence, the system permits the immediate use for future applications.

4.2. Outlook

Although the results obtained from the measurements with seeded defects were superior for the AE signals than for the vibration signals, the latter should not be left apart. It must be considered that the results presented in this thesis correspond to a particular case and, therefore, can not be expanded for the generality of situations. In the same line, the analysis measurements of vibrations and AE on a planetary gearbox with naturally developed failures would provide valuable information.

The fact that the use of AE provided auspicious results on detecting the seeded defects, makes it a good candidate for consideration in future condition monitoring systems for epicyclic gearboxes. Still, the results presented in this thesis should be considered only as one step forward in this direction. More research is needed to decipher the real behaviour of AE generated in epicyclic gearboxes under different conditions of load, rotational speed and temperature of the lubricant. The influence of these parameters on the diagnostic capabilities of the AE should be carefully studied. After this is done, the model of AE proposed in this thesis could be improved by including the influence of these parameters, thus leading to a more reliable model.

As presented in this thesis, the cyclostationary approach appears as a very powerful tool for the analysis of non-stationary signals. Its main drawback relies on the high computational requirements and the low processing speed of its signal processing tools. This is specially critical when dealing with high sampled signals such as AE signals. This restriction usually permits the cyclostationary analysis only on narrow cyclic frequency bands at a time, and with a non optimum cyclic frequency resolution. A solution for this could be the hardware implementation of the signal processing techniques using, for example, FPGA (field porgrammable gate array) based circuitry.

The AE data is bulky and, therefore, its handling and storage can become problematic. There is large room for the development of AE-based scalar and vectorial quantities which contain the most important diagnostic information in small amounts of data. The points mentioned in the two paragraphs above would help enormously in the development of this task.

A. Planetary gearbox of the test bench

Table A.1: General data.

Z_S	Z_P	Z_R	N	$\{\psi_i\}$	Ratio
18	26	72	3	$\left\{0; \frac{2\pi}{3}; \frac{4\pi}{3}\right\}$	1 : 5

Table A.2: Characteristic frequencies in Hz for different rotational speeds of the motor.

Motor rotational speed = 1200 rpm					
	1×	2×	3×	4×	5×
f_S	20	40	60	80	100
f_P	7.08	14.16	21.24	28.32	35.40
f_C	4	8	12	16	20
$f_{P\|C}$	11.08	22.16	33.24	44.32	55.40
f_g^p	288	576	864	1152	1440
f_{fault_b}	89.19	178.38	267.57	356.76	445.95
f_{fault_g}	11.08	22.16	33.24	44.32	55.40
Motor rotational speed = 1800 rpm					
	1×	2×	3×	4×	5×
f_S	30	60	90	120	150
f_P	10.62	21.24	31.86	42.48	53.10
f_C	6	12	18	24	30
$f_{P\|C}$	16.62	33.24	49.86	66.48	83.10
f_g^p	432	864	1296	1728	2160
f_{fault_b}	133.79	267.58	401.37	535.16	668.95
f_{fault_g}	16.62	33.24	49.86	66.48	83.10

Calculation of the BPFI factor for the planet bearing INA NK17/20

The BPFI factor is calculated by using the following formula [How94]:

$$\text{BPFI factor} = \frac{r\left(1 + \frac{d}{D}\cos\alpha\right)}{2} \tag{A.1}$$

where r is the number of rolling elements, d is the diameter of the rolling elements, $D = \frac{(D_i + D_o)}{2}$, D_i is the diameter of the contact circumference between the rolling elements and the inner race, D_o is the diameter of the contact circumference between the rolling elements and the outer race, and α is the contact angle. For the bearing used: $r = 14$; $d = 3$ mm; $D_i = 17$ mm; $D_o = 23$ mm and $\alpha = 0^*$. Substitution of these values into eq. A.1 gives BPFI factor = 8.05.

B. Planetary gearbox of the bucket wheel excavators

Table B.1: General data.

First planetary stage					
Z_{S_1}	Z_{P_1}	Z_{R_1}	N_1	$\{\psi_i\}_1$	Ratio
21	64	150	3	$\{0; \frac{2\pi}{3}; \frac{4\pi}{3}\}$	1 : 8.143
Second planetary stage					
Z_{S_2}	Z_{P_2}	Z_{R_2}	N_2	$\{\psi_i\}_2$	Ratio
27	31	90	3	$\{0; \frac{2\pi}{3}; \frac{4\pi}{3}\}$	1 : 4.333

Table B.2: Characteristic frequencies in Hz for the nominal motor rotational speed (990 rpm).

First planetary stage					
	1×	2×	3×	4×	5×
f_{S_1}	1.6649	3.3299	4.9948	6.6597	8.3247
f_{P_1}	0.2747	0.5495	0.8243	1.0990	1.3737
f_{C_1}	0.2045	0.4089	0.6134	0.8179	1.0223
$f_{P\|_{C_1}}$	0.4792	0.9584	1.4376	1.9169	2.3961
$f_{g_1}^p$	30.6697	61.3395	92.0092	122.6790	153.3487
Second planetary stage					
	1×	2×	3×	4×	5×
f_{S_2}	0.2045	0.4089	0.6134	0.8179	1.0223
f_{P_2}	0.0898	0.1796	0.2694	0.3592	0.4490
f_{C_2}	0.0472	0.0944	0.1415	0.1887	0.2359
$f_{P\|_{C_2}}$	0.1370	0.2740	0.4109	0.5479	0.6849
$f_{g_2}^p$	4.2466	8.4932	12.7397	16.9863	21.2329

Table B.3: Characteristic orders with respect to the rotational speed of the first planetary stage sun gear.

First planetary stage					
	1×	2×	3×	4×	5×
O_{S_1}	1	2	3	4	5
O_{P_1}	0.1650	0.3300	0.4951	0.6601	0.8251
O_{C_1}	0.1228	0.2456	0.3684	0.4912	0.6140
$O_{P\|_{C_1}}$	0.2878	0.5757	0.8635	1.1513	1.4391
$O_{g_1}^p$	18.4211	36.8421	55.2632	73.6842	92.1053
Second planetary stage					
	1×	2×	3×	4×	5×
O_{S_2}	0.1228	0.2456	0.3684	0.4912	0.6140
O_{P_2}	0.0539	0.1079	0.1618	0.2157	0.2697
O_{C_2}	0.0283	0.0567	0.0850	0.1134	0.1417
$O_{P\|_{C_2}}$	0.0823	0.1645	0.2468	0.3291	0.4114
$O_{g_2}^p$	2.5506	5.1012	7.6518	10.2024	12.7530

C. Planetary gearbox of the wind turbines

Table C.1: General data.

Z_S	Z_P	Z_R	N	$\{\psi_i\}$	Ratio
18	34	87	3	$\left\{0; \frac{2\pi}{3}; \frac{4\pi}{3}\right\}$	1: 5.833

Table C.2: Characteristic frequencies in Hz for operation with the two generators.

660 kW generator					
	1×	2×	3×	4×	5×
f_S	2.5278	5.0555	7.5833	10.1111	12.6389
f_P	0.6755	1.3510	2.0265	2.7020	3.3775
f_C	0.4333	0.8667	1.3	1.7333	2.1667
$f_{P\|_C}$	1.1088	2.2177	3.3265	4.4353	5.5441
f_g^p	37.7	75.4	113.1	150.8	188.5
200 kW generator					
	1×	2×	3×	4×	5×
f_S	1.9444	3.8889	5.8333	7.7778	9.7222
f_P	0.5196	1.0392	1.5588	2.0784	2.5980
f_C	0.3333	0.6667	1	1.3333	1.6667
$f_{P\|_C}$	0.8529	1.7059	2.5588	3.4118	4.2647
f_g^p	29	58	87	116	145

Table C.3: Characteristic orders with respect to the rotational speed of the 660 kW generator.

	1×	2×	3×	4×	5×
O_S	0.1006	0.2013	0.3019	0.4025	0.5032
O_P	0.0269	0.0538	0.0807	0.1076	0.1345
O_C	0.0172	0.0345	0.0518	0.0690	0.0863
$O_{P\|C}$	0.0441	0.0883	0.1324	0.1766	0.2207
O_g^p	1.5009	3.0019	4.5028	6.0037	7.5047

Bibliography

[ABREB04] J. Antoni, F. Bonnardot, A. Raad, and M. El Badaoui. Cyclostationary modelling of rotating machine vibration signals. *Mechanical Systems and Signal Processing*, 18(6):1285–1314, November 2004.

[Ant07] Jérôme Antoni. Cyclic spectral analysis in practice. *Mechanical Systems and Signal Processing*, 21(2):597–630, February 2007.

[Ant09] Jérôme Antoni. Cyclostationarity by examples. *Mechanical Systems and Signal Processing*, 23(4):987 – 1036, 2009.

[AR02] J. Antoni and R. B. Randall. Differential diagnosis of gear and bearing faults. *Journal Of Vibration And Acoustics-Transactions Of The Asme*, 124(2):165–171, April 2002.

[AR03] J. Antoni and R. B. Randall. A stochastic model for simulation and diagnostics of rolling element bearings with localized faults. *Transactions of the ASME*, 125:282–289, July 2003.

[AR06] Jérôme Antoni and R.B. Randall. The spectral kurtosis: application to the vibratory surveillance and diagnostics of rotating machines. *Mechanical Systems and Signal Processing*, 20(2):308–331, February 2006.

[BCR97] M.J. Brennan, M.H. Chen, and A.G. Reynolds. Use of vibration measurements to detect local tooth defects in gears. *Sound and Vibration*, 31(11):12–17, September 1997.

[BH87] Duane E. Bassett and Donald R. Houser. The design and analysis of single flank transmission error tester for loaded gears. Technical Report Technical Report 87-C-15, NASA, 1987.

[Blu05] David Mark Blunt. Synchronous averaging of epicyclic sun gear vibration. United States Patent No.: US 6,898,975 B2, May 31 2005.

[BR09] Tomasz Barszcz and Robert B. Randall. Application of spectral kurtosis for detection of a tooth crack in the planetary gear of a wind turbine. *Mechanical Systems and Signal Processing*, 23:1352–1365, 2009.

[BZ09] W. Bartelmus and R. Zimroz. Vibration condition monitoring of planetary gearbox under varying external load. *Mechanical Systems and Signal Processing*, 23:246–257, 2009.

[CSL00] C. CAPDESSUS, M. SIDAHMED, and J. L. LACOUME. Cyclostationary processes: Application in gear faults early diagnosis. *Mechanical Systems and Signal Processing*, 14(3):371–385, May 2000.

[DH77] D. Dowson and G.R. Higginson. *Elasto-Hydrodynamic lubrication*. Pergamon Press, 1977.

[Dou50] Walter F. Double. Double planetary drive axle. United States Patent No.: 2,529,330, November 1950.

[EM09] M. Elforjani and D. Mba. Natural mechanical degradation measurements in slow speed bearings. *Engineering Failure Analysis*, 16(1):521 – 532, 2009.

[For01] David Forrester. Method for the separation of epicyclic planet gear vibration signatures. United States Patent No.: US 6,298,725 B1, Oct. 9 2001.

[Ga94] William A. Gardner and et. al. *Cyclostationary in communications and signal processing*. IEEE Press, 1994.

[Gar87] William A. Gardner. *Statistical Spectral Analysis*. Prentice Hall, 1987.

[Gar91] William A. Gardner. Exploitation of spectral redundancy in cyclostationary signals. *IEEE SP Magazine*, pages 14–36, 1991.

[Gia99] G.B. Giannakis. *Digital Signal Processing Handbook*, chapter 17 - Cyclostationary Signal Analysis. 1999.

[GS94] W.A. Gardner and C.M. Spooner. The cumulant theory of cyclostationary time-series. i. foundation. *Signal Processing, IEEE Transactions on*, 42(12):3387–3408, Dec 1994.

[Har58] Stephen L. Harris. Dynamic loads on the teeth of spur gears. In *Proceedings of Institution of Mechanical Engeenering*, volume 172, pages 87–112, 1958.

[HM09] R.I. Raja Hamzah and D. Mba. The influence of operating condition on acoustic emission (ae) generation during meshing of helical and spur gear. *Tribology International*, 42(1):3 – 14, 2009.

[How94] I.M. Howard. A review of rolling element bearing vibration. Detection, diagnosis and prognosis. Technical Report DSTO-RR-0013, Defense Science and Technology Organisation (DSTO), 1994.

[HZ06] Robert F. Handschuh and James J. Zakrajsek. Current research activities in drive system technology in support of the nasa rotorcraft program. Technical Report TM214052, NASA, 2006.

[IK09] M. Inalpolat and A. Kahraman. A theoretical and experimental investigation of modulation sidebands of planetary gear sets. *Journal of Sound and Vibration*, 323(3-5):677 – 696, 2009.

[KG03] Jonathan A. Keller and Paul Grabill. Vibration monitoring of uh-60-a main transmission planetary carrier fault. In *American Helicopter Society 59th Annual Forum, Phoenix, Arizona, May 6th to 8th, 2003*, 2003.

[KLD07] A. Kahraman, J. Lim, and H. Ding. A dynamic model of a spur gear pair with friction. In *12th IFToMM World Congress, Besançon (France), June18-21, 2007*, 2007.

[LHLC87] Edward Hsiang-Hsi Lin, Huston, Ronald L., and John J. Coy. On dynamic loads in parallel shaft transmissions. 1: Modelling and analysis. Technical Report Technical memorandum 100180, NASA, 1987.

[Loo96] Johannes Looman. *Zahnradgetriebe. Grundlagen, Konstruktionen, Anwendungen in Fahrzeugen*. Springer, 1996.

[LP09] Gang Liu and Robert G. Parker. Impact of tooth friction and its bending effect on gear dynamics. *Journal of Sound and Vibration*, 320(4-5):1039 – 1063, 2009.

[LTO89] Hsiang Hsi Lin, Dennis P. Townsend, and Fred B. Oswald. Profile modification to minimize spur gear dynamic loading. Technical Report Technical Memorandum 89901, NASA, 1989.

[MC04] Scott L. Miller and Donald G. Childers. *Probability and random processes: with applications to signal processing and communications*. Elsevier Inc., 1st edition, 2004.

[McF91] P. D. McFadden. A technique for calculating the time domain averages of the vibration of the individual planet gears and the sun gear in an epicyclic gearbox. *Journal of Sound and Vibration*, 144(1):163–172, January 1991.

[McN02] James McNames. Fourier series analysis of epicyclic gearbox vibration. *Journal of Vibration and Acoustics*, 124:150–152, 2002.

[Mos05] Marianne Mosher. Results from a new separation algorithm for planetary gear system vibration measurements. In *Proceedings of IDETC/CIE 2005 ASME 2005 International Design Engineering Technical Conferences & Computers and Information in Engineering Conference September 24-28, 2005, Long Beach, California, USA*, 2005.

[MR06] D. Mba and Raj B.K.N. Rao. Development of acoustic emission technology for condition monitoring and diagnosis of rotating machines; bearings, pumps, gearboxes, engines and rotating structures. *The Shock and Vibration Digest*, 38(1), 2006.

[MS85] P.D. McFadden and J.D. Smith. An explanation for the asymmetry of the modulation sidebands about the tooth meshing frequency in epyciclic gear vibration. In *Proceedings of the Institution of Mechanical Engineers, 1985, 199(C1), 65-70*, volume 199(C1), pages 65–70, 1985.

[PA07] Romano Patrick-Aldaco. *A model based framework for fault diagnosis and prognosis of diynamical systems with an application to helicopter transmissions*. PhD thesis, Georgia Institut of Technology, August 2007.

[PKFA83] Adam Pintz, R. Kasuba, J.L. Frater, and R. August. Dynamic effect of internal spur gear drives. Technical Report Contractor report 3692, NASA, 1983.

[PL04] R. G. Parker and J. Lin. Mesh phasing relationships in planetary and epicyclic gears. *Journal of Mechanical Design*, 126(2):365–370, 2004.

[RAC00] R.B. Randall, J. Antoni, and S. Chobsaard. A comparison of cyclostationary and envelope analysis in the diagnostics of rolling element bearings. In *International Conference on Acoustics, Speech, and Signal Processing, 2000. (ICASSP '00)*, 2000.

[RAC01] R. B. Randall, j. Antoni, and S. Chobsaard. The relationship between spectral correlation and envelope analysis in the diagnostics of bearing faults and other cyclostationary machine signals. *Mechanical Systems and Signal Processing*, 15(5):945–962, September 2001.

[Ran04] R. B. Randall. Detection and diagnosis of incipient bearing failure in helicopter gearboxes. *Engineering Failure Analysis*, 11(2):177–190, April 2004.

[RAS08] Amani Raad, Jérôme Antoni, and Ménad Sidahmed. Indicators of cyclostationarity: Theory and application to gear fault monitoring. *Mechanical Systems and Signal Processing*, 22(3):574 – 587, 2008.

[Saw07] Nader Sawalhi. *Diagnostics, prognostics and fault simulation for rolling element bearings*. PhD thesis, The University of New South Wales, School of Mechanical and Manufacturing Engineering, 2007.

[SBS99] J. Shan, B. Bauer, and A. Seeliger. Schadensdiagnose von Planetengetrieben mit Hilfe der Schwingungsanalyse. Tagungsband VDI, Schwingungsüberwachung und -diagnose von Maschinen und Anlagen VDI-Berichte Nr. 1466, 27./28.5.99, S. 521-534. ISBN 3-18-091466-1, VDI, 1999.

[SCP04] Paul D. Samuel, Joseph K. Conroy, and Darryll J. Pines. Planetary transmission diagnostics. Technical Report NASA/CR 2004 213068, NASA, 2004.

[Sha01] Jianfeng Shan. *Zustandsdiagnose von Planetengetrieben bei stationärem und instationärem Betrieb mit Hilfe der Schwingungsanalyse*. PhD thesis, RWTH Aachen, 2001.

[SM87] A. Seeliger and B. Meiselbach. Planetengetriebe mit Überlastschutzeinrichtung für Hobelanlagen. *Glückauf*, 123(15):929–932, 1987.

[Smi03] J. D. Smith. *Gear Noise and Vibration*. Marcel Dekker, Inc., 2003.

[Smi04] Robert E. Smith. Single-flank testing of gears. *Gear Technology*, pages 18–21, May/June 2004.

[SMW85] A. Seeliger, B. Meiselbach, and W. Wenzel. Planetengetriebe für Hobelanlagen und Strebförderer. *Glückauf-Forschungshefte*, 46(6):286–290, 1985.

[SP03] Paul Samuel and Darryll Pines. Helicopter transmission diagnostics using constrained adaptive lifting. In *American Helicopter Society 59th Annual Forum, Phoenix, AZ, May 6-8, 2003*, 2003.

[SR06] N Sawalhi and R.B. Randall. Helicopter gearbox bearing fault identification unsing a range of analysis techniques. In *WCEAM 2006*, 2006.

[SW76] A. Seeliger and D. Wünsch. Schwingungsminderung in Maschinensystemen durch rechnergestützte Parameterdiskussion in der Konstruktionsphase. *Konstruktion*, 28(9):347–352, 1976.

[TM04] Chee Keong Tan and David Mba. The source of acoustic emission during meshing of spur gears. In *EWGAE 2004*, 2004.

[TM05] C. Tan and D. Mba. Correlation between acoustic emission activity and asperity contact during meshing of spur gears under partial elastohydrodynamic lubrication. *Tribology Letters*, 20(1):63–67, September 2005.

[VBVW09] C. Molina Vicuña, P. Burgwinkel, K. Vaehsen, and J. Wellhausen. Analysis of the acoustic emissions generated during the meshing process of planetary gearboxes.

In *The Sixth International Conference on Condition Monitoring and Machinery Failure Prevention Technologies*, pages 1252–1263, 2009.

[WSK+04] B. Wu, A. Saxena, T. S. Khawaja, R. Patrick, and P. Sparis G. Vachtsevanos. An approach to fault diagnosis of helicopter planetary gears. In *Proceedings of the IEEE Autotestcon 2004*, 2004.

[WSPV05] Biqing Wu, Abhinav Saxena, Romano Patrick, and George Vachtsevanos. Vibration monitoring for fault diagnosis of helicopter planetry gears. In *16th IFAC World Congress, July 3-8 2005, Prague*, 2005.

[ZLSV07] Erwin V. Zaretsky, David G. Lewicki, Michael Savage, and Brian L. Vlcek. Determination of turboprop reduction gearbox system fatigue life and reliability. Technical Report TM215019, NASA, 2007.

Curriculum Vitae

Personal data

Name:	Cristián Molina Vicuña
Date of birth:	07 January 1981
Place of birth:	Concepción, Chile
Citizenship:	Chilean

Internship and employment

2006 – 2009	Research assistant at the Institute of Mining and Metallurgical Machine Design (IBH), RWTH Aachen University, Germany
2005 – 2006	SPM Maintenance Engineering, Concepción Chile
2004	Internship at Huasco Mining Company, Vallenar, Chile

Studies

2006 – 2009	Ph.D. at the Institute of Mining and Metallurgical Machinery, IMR (former IBH), RWTH Aachen University
2003 – 2006	Magister on engineering sciences, University of Concepción
1999 – 2005	Civil mechanical engineering, University of Concepción

Education

1985 – 1998	Sacred Hearts School, Concepción

Schriftenreihe des Instituts für Bergwerks- und Hüttenmaschinenkunde

ABAR **A**achener **B**eiträge zur **A**ngewandten **R**echnertechnik

Band 1 Weidemann J. (1992).
Rechnerunterstützte Maschinenüberwachung als Instrument der vorausschauenden Instandhaltung in Walzwerken am Beispiel von Profilwalzgerüsten; ISBN 3-86073-051-7

Band 2 Cerv, H. (1992).
Softwarekonzept zur Analyse und echtzeitfähigen Simulation des dynamischen Verhaltens elektromechanisch gekoppelter Antriebe; ISBN 3-86073-058-4

Band 3 Ruhnau, S. (1992).
Automatisierung des Darstellungsprozesses bei der Variantenkonstruktion von Gewindebohrwerkzeugen unter Verwendung einer graphischen Programmiersprache am Beispiel eines mittelständischen Zulieferunternehmens der Montanindustrie; ISBN 3-86073-067-3

Band 4 Schniering, B. (1993).
Entwicklung und Umsetzung einer praxisorientierten CIM-Strategie als Informationssystem für kleine Unternehmen der Präzisionswerkzeugindustrie am Beispiel eines indirekten Zulieferunternehmens der Montanindustrie; ISBN 3-86073-153-X

Band 5 Streichfuss, M. (1993).
Maschinendiagnose an dieselgetriebenen Transportfahrzeugen im deutschen Steinkohlenbergbau; ISBN 3-86073-154-8

Band 6 Friedhelm, K. (1993).
Konzeption eines Informationssystems für bergmännische und markscheiderische Planung und Dokumentation; ISBN 3-86073-166-3

Band 7 Borstell, D. (1993).
Entwicklung eines Softwarekonzeptes für die rechnergestützte maschinentechnische Detailplanung im deutschen Steinkohlenbergbau; ISBN 3-86073-163-7

Band 8 Linnartz, A. (1993).
Integration von Zustandsdiagnose u. Instandhaltungsplanung, -steuerung und -analyse für dieselgetriebene Transportfahrzeuge im deutschen Steinkohlenbergbau;
ISBN 3-86073-290-0

Band 9 Müller, T. (1994).
Zustandsüberwachung und Verfügbarkeitsprognose in Großanlagen der Stahlindustrie;
ISBN 3-86073-291-9

Band 10 Kessler, H.-W. (1994).
Entwicklung und Untersuchung eines Diagnosesystems zur Wälzlagerüberwachung hydrodynamischer Getriebe; ISBN 3-86073-292-7

Band 11 Peschers, H. (1994).
Funktionalität und Aufbau eines Leitsystems zur Verbesserung der Materiallogistik von Steinkohlenbergwerken; ISBN 3-86073-293-5

Band 12 Dumoulin, L. (1995).
Die berührungslose, digitale Messung von Drehmoment und Drehzahl;
ISBN 3-86073-294-3

Band 13 Broderius, T. (1995).
Konzeption eines objektbasierten Programmsystems zur markscheiderischen Bearbeitung und Abbauplanung plattenförmiger Lagerstätten; ISBN 3-86073-295-1

Band 14 Geropp, B. (1995).
Schwingungsdiagnose an Wälzlagern mit Hilfe der Hüllkurvenanalyse;
ISBN 3-86073-296-X

Band 15 Plaster, A. (1996).
Weiterentwicklung des wettertechnischen CAE-Arbeitsplatzes für den deutschen Steinkohlenbergbau; ISBN 3-86073-297-8

Band 16 Ahrens, M. (1996).
Entwicklung eines Konzeptes zur Auslegung und zeitoptimalen Berechnung metallischer Zylinderkopfdichtungen mit Hilfe der Finiten Elemente Methode; ISBN 3-86073-298-6

Band 17 Zhang, M. (1996).
Messstellenreduktion an elektromechanischen Antriebssträngen mittels prozessgeführter digitaler Simulation - ein Beitrag zur Maschinenüberwachung und vorausschauenden Instandhaltung; ISBN 3-86073-299-4

Band 18 Mackel, J. (1996).
Die anwendungsorientierte Elastizitätsberechnung von Walzgerüsten unterschiedlicher Bauart; ISBN 3-86073-530-6

Band 19 Seeliger, A. (1996).
AKIDA - Aachener Kolloquium für Instandhaltung, Diagnose und Anlagenüberwachung - Tagungsband des Kolloquiums vom 30.-31. Mai 1996 in Aachen; ISBN 3-86073-531-4

Band 20 Staniullo, H.-J. (1996).
Ein Beitrag zur Entwicklung eines graphikorientierten Informationssystems für die maschinentechnische Betriebsmitteleinsatzplanung im deutschen Steinkohlenbergbau; ISBN 3-86073-532-2

Band 21 Tao, X. (1997).
Entwicklung eines Berechnungsmodells zur Ermittlung des Brennraumdruckverlaufs aus der Winkelgeschwindigkeit der Kurbelwelle; ISBN 3-86073-533-0

Band 22 Petit, E. (1997).
Entwicklung eines neuen Verfahrens zur Nassaufbereitung von Bauschutt;
ISBN 3-86073-534-9

Band 23 Levin, C. (1997).
Konzeption und Realisierung eines rechnergestützten Planungs- und Informationssystems für die Projektplanung im deutschen Steinkohlenbergbau; ISBN 3-86073-535-7

Band 24 Kaub, R. (1997).
Konzeption und Realisierung eines Informationssystems zur Dokumentation und Vorhersage der Ausgasung im deutschen Steinkohlenbergbau; ISBN 3-86073-536-5

Band 25 Schumacher, T. (1998).
Konzeption und Entwicklung eines integrierten maschinentechnischen Planungs- und Informationssystems für Rohstoffgewinnungsbetriebe; ISBN 3-86073-537-3

Band 26 Rensmann, F. (1998).
Entwicklung einer kleinbauenden Gruben-Diesellokomotive mit optimiertem hydraulischen Antriebssystem unter Berücksichtigung der wirtschaftlichen Rahmenbedingungen im deutschen Steinkohlenbergbau; ISBN 3-86073-538-1

Band 27 Asch, A. (1998).
Technische Diagnose am stoßaufgeladenen Dieselmotor mit Hilfe leistungskorrelierter Meßgrößen; ISBN 3-86073-539-X

Band 28 Koch, S. (1998).
Schwingungssimulation industrieller Antriebe mit Drehfeldmaschinen großer Leistung; ISBN 3-86073-700-7

Band 29 Wischnewski, R. (1998).
Entwicklung eines modularen, wissensbasierten Systems zur Diagnose von dieselgetriebenen Transportfahrzeugen im Deutschen Steinkohlenbergbau; ISBN 3-86073-701-5

Band 30 Seeliger, A. (1998).
AKIDA - 2. Aachener Kolloquium für Instandhaltung, Diagnose und Anlagenüberwachung - Tagungsband des Kolloquiums vom 3.-4. Juni 1998 in Aachen;
ISBN 3-86073-531-4

Band 31 Burgwinkel, P. (1998).
Das Transportleitsystem TLS - ein zentrales Planungs-, Steuerungs- und Überwachungssystem zur Verbesserung der Materiallogistik von Steinkohlenbergwerken;
ISBN 3-86073-703-1

Band 32 Lange, C. (1998).
Die Entwicklung eines Planungs- und Informationssystems für die bergmännische Planung im deutschen Steinkohlenbergbau; ISBN 3-86073-704-X

Band 33 Tao, X. (1997).
Konzeption einer Regelung zur automatischen Kohleninjektion in Drehstromlichtbogenöfen; ISBN 3-86073-705-8

Band 34 Georges, D. (1999).
Konzeption, Entwicklung und Einsatz eines Überwachungssystems zur Erkennung und Vermeidung von qualitätsmindernden Störschwingungen an Kaltwalzgerüsten;
ISBN 3-86073-706-6

Band 35 Lorbach, J. (1999).
Konzeption und Implementierung eines objekt-orientierten Datenmodells zur integrierten Nutzung von Prozessdaten für den Bereich Wettertechnik; ISBN 3-86073-707-4

Band 36 Reimers, J. (1999).
Konzeption eines Rohrleitungsplanungssystems für den deutschen Steinkohlenbergbau; ISBN 3-86073-708-2

Band 37 Arefzadeh, S. (1999).
Klassifizierung der Belastung von Walzanlagen mittels Softcomputing-Methoden als Grundlage zur Stichplan- und Restlebensdaueroptimierung; ISBN 3-86073-709-0

Band 38 Bauer, B. (2000).
Körperschallanalyse von Verzahnungen im Rahmen der zustandsorientierten Instandhaltung; ISBN 3-86073-670-1

Band 39 Baumann, S. (2000).
Entwicklung eines Diagnosesystems für hydrostatische Antriebe von dieselgetriebenen Transportfahrzeugen im deutschen Steinkohlenbergbau; ISBN 3-86073-671-X

Band 40 Mandelartz, J. (2000).
Der Sekundäraluminium-Stoffstrom in Deutschland unter transporttechnischen und logistischen Gesichtspunkten; ISBN 3-86073-672-8

Band 41 Schneider, S. (2000).
Methode zur Zustandsüberwachung von Kreuzgelenkwellen in den Hauptantrieben von Walzgerüsten; ISBN 3-86073-673-6

Band 42 Quacken, G. (2000).
Bestimmung von produktspezifischen, störungsbedingten Qualitätskosten bei der Maschinendiagnose; ISBN 3-86073-674-4

Band 43 Türk, M. (2001).
Optimierung des Walzprozesses und der Anlagenauslastung durch moderne Diagnoseverfahren und vernetzte Überwachungssysteme; ISBN 3-86073-675-2

Band 44 Teschers, R. (2001).
Konzeption und Entwicklung eines Gesamtinformationssystems in einem interdisziplinären Forschungsprogramm am Beispiel eines Arbeitsbereichs; ISBN 3-86073-676-0

Band 45 Shan, J. (2001).
Zustandsdiagnose von Planetengetrieben bei stationärem und instationärem Betrieb mit Hilfe der Schwingungsanalyse; ISBN 3-86073-677-9

Band 46 Seeliger, A., Burgwinkel, P. (2002).
AKIDA - 4. Aachener Kolloquium für Instandhaltung, Diagnose und Anlagenüberwachung - Tagungsband des Kolloquiums vom 6.-7. November 2002 in Aachen; ISBN 3-86073-677-9

Band 47 Lorbach, J. (1999).
Entwicklung und Erprobung eines neuartigen integrierten Informations-, Kommunikations- und Automatisierungssystems für den Untertagebau;
ISBN 3-86073-679-5

Band 48 Nahrath, T. (2003).
Untersuchung zur Erfassung des Säulendurchmessers bei der Düsenstrahlinjektion zur Baugrundfestigung; ISBN 3-89653-981-7

Band 49 Heim, G. K. (2003).
Grenzen und Möglichkeiten einer EDV-Unterstützung gruppenbezogener Planungsarbeit am Beispiel bergbaulicher Produktionsbetriebe; ISBN 3-86130-210-1

Band 50 Vollmer, A. (2003).
Technische und organisatorische Lösungen zur Einführung von Instandhaltungsplanungs- und -steuerungssystemen; ISBN 3-86130-192-X

Band 51 Markhöfer, J. (2003).
Konzeption und Realisierung eines modellgestützten Instrumentariums zur Optimierung der Transportlogistik für den primären und sekundären Kupferstoffstrom;
ISBN 3-86130-196-2

Band 52 Hoppe, H. (2003).
Konzeption und Entwicklung eines technischen Berichtsystems zur weltweiten Anlagenüberwachung am Beispiel von Gutbett-Walzenmühlen; ISBN 3-86130-211-X

Band 53 Weyres, S. (2003).
Mobile Computing in der Instandhaltung ? Realisierung medienbruchfreier Arbeitsabläufe; ISBN 3-86130-212-8

Band 54 Schaaf, C. (2003).
Entwicklung eines Reportgenerators zur prozessoptimierten Messsignalauswertung an Walzanlagen; ISBN3-86130-213-6

Band 55 Reitz, K. (2004).
Betrachtung der Körperschallemission von Wälzlagern zur Verfeinerung der Zustandsdiagnose; ISBN 3-86130-214-4

Band 56 Gantevoort, T. (2004).
Integration der Körperschalldiagnose in das kommunikations- und informationstechnische System des deutschen Untertagebergbaus; ISBN 3-86130-215-2

Band 57 Janser, S. (2004).
Modellierung einer Redistributionslogistik metallhaltiger Gebrauchsgüter am Beispiel von Elektronikaltgeräten; ISBN 3-86130-216-0

Band 58 Seeliger, A., Burgwinkel, P. (2004).
AKIDA - 5. Aachener Kolloquium für Instandhaltung, Diagnose und Anlagenüberwachung - Tagungsband des Kolloquiums vom 9.-10. November 2004; ISBN 3-86130-217-9

Band 59 Schumacher, G. (2004).
Entwicklung und Erprobung eines nassmechanischen Bauschuttsortierers;
ISBN3-86130-218-7

Band 60 Küpper, T. M. E. (2005).
Konzeption und Entwicklung eines intranetbasierten Informationssystems für den deutschen Steinkohlenbergbau; ISBN 3-86130-219-5

Band 61 Aguilar, C. A. (2005).
Konzeption und Implementierung einer komponentenbasierten Softwareentwicklungsplattform für raumbezogene internetfähige Informationssysteme; ISBN 3-86130-220-9

ASRE Aachener Schriften zur Rohstoff- und Entsorgungstechnik

Band 62 Balke, A. (2006).
Lebenszyklusrechnung von IPS-Systemen in der Auswahl-, Einführungs- und Betriebsphase; ISBN-10: 3-9810344-2-2; ISBN-13: 978-3-9810344-2-4

Band 63 Seeliger, A., Burgwinkel, P. (2006).
AKIDA - 6. Aachener Kolloquium für Instandhaltung, Diagnose und Anlagenüberwachung - Tagungsband des Kolloquiums vom 14.-15. November 2006 in Aachen; ISBN-10: 3-9810344-3-0; ISBN-13: 978-3-9810344-3-1

Band 64 Charlier, F. (2006).
Neuentwicklung eines schlagwettergeschützten Dieselmotors der Leistungsklasse bis $100kW$ mit Abgasturbolader; ISBN-10: 3-9810344-4-9; ISBN-13: 978-3-9810344-4-8

Band 65 Bencze, A. (2007).
Entwicklung eines miniaturisierten Drehmomentmesssystems - μ-ETC;
ISBN: 978-3-9810344-5-5

Band 66 Brümmer, G. (2008).
Konzeption, Entwicklung und Einführung eines grafikbasierten Qualitätssicherungs-Systems für den mobilen Einsatz; ISBN: 978-3-9810344-7-9

Band 67 Steinhusen, C. (2008)
Konzept zur Überwachung elektronischer Komponenten in Windenergieanlagen mit Hilfe konditionierter Simulation und begleitender Messung; ISBN: 978-3-9810344-9-3

Band 68 Meßner, A. (2008)
Verfahren zur Schadensdetektion bei langsam oszillierenden Kreuzgelenkwellenlagerungen in Walzwerksantrieben; ISBN: 978-3-941277-00-7

Band 69 Lachmann, J. M. (2008)
Entwicklung eines simulationsgestützten Condition-Monitoring-Systems zur Onlineüberwachung des mechanischen Antriebsstranges von Multimegawattwindenergieanlagen; ISBN: 978-3-941277-01-4

Band 70 Seeliger, A., Burgwinkel, P. (2008).
AKIDA - 7. Aachener Kolloquium für Instandhaltung, Diagnose und Anlagenüberwachung - Tagungsband des Kolloquiums vom 18.-19. November 2008 in Aachen; ISBN-13: 978-3-941277-02-1

Band 71 Buttgereit D. A. (2009).
Konzeption und Entwicklung eines WLAN-basierten Kommunikations- und Informationssystems für den deutschen Steinkohlenbergbau;
ISBN-13: 978-3-941277-04-5